UNIVERSITY OF CALIFORNIA, SAN DIEGO

Novel Photonic Bandgap Based Architectures for Quantum Computers and Networks

A dissertation submitted in partial satisfaction of the
requirements for the degree Doctor of Philosophy
in
Electrical Engineering (Applied Physics)

by

Durdu Güney

Committee in charge:

Professor David A. Meyer, Chair
Professor Sadik C. Esener
Professor Yu-Hwa Lo
Professor George Papen
Professor Jeffrey Rabin

2007

The dissertation of Durdu Güney is approved, and it is acceptable in quality and form for publication on microfilm:

Chair

University of California, San Diego

2007

To my family.

TABLE OF CONTENTS

LIST OF FIGURES

ACKNOWLEDGMENTS

I very much would like to thank my advisor Prof. David Meyer for his patience and excellent guidance. Much of this dissertation would not be completed without his continual encouragement and support. His deep knowledge of quantum information processing in along with his kind and intelligent personality led me achieve this work.

I am also very grateful to my co-advisor Prof. Sadik Esener for his sincere help and excellent guidance toward my PhD degree at UCSD. I can never forget his continual encouragement and support since the beginning.

I am thankful to my other committee members Profs. Yu-Hwa Lo, George Papen, and Jeffrey Rabin for their time, classes, and valuable comments.

I am indebted to Prof. Lu Sham for his classes which have been a foundation for my research.

I would like to thank Prof. Jelena Vuckovic from Stanford University and Prof. Ekmel Özbay from Bilkent University (Turkey) for their helpful discussions on the theory of photonic crystal cavity QED and three-dimensional photonic crystals, which are essential ingredients for Chapter IV. I am thankful to Prof. Shi-Biao Zheng from Fouzhou University (China), whose discussions on atomic state detection were very useful for Chapter V. I also thank Profs. David R. Smith and Sheldon Schultz of the Physics Department at UCSD. Chapter VI was partially motivated by interactions with them.

I am grateful to my family for their love and continual encouragement about my career.

Funding for this work was provided in part by the National Security Agency (NSA) and Advanced Research and Development Activity (ARDA) under Army Research Office (ARO) grant, by the DARPA QuIST program, and by the National Science Foundation (NSF).

Portions of Chapter IV were presented in the paper: D. Ö. Güney and D.

A. Meyer, "*Creation of entanglement and implementation of quantum logic gate operations using a three-dimensional photonic crystal single-mode cavity*", J. Opt. Soc. Am. B **24**, 283 (2007). Portions of Chapter V were presented in the paper: D. Ö. Güney and D. A. Meyer, "*Integrated conditional teleportation and readout circuit based on a photonic crystal single chip*", J. Opt. Soc. Am. B **24**, 391 (2007). A portion of Chapter VI was presented in a conference paper: D. Ö. Güney and D. A. Meyer, "*Optoelectronic simulation of the Klein paradox using left-handed materials*", 2004 MRS Spring Meeting, 12-16 Apr. 2004, San Fransisco, CA, USA. The dissertation author is the primary author in these papers.

VITA

October 5, 1978	Born, Ordu, Turkey
2000	B.S., Physics, Boğaziçi University, İstanbul
2000–2002	Teaching/Research Assistant, Faculty of Engineering and Natural Sciences Sabancı University, İstanbul
2002	M.S., Electronics Engineering and Computer Science, Sabancı University, İstanbul
2002–2007	Research Assistant, University of California, San Diego
2007	Ph.D., Electrical Engineering (Applied Physics) University of California, San Diego

PUBLICATIONS

[1] D. Ö. Güney and D. A. Meyer, "*Creation of entanglement and implementation of quantum logic gate operations using a three-dimensional photonic crystal single-mode cavity*", J. Opt. Soc. Am. B **24**, 283 (2007).

[2] D. Ö. Güney and D. A. Meyer, "*Integrated conditional teleportation and readout circuit based on a photonic crystal single chip*", J. Opt. Soc. Am. B **24**, 391 (2007).

[3] D. Ö. Güney, T. Demirci, S. Isci, Y. Gurbuz, and M. N. Inci, "*Design and Simulation of Photonic Crystals for Temperature Reading of Ultra-small Structures*", 2001 IEEE/LEOS Annual Meeting Conference Proceedings, 11-15 Nov. 2001, San Diego, CA, USA.

[4] D. Ö. Güney, S. Isci, Y. Gurbuz, and M. N. Inci, "*Photonic Crystals for Temperature Mapping of Micron-sized Objects*", MRS Fall 2001 Meeting, Microphotonics: Materials, Physics, and Applications, 26-30 Nov. 2001, Boston, Massachusetts, USA.

[5] D. Ö. Güney, Y. Gurbuz, M. N. Inci, "*A Two-dimensional Photonic Crystal for Surface Temperature Reading of Miniature Systems*", SPIE Photonics West 2002, Optoelectronics 2002: Integrated Optoelectronic Devices, 20-25 Jan. 2002, San Jose, CA, USA.

[6] T. Demirci, D. Ö. Güney, A. Bozkurt, and Y. Gurbuz, "*Electro-thermal simulations and modelling of micromachined gas sensors*", MEMS Conference 2001, 24-26 Aug. 2001, Berkeley, CA, USA.

[7] D. Ö. Güney and D. A. Meyer, "*Optoelectronic simulation of the Klein paradox using left-handed materials*", 2004 MRS Spring Meeting, 12-16 Apr. 2004, San Fransisco, CA, USA.

[8] D. Ö. Güney and M. N. Inci, "*Two-dimensional photonic crystal slab for remote temperature mapping*" (in preparation for journal).

[9] D. Ö. Güney and D. A. Meyer, "*Wave propagation analogy between the Klein paradox for the spin-zero particles and negative index medium*" (in preparation for journal, Nature Physics).

[10] D. Ö. Güney and D. A. Meyer, "*How to simulate the Klein paradox for the spin-zero particles using left-handed materials*" (in preparation for journal).

[11] D. Ö. Güney, *"Security analysis of the ... cryptosystem using graph theory*" (classified).

ABSTRACT OF THE DISSERTATION

Novel Photonic Bandgap Based Architectures for
Quantum Computers and Networks

by

Durdu Güney
Doctor of Philosophy in Electrical Engineering (Applied Physics)
University of California, San Diego, 2007
Professor David A. Meyer, Chair

All of the approaches for quantum information processing have their own advantages, but unfortunately also their own drawbacks. Ideally, one would merge the most attractive features of those different approaches in a single technology. We envision that large-scale photonic crystal (PC) integrated circuits and fibers could be the basis for robust and compact quantum circuits and processors of the next generation quantum computers and networking devices. Cavity QED, solid-state, and (non)linear optical models for computing, and optical fiber approach for communications are the most promising candidates to be improved through this novel technology. In our work, we consider both digital and analog quantum computing.

In the digital domain, we first perform gate-level analysis. To achieve this task, we solve the Jaynes-Cummings Hamiltonian with time-dependent coupling parameters under the dipole and rotating-wave approximations for a 3D PC single-mode cavity with a sufficiently high Q-factor. We then exploit the results to show how to create a maximally entangled state of two atoms and how to implement several quantum logic gates: a dual-rail Hadamard gate, a dual-rail NOT gate, and a SWAP gate. In all of these operations, we synchronize atoms, as opposed

to previous studies with PCs. The method has the potential for extension to N-atom entanglement, universal quantum logic operations, and the implementation of other useful, cavity QED-based quantum information processing tasks.

In the next part of the digital domain, we study circuit-level implementations. We design and simulate an integrated teleportation and readout circuit on a single PC chip. The readout part of our device can not only be used on its own but can also be integrated with other compatible optical circuits to achieve atomic state detection. Further improvement of the device in terms of compactness and robustness is possible by integrating with sources and detectors in the optical regime.

In the analog domain, we consider a quantum simulation problem. We show that the Klein paradox for the Klein-Gordon equation of a spin-zero particle manifests exactly the same kind of wave propagation and negative refraction phenomenon as the scattering of a transverse-electric-polarized electromagnetic wave incident on a negative index medium. Using this peculiar feature of negative index materials, we show that real time control and processing of some quantum experiments related with Klein paradox can be achieved by an optoelectronic simulator designed according to certain transformations and approximations.

Chapter I

Introduction

Most of the material in §I.A (quantum state evolution) and §I.B (quantum measurement) is studied in more depth in Ref. [1]. Quantum process tomography that we review in §I.C is based on Nielsen and Chuang's introductory book on quantum computation and quantum information [2]. Information that we present in §I.D (atomic interferometers) is mostly taken from Steven Chu's course on 'atomic interferometers' [3]. For more details and references please consult these valuable resources. In §I.D.1 (Ramsey interferometer) we review the interaction of atomic beams with two separated oscillatory fields based on Ref. [4], which describes the process in an excellent and intuitive fashion with many references. Ref. [5] provides an excellent review of "decoherence" phenomenon in quantum mechanics and explains how the transition from quantum in the microscale to classical in our macroscale world occurs. In §I.E (decoherence) we briefly summarize this concept critical to quantum information processing.

I.A Quantum State Evolution

Controlled time evolution of quantum states of a physical system forms the basis of quantum logic operations. In quantum mechanics time is not an observable (i.e., not an operator) in the sense that it is only a parameter.

Dynamics of a quantum state $|\Psi(t_0)\rangle$ under time displacement $t_0 \to t$ can be described by the time evolution operator $U(t, t_0)$, in such a way that

$$|\Psi(t)\rangle = U(t, t_0)|\Psi(t_0)\rangle \tag{I.1}$$

Note that if we can engineer the time evolution operator on demand we could build many useful operations relevant to quantum computation such as quantum gates and creation of entanglement. The nature of $U(t, t_0)$ is determined by the underlying Hamiltonian operator H that describes the physical system. The relation between $U(t, t_0)$ and H is given by the Schrodinger equation,

$$i\hbar \frac{\partial}{\partial t} U(t, t_0) = HU(t, t_0). \tag{I.2}$$

Formal solutions to this equation can be investigated in three cases depending on how the Hamiltonian operator H evolves in time. Once we find the solution for $U(t, t_0)$ in Eqn. (I.1), we can determine how the state $|\Psi\rangle$ evolves in time using Eqn. (I.2) and whether or not we manage to build useful quantum operations for our purpose under given physical system design parameters.

If the Hamiltonian operator H is independent of time then the solution to Eqn. (I.2) can be written as

$$U(t, t_0) = e^{-\frac{i}{\hbar} H(t - t_0)}. \tag{I.3}$$

In the case that H is time-dependent but the H's at different times commute then the formal solution to the Schrodinger equation (I.2) is

$$U(t, t_0) = e^{-(\frac{i}{\hbar}) \int_{t_0}^{t} dt' H(t')} \tag{I.4}$$

For convenience we can expand the exponential as follows:

$$e^{-(\frac{i}{\hbar}) \int_{t_0}^{t} dt' H(t')} = 1 - \frac{i}{\hbar} \int_{t_0}^{t} dt' H(t') + [\frac{(-i)^2}{2}][\frac{\int_{t_0}^{t} dt' H(t')}{\hbar}]^2 + ... \tag{I.5}$$

The Hamiltonian operator that describes the atom-microcavity interaction in Chapters IV and V for the creation of atom-atom and atom-cavity entanglements and the implementation of several quantum logic operations falls into this category.

The third case is that the H's at different times do not commute. This type of Hamiltonian operator is not convenient from the computational perspective, although it might be the case that it presents richer possibilities. The formal solution to Eqn. (I.2) in such a situation is given by

$$U(t,t_0) = 1 + \sum_{n=1}^{\infty} (\frac{-i}{\hbar})^n \int_{t_0}^{t} dt_1 \int_{t_0}^{t_1} dt_2 ... \int_{t_0}^{t_{n-1}} dt_n H(t_1)H(t_2)...H(t_n), \qquad \text{(I.6)}$$

which is sometimes known as the Dyson series.

I.B Quantum Measurement

Quantum measurement is an essential part of quantum computing models such as circuit and cluster state quantum computing. Dirac says, "A measurement always causes the system to jump into an eigenstate of the dynamical variable that is being measured." Before the measurement the quantum state $|\Psi\rangle$ can be assumed to be in a linear superposition of eigenstates of the observable being measured. In mathematical terms this can be expressed as

$$|\Psi\rangle = \sum_{a'} c_{a'} |a'\rangle, \qquad \text{(I.7)}$$

where $c_{a'}$ is the complex probability amplitude for the corresponding eigenstate $|a'\rangle$. Therefore, the measurement collapses $|\Psi\rangle$ into $|a'\rangle$ with a probability $|c_{a'}|^2$. This is one of the fundamental postulates of quantum mechanics. More precisely quantum measurements are described by a set $\{M_m\}$ of projection operators, which satisfies the completeness equation

$$\sum_m M_m^\dagger M_m = I. \tag{I.8}$$

The probability that the result m occurs is given by

$$p(m) = \langle\Psi|M_m^\dagger M_m|\Psi\rangle \tag{I.9}$$

and the state of the system after the measurement is thrown into

$$\frac{M_m|\Psi\rangle}{\sqrt{p(m)}} \tag{I.10}$$

For example, a two-level atom can be prepared in an arbitrary superposition of ground (i.e., $|0\rangle$) and excited (i.e., $|1\rangle$) states such that

$$|\Psi\rangle = a|0\rangle + b|1\rangle, \tag{I.11}$$

and a field ionization detector can be used to measure $|\Psi\rangle$. In this case two measurement operators $M_0 = |0\rangle\langle 0|$ and $M_1 = |1\rangle\langle 1|$ are used. Then the probabilities of obtaining the measurement outcomes 0 and 1 from Eqns. (I.9) and (I.10) are respectively

$$p(0) = \langle\Psi|M_0^\dagger M_0|\Psi\rangle = |a|^2 \tag{I.12}$$

and

$$p(1) = \langle\Psi|M_1^\dagger M_1|\Psi\rangle = |b|^2. \tag{I.13}$$

Therefore post-measurement results for the two cases using Eqn. (I.10) are

$$\frac{M_0|\Psi\rangle}{|a|} = \frac{a}{|a|}|0\rangle, \tag{I.14}$$

and

$$\frac{M_1|\Psi\rangle}{|a|} = \frac{b}{|b|}|1\rangle. \tag{I.15}$$

Note that to determine the probabilities empirically we need an ensemble of identically prepared atoms (i.e., pure ensemble).

In Chapter V, we will use the above properties of quantum measurement to achieve both the teleportation and readout of an unknown or arbitrary quantum state of a two-level atom.

I.C Quantum Process Tomography

Closed quantum systems are immune to unwanted interactions with their environment. This leads to no noise showing up in these ideal quantum information processing systems. In practice, however, no such perfectly closed systems are available. Therefore it is essential to understand and control the noise mechanisms to build a scalable quantum computer. The "quantum operations formalism" is a powerful tool to achieve this task. It can not only be used to describe open systems but also be employed to study closed systems that are opened suddenly and subject to measurement.

The quantum operations formalism describes the evolution of quantum systems under various circumstances including stochastic processes. Unitary transformations and measurements are two simple examples of quantum operations. In general, we can denote a quantum operation as the map ε such that

$$\rho' = \varepsilon(\rho), \tag{I.16}$$

where ρ is the density operator for the quantum state being transformed. For a unitary transformation and measurements

$$\epsilon(\rho) = U\rho U^\dagger \tag{I.17}$$

and

$$\epsilon_m(\rho) = M_m \rho M_m^\dagger, \tag{I.18}$$

respectively. For example, consider the measurement as a quantum operation. Remember (see §1.B) that a quantum measurement can be described by a set of measurement operators $\{M_m\}$ that satisfies the completeness equation (I.8). If the state of the system immediately before the measurement is given by ρ, then the quantum operation (I.18) transforms the state immediately after the measurement into

$$\frac{\epsilon_m(\rho)}{\mathrm{tr}(\epsilon_m(\rho))}, \tag{I.19}$$

which is equivalent to Eqn. (I.10), since

$$p(m) = \mathrm{tr}(\epsilon_m(\rho)). \tag{I.20}$$

One application of quantum operations formalism is "quantum process tomography", a procedure to experimentally determine the dynamics of a quantum system. To understand process tomography, however, we first need to understand quantum state tomography, which is another procedure to experimentally determine an unknown quantum state. If we have only a single copy of the state to be measured, it is impossible to characterize. Therefore we need to repeat the experiment many times to produce a large number of copies of the same state. This is similar to the atomic state readout process that we will describe in Chapter V, where we repeat the teleportation protocol many times to produce identically prepared atoms to be detected.

Consider a single qubit density matrix ρ. We can expand ρ as

$$\rho = \frac{\mathrm{tr}(\rho)I + \mathrm{tr}(X\rho)X + \mathrm{tr}(Y\rho)Y + \mathrm{tr}(Z\rho)Z}{2}, \tag{I.21}$$

where I, X, Y, and Z are identity and Pauli matrices, respectively. The set $\frac{I}{\sqrt{2}}$, $\frac{X}{\sqrt{2}}$, $\frac{Y}{\sqrt{2}}$,$\frac{Z}{\sqrt{2}}$ forms an orthonormal set of matrices with respect to Hilbert-Schimidt

inner product. Remember that $\mathrm{tr}(A\rho)$ is the average value of the observable A. For example, if we measure Z a large number of times m, we can estimate the true value of $\mathrm{tr}(Z\rho)$ as $\sum_i z_i/m$ with standard deviation $1/\sqrt{m}$. z_i is the ith outcome of the measurement. Similarly we can estimate $\mathrm{tr}(X\rho)$ and $\mathrm{tr}(Y\rho)$ with a high level of confidence in the limit of large sample size.

Having described quantum state tomography, now we can use it to do process tomography. We will show how a useful representation for the dynamics of a quantum system may be experimentally determined using a systematic procedure. Our goal is to find a set of operation elements $\{E_i\}$ such that the map ε in Eqn. (I.16) has the form

$$\varepsilon(\rho) = \sum_i E_i \rho E_i^\dagger. \tag{I.22}$$

To determine E_i from measurable parameters, it is more convenient to use a fixed set of operators E_i', which form a basis for the set of operators in the state space, such that

$$E_i = \sum_m e_{im} E_m'. \tag{I.23}$$

where the e_{im}'s are complex numbers. Substituting Eqn. (I.23) into Eqn. (I.22) gives

$$\varepsilon(\rho) = \sum_{mn} E_m' \rho E_n'^\dagger \chi_{mn}, \tag{I.24}$$

where χ_{mn} is defined as

$$\chi_{mn} \equiv \sum_i e_{im} e_{in}^*. \tag{I.25}$$

Expression (I.24) shows that the map ε can be completely described by the χ matrix, once the set of operators E_i' has been fixed.

In the following we give the process tomography for a single qubit operation as an example. Given the experimental state tomography and preparation

procedures available in the laboratory, the dynamics of a multiple qubit quantum black box can be implemented numerically in a relatively straightforward way. For a single qubit case, for example, it is convenient mathematically to use the following set of fixed operators E_i'

$$E_0' = I, \tag{I.26}$$

$$E_1' = X, \tag{I.27}$$

$$E_2' = -iY, \tag{I.28}$$

$$E_3' = Z. \tag{I.29}$$

Here is the experimental procedure to do quantum process tomography. In a single qubit case the state space is $d = 2$ dimensional. Therefore, we choose $d^2 = 4$ pure states so that the corresponding density matrices ρ_1, ρ_2, ρ_3, and ρ_4 form a basis set for the state space. Once we determine this basis set, each state is subjected to the quantum process that we wish to characterize. After it is completed we obtain the density matrices $\rho_j' = \varepsilon(\rho_j)$ for each state $|\Psi_j\rangle$ using quantum state tomography as explained above. Knowing the ρ_js and the ρ_j's the χ matrix representation of the quantum process follows. The connection between these density matrices and the χ matrix is established through the equations:

$$E_m' \rho_j E_n'^{\dagger} = \sum_k \beta_{jk}^{mn} \rho_k, \tag{I.30}$$

$$\rho_j' = \sum_k \lambda_{jk} \rho_k, \tag{I.31}$$

$$\sum_{mn} \beta_{jk}^{mn} \chi_{mn} = \lambda_{jk}. \tag{I.32}$$

β_{jk}^{mn} and λ_{jk} can be determined from Eqns. (I.30) and (I.31), respectively, using standard linear algebra, and hence the χ matrix using Eqn. (I.32). Relation (I.32) gives the condition for the χ matrix, which describes the quantum operation ε.

Coming back to the single qubit case, we choose to prepare the input states $|0\rangle$, $|1\rangle$, $|+\rangle = (|0\rangle + |1\rangle)/\sqrt{2}$, $|-\rangle = (|0\rangle + i|1\rangle)/\sqrt{2}$ and we use the set of density matrices ρ_1, $\rho_2 = \rho_1 X$, $\rho_3 = X\rho_1$, and $\rho_4 = X\rho_1 X$, where ρ_1 is defined as

$$\begin{bmatrix} 1 & 0 \\ 0 & 0 \end{bmatrix}. \tag{I.33}$$

The quantum process that we want to characterize maps these density matrices into

$$\rho_1' = \varepsilon(|0\rangle\langle 0|) \tag{I.34}$$

$$\rho_2' = \varepsilon(|1\rangle\langle 1|) \tag{I.35}$$

$$\rho_3' = \varepsilon(|+\rangle\langle +|) - i\varepsilon(|-\rangle\langle -|) - (1-i)(\rho_1' + \rho_4')/2 \tag{I.36}$$

$$\rho_4' = \varepsilon(|+\rangle\langle +|) + i\varepsilon(|-\rangle\langle -|) - (1+i)(\rho_1' + \rho_4')/2 \tag{I.37}$$

and we can determine them from quantum state tomography. Once we know ρ_j and ρ_j's we can determine β and λ matrices from Eqns. (I.30) and (I.31), respectively, and hence the χ matrix that describes the two-qubit quantum process using Eqn. (I.32). After some algebra, due to the particular choice of basis, the χ matrix in this case can be expressed as

$$\chi = \Lambda \begin{bmatrix} \rho_1' & \rho_2' \\ \rho_3' & \rho_4' \end{bmatrix} \Lambda \tag{I.38}$$

in terms of block matrices and Λ is given as

$$\Lambda = \frac{1}{2}\begin{bmatrix} I & X \\ X & -I \end{bmatrix}. \tag{I.39}$$

I.D Atomic Interferometers

The first atom interferometers were demonstrated in the early 1990s. They were based on atomic diffraction from periodic microfabricated structures. Shortly afterwards, another class of atomic interferometers was developed by using optical light pulses. Here we will only consider single particle interferometry.

The physical system that we will study in Chapters IV and V operates in the microwave regime. Therefore, we assume below that internal and external degrees of freedom of a two-level atom are decoupled, because the momentum recoil of the atom due to the microwave photon is negligible in our analysis.

The Hamiltonian for the interaction of a two-level atom with an electromagnetic field can be written as

$$H = \hbar\omega_e|e\rangle\langle e| + \hbar\omega_g|g\rangle\langle g| - \mathbf{d}.\mathbf{E} \tag{I.40}$$

or in the matrix form

$$H = \begin{bmatrix} \hbar\omega_e & V_{eg} \\ V_{eg}^* & \hbar\omega_g \end{bmatrix}. \tag{I.41}$$

ω_e and ω_g are the excited and ground state energies of the two-level atom, respectively. The electromagnetic field operator $\mathbf{E}$ in Eqn. (I.40) is given by

$$\mathbf{E} = \mathbf{E}_0\cos(\omega_L t + \phi). \tag{I.42}$$

The last term in the Hamiltonian [Eqn. (I.40)],

$$\mathbf{V} = -\mathbf{d}.\mathbf{E} = -e\mathbf{r}.\mathbf{E}, \tag{I.43}$$

is the atom-electric dipole interaction term and its matrix element V_{eg} can be found using Eqns. (I.42) and (I.43) as

$$V_{eg} = \langle e|\mathbf{V}|g\rangle = \hbar\Omega_{eg}(\frac{e^{i(\omega_L t+\phi)} + e^{-i(\omega_L t+\phi)}}{2}), \tag{I.44}$$

where Ω_{eg} is called the Rabi frequency and is defined as

$$\Omega_{eg} = -\frac{\langle e|\mathbf{d}.\mathbf{E}_0|g\rangle}{\hbar}. \tag{I.45}$$

$\mathbf{r}$ in Eqn. (I.43) is the position of the electron in the two-level atom with respect to the nucleus.

The general solution to the Schrodinger equation (see Eqn. I.2) using the Hamiltonian (I.40) can be expressed as

$$|\Psi(t)\rangle = a_e(t)|e\rangle + a_g(t)|g\rangle. \tag{I.46}$$

The probability amplitudes $a_e(t)$ and $a_g(t)$ in Eqn. (I.46) can be written in the form

$$a_e(t) = c_e(t)e^{-i\omega_e t/2}, \tag{I.47}$$

$$a_g(t) = c_g(t)e^{-i\omega_g t/2}, \tag{I.48}$$

for mathematical convenience to separate the slowly varying functions of time $c_e(t)$ and $c_g(t)$. Using Eqns. (I.47) and (I.48) and the rotating wave approximation we can transform the matrix form of the Hamiltonian in Eqn. (I.41) into

$$H_r = \frac{\hbar}{2}\begin{bmatrix} 0 & \Omega_{eg}e^{-i(\delta t+\phi)} \\ \Omega^*_{eg}e^{i(\delta t+\phi)} & 0 \end{bmatrix}. \tag{I.49}$$

$\delta \equiv \omega_L - \omega_{eg}$ is the laser-atom detuning, where $\omega_{eg} \equiv \omega_e - \omega_g$. Note that the transformed Hamiltonian in Eqn. (I.49) is time-dependent. Under the following transformation of variables it can be made time-independent:

$$c_e(t) = d_e(t)e^{-i\delta t/2}, \tag{I.50}$$

$$c_g(t) = d_g(t)e^{i\delta t/2}. \tag{I.51}$$

Transformations (I.50) and (I.51) physically mean that the quantum state rotates around the **z**-axis with a frequency δ. Similarly, the transformation from the Schrodinger picture into the interaction picture can be interpreted as a rotating frame with a frequency ω_{eg}. Therefore our time-independent Hamiltonian incorporates both transformations.

The transformation of a quantum state $|\Psi\rangle$ into a rotating frame with frequency δ around the **z**-axis is described by a rotation operator $D(\mathbf{z}, -\delta t)$ such that

$$D(\mathbf{z}, -\delta t)|\Psi\rangle = |\Psi\rangle_R. \tag{I.52}$$

The representation of the rotation operator in matrix form can be written as

$$D(\mathbf{z}, -\delta t) = e^{i\sigma_z \delta t/2} = \begin{bmatrix} e^{i\delta t/2} & 0 \\ 0 & e^{-i\delta t/2} \end{bmatrix}, \tag{I.53}$$

where σ_z is the Pauli matrix.

Now, let's find the time-independent Hamiltonian by transforming the Schrodinger equation into the rotating frame. We can express the Schrodinger equation as

$$i\hbar\frac{d}{dt}(D^\dagger|\Psi\rangle_R) = H(D^\dagger|\Psi\rangle_R). \tag{I.54}$$

Multiplying both sides with D from the left and rearranging the equation gives

$$i\hbar\frac{d}{dt}|\Psi\rangle_R = [DHD^\dagger - i\hbar D(\frac{dD^\dagger}{dt})]|\Psi\rangle_R. \tag{I.55}$$

Thus the effective Hamiltonian in the square brackets can be defined as the Hamiltonian in the rotating frame. It can be represented by the matrix

$$H_R = \frac{\hbar}{2}\begin{bmatrix} -\delta & \Omega_{eg}e^{-i\phi} \\ \Omega^*_{eg}e^{i\phi} & \delta \end{bmatrix}. \tag{I.56}$$

The eigenvalues of this Hamiltonian are

$$\lambda_\pm = \pm\frac{\hbar\Omega_r}{2}, \tag{I.57}$$

where $\Omega_r \equiv \sqrt{|\Omega_{eg}|^2 + \delta^2}$ is the off-resonant Rabi frequency. The phase ϕ in Eqn. (I.56) can be incorporated into Ω_{eg} to make it positive and real. Then the eigenstates of H_R can be calculated to be

$$|\lambda_+\rangle = \cos(\frac{\theta}{2})|e\rangle_R \mathrm{e}^{-i\phi/2} + \sin(\frac{\theta}{2})|g\rangle_R \mathrm{e}^{i\phi/2} \tag{I.58}$$

and

$$|\lambda_-\rangle = \text{-}\sin(\frac{\theta}{2})|e\rangle_R \mathrm{e}^{-i\phi/2} + \cos(\frac{\theta}{2})|g\rangle_R \mathrm{e}^{i\phi/2}, \tag{I.59}$$

where $\sin(\theta) = \Omega_{eg}/\Omega_r$, $\cos(\theta) = -\delta/\Omega_r$ and $0 \le \theta \le \pi$. Then the time evolution of the state $|\Psi(t_0)\rangle_R$ can be written as

$$|\Psi(t_0+\tau)\rangle_R = (\mathrm{e}^{-i\lambda_+\tau/\hbar}|\lambda_+\rangle\langle\lambda_+| + \mathrm{e}^{-i\lambda_-\tau/\hbar}|\lambda_-\rangle\langle\lambda_-|)|\Psi(t_0)\rangle_R. \tag{I.60}$$

For $\delta = 0$ and constant field amplitude the evolution operator can be expressed in the matrix form as

$$U_R = \begin{bmatrix} \cos(\Omega_r\tau/2) & -i\mathrm{e}^{-i\phi}\sin(\Omega_r\tau/2) \\ -i\mathrm{e}^{i\phi}\sin(\Omega_r\tau/2) & \cos(\Omega_r\tau/2) \end{bmatrix}. \tag{I.61}$$

When the initial state is the ground state and it is subjected to two pulses of area $\int \Omega_r(t)dt = \Omega_r\tau = \pi/2$, we obtain the excited state if the atomic oscillation in between the two $\pi/2$ pulses is the same as the microwave oscillator (i.e., $\delta T = n\pi$,

where T is time elapsed between two pulses and n is an even integer). If there is a phase difference $m\pi$ (m is odd), the atom is left in the ground state. Thus interference creates an oscillation between the excited and ground states of the atom.

I.D.1 Ramsey Interferometer

Assume an oscillator frequency

$$\nu_0 = (W_q - W_p)/2\pi\hbar \tag{I.62}$$

at which a resonance transition between states of energy W_p and W_q occurs. In practice not only the resonance frequency but also the width of the resonance is important, because the linewidth affects the transition probabilities, although the maximum transition occurs at the oscillator frequency (I.62).

We can give a qualitative physical description of the resonance process by considering a magnetic moment associated with a large angular momentum such that the problem can be treated classically. Consider that such a magnetic moment enters a region with a static magnetic field H_0. Then the magnetic moment will precess around H_0 with the Larmor frequency

$$\omega_0 = \frac{\mu_I}{\hbar I} H_0, \tag{I.63}$$

where μ_I is the z-component of the nuclear magnetic moment and I is the nuclear spin quantum number. When H_1, a weak magnetic field perpendicular to the axis of H_0 and rotating around it, is added, the magnetic moment also precesses around H_1. This changes the angle ϕ between the nuclear magnetic moment and $\mathbf{H}_0$. If H_1 rotates faster than the Larmor frequency (I.63), angle ϕ on the average does not change. When it rotates at a frequency equal to the Larmor frequency, however, there is a net angle ϕ accumulated.

Below we will calculate the transition probability between two states $|p\rangle$

and $|q\rangle$ of an atom with a magnetic moment subject to an oscillatory perturbation V. We can write the matrix elements of V as

$$V_{pq} = \langle p|V|q\rangle = \hbar b e^{i\omega t}, \tag{I.64}$$

$$V_{qp} = V_{pq}^{*}, \tag{I.65}$$

$$V_{pp} = V_{qq} = 0, \tag{I.66}$$

where ω is the rate of rotation of the magnetic field around the axis of quantization and b is proportional to the magnetic field.

The quantum state of the system that makes transitions between $|p\rangle$ and $|q\rangle$ can be written at time t as

$$|\Psi(t)\rangle = C_p(t)|\Psi_p\rangle + C_q(t)|\Psi_q\rangle, \tag{I.67}$$

and the Schrödinger equation for above Hamiltonian can be expressed as

$$i\hbar\frac{\partial}{\partial t}|\Psi(t)\rangle = \mathcal{H}_0|\Psi(t)\rangle + V|\Psi(t)\rangle. \tag{I.68}$$

Multiplying Eqn. (I.68) by $\langle\Psi_p|$ and $\langle\Psi_q|$ gives

$$i\hbar\frac{\partial}{\partial t}C_p(t) = W_p C_p(t) + \hbar b e^{i\omega t} C_q(t) \tag{I.69}$$

and

$$i\hbar\frac{\partial}{\partial t}C_q(t) = \hbar b e^{-i\omega t} C_p(t) + W_q C_q(t), \tag{I.70}$$

respectively. Assuming the initial conditions $C_p(0) = 1$ and $C_q(0) = 0$, the solution at time t can be found as

$$C_p(t) = [i\cos\Theta\sin(\frac{at}{2}) + \cos(\frac{at}{2})]\mathrm{e}^{i[\omega/2-(W_p+W_q)/2\hbar]t}, \tag{I.71}$$

$$C_q(t) = i\sin\Theta\sin(\frac{at}{2})\mathrm{e}^{i[-\omega/2-(W_p+W_q)/2\hbar]t}, \tag{I.72}$$

where

$$\cos\Theta = (\omega_0 - \omega)/a, \tag{I.73}$$

$$\sin\Theta = -2b/a, \tag{I.74}$$

$$a^2 = [(\omega_0 - \omega)^2 + (2b)^2], \tag{I.75}$$

$$\omega_0 = (W_q - W_p)/\hbar. \tag{I.76}$$

Then the probability of a transition from state $|\Psi_p\rangle$ to state $|\Psi_q\rangle$ by time t is $|C_q(t)|^2$ or

$$P_{p,q} = \frac{(2b)^2}{(\omega_0 - \omega)^2 + (2b)^2}\sin^2\{\frac{t}{2}[(\omega_0 - \omega)^2 + (2b)^2]^{1/2}\}. \tag{I.77}$$

Note that at resonance (i.e., when $\omega = \omega_0$) the first factor in Eqn. (I.77) reaches unity.

One of the approximations in the preceding calculations is the omission of possible oscillatory diagonal elements in Eqn. (I.66). The effects of such oscillatory diagonal elements are negligible near resonance.

Ramsey pointed out that approximately uniform intensity throughout the regions of the apparatus was not the most advantageous method of applying the oscillatory field. Rather, amplitude and phase of the oscillating field could be varied to obtain more useful resonances. A particular arrangement that is more useful in many cases is separated oscillatory fields, where two oscillatory fields are confined tightly in two separate locations.

Consider again a magnetic moment (with a large angular momentum to treat the problem classically) which enters a region with strong uniform magnetic

field $\mathbf{H}_0$ at the entrance and exit ends of which there is a weak magnetic field perpendicular to $\mathbf{H}_0$ and rotating about an axis parallel to it. If the angular momentum is initially aligned with the field so that $\phi = 0$, we can tune it to $\phi = \pi/2$ by applying a weak rotating field with a certain amplitude and period of time in the first oscillating region. In the intermediate region of no rotating field the magnetic moment simply precesses with the Larmor frequency (I.63). When it proceeds to the next oscillatory region, however, ϕ starts to change again. If the frequency of the second rotating field is exactly the same as the mean Larmor frequency in the intermediate region, no relative phase shift occurs between the angular momentum and the rotating field. Then, with the magnitude of the rotating field and the time of application equal to those of the first oscillatory region, ϕ increases by another $\pi/2$, making $\phi = \pi$. If the phase shift between the precessing angular momentum and the rotating field is π, the second oscillating field reverses the effect of the first oscillatory field, returning to $\phi = 0$. If the Larmor frequency and the frequency of the rotating field differs in such a way that the phase shift in the intermediate region is an integral multiple of 2π, then ϕ will be the same as at the exact resonance, which is π.

Below we will find the transition probability for a single atom passing through two separated oscillating fields. A more general solution to Eqns. (I.69) and (I.70) can be obtained by considering that the atom enters the oscillatory region at time t_1 with probability amplitudes $C_p(t_1)$ and $C_q(t_1)$ and exits at time $t_1 + T$. Under these initial conditions the solution to Eqns. (I.69) and (I.70) is

$$\begin{aligned} C_p(t_1+T) &= [(i\cos\Theta\sin\frac{aT}{2} + \cos\frac{aT}{2})C_p(t_1) \\ &\quad +(i\sin\Theta\sin\frac{aT}{2}\mathrm{e}^{i\omega t_1})C_q(t_1)]\mathrm{e}^{\{i[\omega/2-(W_p+W_q)/2\hbar]T\}}, \end{aligned} \tag{I.78}$$

$$\begin{aligned} C_q(t_1+T) &= [(i\sin\Theta\sin\frac{aT}{2}\mathrm{e}^{-i\omega t_1})C_p(t_1) \\ &\quad +(-i\cos\Theta\sin\frac{aT}{2} + \cos\frac{aT}{2})C_q(t_1)]\mathrm{e}^{\{i[-\omega/2-(W_p+W_q)/2\hbar]T\}}. \end{aligned} \tag{I.79}$$

For the special case of $b = 0$, Eqns. (I.78) and (I.79) reduce to

$$C_p(t_1 + T) = \mathrm{e}^{[-i(W_p/\hbar)T]} C_p(t_1) \tag{I.80}$$

$$C_q(t_1 + T) = \mathrm{e}^{[-i(W_q/\hbar)T]} C_q(t_1). \tag{I.81}$$

Now let's consider a single atom crossing two separated oscillatory regions in which the perturbation of Eqns. (I.64)-(I.66) occurs. Both regions have width l and take time τ for the atom to traverse. In between the two oscillatory regions no perturbation exists (i.e., $b = 0$). We assume, however, that the energies of the states $|\Psi_p\rangle$ and $|\Psi_q\rangle$ are different in each sub-region of the intermediate region such that the kth sub-region of duration Δt_k has the energies $W_{p,k}$ and $W_{q,k}$. Then, using Eqns. (I.78) and (I.79) and the initial conditions $C_p(0) = 1$ and $C_q(0) = 0$, we obtain at time τ when the atoms reach the entrace to the first oscillatory region,

$$C_p(\tau) = (i\cos\Theta\sin\frac{a\tau}{2} + \cos\frac{a\tau}{2})\mathrm{e}^{i[\omega/2 - (W_p + W_q)/2\hbar]\tau}, \tag{I.82}$$

$$C_q(\tau) = i\sin\Theta\sin\frac{a\tau}{2}\mathrm{e}^{i[-\omega/2 - (W_p + W_q)/2\hbar]\tau}. \tag{I.83}$$

The first oscillatory region is followed by the intermediate region (i.e., $b = 0$) in which the atom propagates until time $\tau + T$. Then, the transition probability amplitudes can be found as

$$C_p(\tau + T) = \prod_k \mathrm{e}^{-iW_{p,k}\Delta_{t,k}/\hbar} C_p(\tau) = \mathrm{e}^{-(i/\hbar)\sum_k W_{p,k}\Delta_{t,k}} C_p(\tau) = \mathrm{e}^{-i\overline{W}_p T/\hbar} C_p(\tau), \tag{I.84}$$

$$C_q(\tau + T) = \mathrm{e}^{-i\overline{W}_q T/\hbar} C_q(\tau), \tag{I.85}$$

Once the atom exits the intermediate region, it enters the second oscillatory region which takes an additional time τ. Then, we obtain the final probability amplitudes at time $2\tau + T$ as

$$C_p(2\tau+T) = [(i\cos\Theta\sin\frac{a\tau}{2}+\cos\frac{a\tau}{2})C_p(\tau+T) + i\sin\Theta\sin\frac{a\tau}{2}e^{i\omega(\tau+T)}C_q(\tau+T)]e^{i[\omega/2-(W_p+W_q)/2\hbar]\tau}, \quad \text{(I.86)}$$

$$C_q(2\tau+T) = [i\sin\Theta\sin\frac{a\tau}{2}e^{-i\omega(\tau+T)}C_p(\tau+T) + (-i\cos\Theta\sin\frac{a\tau}{2} + \cos\frac{a\tau}{2})C_q(\tau+T)]e^{i[-\omega/2-(W_p+W_q)/2\hbar]\tau}. \quad \text{(I.87)}$$

We can rewrite Eqn. (I.87) by eliminating C_p and C_q as

$$C_q(2\tau+T) = -2i\sin\Theta(\cos\Theta\sin^2\frac{a\tau}{2}\sin\frac{\lambda T}{2} - \frac{1}{2}\sin a\tau\cos\frac{\lambda T}{2}) \times e^{-i[(\omega/2+(W_p+W_q)/2\hbar)(2\tau+T)+[(\overline{W}_p-W_p+\overline{W}_q-W_q)/2\hbar]T]}, \quad \text{(I.88)}$$

where

$$\lambda = [(\overline{W}_q - \overline{W}_p)/\hbar] - \omega. \quad \text{(I.89)}$$

Using Eqn. (I.88), we can write the transition probability of the atom from state $|\Psi_p\rangle$ to $|\Psi_q\rangle$ as

$$P_{p,q} = |C_q(2\tau+T)|^2 = 4\sin^2\Theta\sin^2\frac{a\tau}{2}(\cos\frac{\lambda T}{2}\cos\frac{a\tau}{2} - \cos\Theta\sin\frac{\lambda T}{2}\sin\frac{a\tau}{2})^2. \quad \text{(I.90)}$$

I.E Decoherence

There is no known evidence of conflict between the experiments and the predictions of quantum mechanics. There is, however, continuing debate on the relation of quantum mechanics with our familiar physical world.

The emergence of classical behavior from quantum dynamics can be understood by studying the quantum apparatus for measurement that was analyzed

by John von Neumann. Consider a two-level quantum sytem $\mathcal{S}$ and a detector $\mathcal{D}$. The Hilbert space $\mathcal{H}_{\mathcal{S}}$ of the system is spanned by $|\uparrow\rangle$ and $|\downarrow\rangle$. $|d_\uparrow\rangle$ and $|d_\downarrow\rangle$ span the Hilbert space $\mathcal{H}_{\mathcal{D}}$ of the detector. A quantum detector can be devised, for example, in such a way that the detector changes its state when the system is in state $|\uparrow\rangle$ only:

$$|\uparrow\rangle|d_\downarrow\rangle \rightarrow |\uparrow\rangle|d_\uparrow\rangle \tag{I.91}$$

Assume a pure state

$$|\Psi_{\mathcal{S}}\rangle = \alpha|\uparrow\rangle + \beta|\downarrow\rangle. \tag{I.92}$$

Initially if we express the composite system in the form $|\Psi_{\mathcal{S}}\rangle|d_\downarrow\rangle$, it evolves into a correlated state $|\Phi^c\rangle$, which can be expressed as

$$|\Phi^c\rangle = \alpha|\uparrow\rangle|d_\uparrow\rangle + \beta|\downarrow\rangle|d_\downarrow\rangle. \tag{I.93}$$

Correlation in Eqn. (I.93) implies that if the detector is found in $|d_\uparrow\rangle$, then the system is thrown into $|\uparrow\rangle$ state. When the detector gives $|d_\downarrow\rangle$ state, the system is in $|\downarrow\rangle$ state. To illustrate environment-induced decoherence, consider also the environment as a quantum system $\mathcal{E}$. The environment also interacts, and becomes correlated, with $|\Phi^c\rangle$,

$$|\Phi^c\rangle|\mathcal{E}_0\rangle = (\alpha|\uparrow\rangle|d_\uparrow\rangle + \beta|\downarrow\rangle|d_\downarrow\rangle)|\mathcal{E}_0\rangle \mapsto \alpha|\uparrow\rangle|d_\uparrow\rangle|\mathcal{E}_\uparrow\rangle + \beta|\downarrow\rangle|d_\downarrow\rangle|\mathcal{E}_\downarrow\rangle = |\Psi\rangle. \tag{I.94}$$

When the states of the environment corresponding to the detector states $|d_\uparrow\rangle$ and $|d_\downarrow\rangle$ are orthogonal, we can obtain the reduced density matrix for the system-detector composite state by tracing over the environment in the complete density matrix,

$$\rho_{\mathcal{DS}} = Tr_{\mathcal{E}}|\Psi\rangle\langle\Psi| = \sum_i \langle\mathcal{E}_i|\Psi\rangle\langle\Psi|\mathcal{E}_{i'}\rangle = |\alpha|^2|\uparrow\rangle\langle\uparrow||d_\uparrow\rangle\langle d_\uparrow| + |\beta|^2|\downarrow\rangle\langle\downarrow||d_\downarrow\rangle\langle d_\downarrow|. \tag{I.95}$$

When a stone falls into a lake, it creates ripples on the surface of the lake, which is otherwise flat. Similarly when a particle exists in the electromagnetic sea the field excitations scatter off the particle and carry information about its quantum observables such as position, momentum, energy, etc. Surprisingly, in quantum mechanics even in a storm the stone thrown into the lake creates disturbances that can be detected, despite the difficulty of deciphering the particle due to the preexisting fields in such a "messy environment".

Below we will illustrate the decoherence by giving an example. We will consider the interaction of a particle at position x that is subject to a scalar field. The Hamiltonian for such a system can be described by

$$H_{int} = \varepsilon x \frac{\mathrm{d}\phi}{\mathrm{d}t}, \tag{I.96}$$

where ϕ is a scalar field and $\varepsilon^2/2$ is the "viscosity". We take thermal-excitation effects of the field ϕ into account and neglect the effect of zero point vacuum fluctuations. Then, in the "high temperature limit" the position representation of the density matrix $\rho(x, x')$ evolves as

$$\frac{\mathrm{d}\rho}{\mathrm{d}t} = -\frac{i}{\hbar}[H, \rho] - \gamma(x - x')(\frac{\partial}{\partial x} - \frac{\partial}{\partial x'})\rho - \frac{2m\gamma k_B T}{\hbar^2}(x - x')^2\rho. \tag{I.97}$$

H is the Hamiltonian for the system. γ, m, k_B, and T are the relaxation constant, mass of the particle, the Boltzman constant, and temperature, respectively. Eqn. (I.97) is obtained by solving the Schrodinger equation for a particle in a field and tracing over the environment (i.e., field) such as in Eqn. (I.95). The first term (i.e., von Neumann equation) describes the reversible classical evolution of the expected value of an observable that has a classical counterpart. The second term is the relaxation or dissipation term. It is responsible for the decrease of the average momentum or energy loss due to the interaction with the scalar field. The relaxation term is proportional to the relaxation constant $\gamma = \eta/2m$, where η is the viscosity. The last term is the "decoherence" term. Below we will explain it

in more detail by an example.

For our purposes the effect of the last term on the coherence of quantum superposition states is the greatest interest. Now we will briefly describe the effect of this term on a quantum superposition of two spatially separated wavepackets by studying the off-diagonal elements of the density matrix.

Consider a coherent quantum superposition of two Gaussian wavefunctions separated by Δx,

$$\phi(x) = [\chi^+(x) + \chi^-(x)]/\sqrt{2}, \tag{I.98}$$

where $\chi^{\pm}(x)$ are defined as

$$\chi^{\pm}(x) = \langle x|\pm\rangle \sim \mathrm{e}^{-(x\pm\Delta x)^2/(2\delta)^2}. \tag{I.99}$$

If the wavepackets are widely separated (i.e., $\Delta x \gg \delta$), the density matrix $\rho(x,x') = \phi(x)\phi^*(x')$ has four peaks on the xx'plane. Those peaks which are centered on the line $x = x'$ form the diagonal elements. Off-diagonal peaks (or elements) lie in the two other quadrants on the line $x = -x'$ passes. The amplitudes of these off-diagonal elements describe how coherent is the superposition state. If their amplitudes are large enough then the particle is in a highly coherent quantum superposition. If their amplitudes are zero, however, it can be regarded as a classical probability distribution with an equal probability of finding the particle in either of the locations of the Gaussian wavepackets.

The decoherence term (i.e., last term) in Eqn. (I.97) has little effect on the diagonal peaks, but it largely affects the off-diagonal peaks. Note that decoherence is proportional to $(x-x')^2$, which is approximately equal to the square of the separation $(\Delta x)^2$. The time scale for the decoherence can be given as

$$\tau_D \simeq \frac{1}{\gamma}\left(\frac{\lambda_{DB}}{\Delta x}\right)^2 = \tau_R\left(\frac{\hbar}{\Delta x\sqrt{2mk_BT}}\right)^2, \tag{I.100}$$

where $\lambda_{DB} = \hbar/\sqrt{2mk_BT}$ is the de Broglie wavelength and $\tau_R = 1/\gamma$ is the re-

laxation time. For macroscopic objects decoherence time is typically much less than the relaxation time, $\tau_D \ll \tau_R$. For microscopic systems, however, the decoherence time is relatively long. For an electron ($m_e = 10^{-27} kg$), for example, the decoherence time can be much larger than other relevant time scales.

There are two roles of decoherence in quantum information processing. It invalidates the quantum superposition principle and therefore negates the potential power of quantum computers by turning them into classical ones at best. But, on the other hand, it is also a necessary ingredient for quantum information processing to achieve quantum measurement.

In the last decade decoherence was studied experimentally in many physical systems by several groups and the results confirmed the thoretical tenets. In particular, Brune, Haroche, Raimond, and their coworkers in France manipulated electromagnetic fields in the microwave region into Schrödinger cat-like superposition states using Rb atoms and they investigated the ensuing loss of quantum coherence. Since then the group upgraded their equipment to grow "bigger and better" cats. They have very recently reported the observation of step-by-step quantum state collapse by non-destructively measuring the photon number of a field stored in a cavity using atoms.

Chapter II

Quantum Computation and Communication

Most of the material in this chapter is visited by Nielsen and Chuang in more depth in Ref. [2]. Therefore, for more details of the concepts introduced here and for many helpful references please see this excellent introduction to "quantum computation and quantum information".

II.A Quantum Logic Gates

Quantum logic gates perform manipulation of quantum information from one form into another. Imagine a physical process which converts the $|0\rangle$ state into the $|1\rangle$ state, and vice versa. Although this physical process can be employed to implement a classical `NOT` gate (only non-trivial single bit logic gate) it is insufficient as a quantum logic gate. The analogous quantum `NOT` gate has to operate not only on classical states but also on their quantum superpositions $\alpha|0\rangle + \beta|1\rangle$ in a linear manner. This linear behaviour is the general property of quantum meachanics.

The matrix representation of the `NOT` gate can be given as

$$X = \begin{bmatrix} 0 & 1 \\ 1 & 0 \end{bmatrix}. \tag{II.1}$$

If we represent an arbitrary single qubit in the vector form

$$\begin{bmatrix} \alpha \\ \beta \end{bmatrix}, \tag{II.2}$$

with the upper element corresponding to the probability amplitude for $|0\rangle$ and the lower one the probability amplitude for $|1\rangle$, then the operation of the quantum `NOT` gate can be described as

$$X \begin{bmatrix} \alpha \\ \beta \end{bmatrix} = \begin{bmatrix} \beta \\ \alpha \end{bmatrix}. \tag{II.3}$$

Single qubit quantum gates U, in general, can be described by two by two unitary matrices, that is $UU^\dagger = I$. Note that the normalization condition requires

$$|\alpha|^2 + |\beta|^2 = |\alpha'|^2 + |\beta'|^2 = 1, \tag{II.4}$$

where α' and β' correspond to the output of the quantum logic gate. Unitarity guarantees the normalization condition.

In contrast to the classical gates, there are many non-trivial single qubit gates. Some important ones are Pauli `X`, `Y`, `Z` gates and Hadamard gate. `Z` gate, for example, transforms $|1\rangle$ into $-|1\rangle$ (second column below) while it leaves $|0\rangle$ (first column) unchanged. Two by two Pauli matrices for these gates are

$$\mathtt{X} \equiv \begin{bmatrix} 0 & 1 \\ 1 & 0 \end{bmatrix};\ \mathtt{Y} \equiv \begin{bmatrix} 0 & -i \\ i & 0 \end{bmatrix};\ \mathtt{Z} \equiv \begin{bmatrix} 1 & 0 \\ 0 & -1 \end{bmatrix}. \tag{II.5}$$

The Hadamard gate creates an equal superposition from an input state $|0\rangle$ or $|1\rangle$. It transforms $|0\rangle$ state into $(|0\rangle + |1\rangle)/\sqrt{2}$ and $|1\rangle$ into $(|0\rangle - |1\rangle)/\sqrt{2}$:

$$\mathtt{H} = \frac{1}{\sqrt{2}} \begin{bmatrix} 1 & 1 \\ 1 & -1 \end{bmatrix}. \tag{II.6}$$

A single qubit $a|0\rangle + b|1\rangle$ can be represented as a point (θ, ϕ) on the unit sphere, called the Bloch sphere, where $a = \cos(\theta/2)$ and $b = \mathrm{e}^{i\phi}\sin(\theta/2)$ and the vector $(\cos\phi\sin\theta, \sin\phi\sin\theta, \cos\theta)$ is called the Bloch vector.

An arbitrary single qubit gate can be decomposed into a product of two rotations and a global phase shift, that is

$$\mathrm{e}^{i\alpha}\begin{bmatrix} \mathrm{e}^{-i\beta/2} & 0 \\ 0 & \mathrm{e}^{i\beta/2} \end{bmatrix}\begin{bmatrix} \cos\frac{\gamma}{2} & -\sin\frac{\gamma}{2} \\ \sin\frac{\gamma}{2} & \cos\frac{\gamma}{2} \end{bmatrix}. \tag{II.7}$$

An important classical theoretical result is that any function on multiple bits can be computed by using `NAND` gates alone. Therefore the `NAND` gate is a universal gate. In contrast to classical computation, any multiple qubit logic gate may be composed from `CNOT` and single qubit gates. Single qubit gates can be further approximated to arbitrary accuracy using the Hadamard, phase, and $\pi/8$ gates. Matrices for the phase and $\pi/8$ gates, respectively, are

$$\mathtt{S} = \begin{bmatrix} 1 & 0 \\ 0 & i \end{bmatrix};\ \mathtt{T} = \begin{bmatrix} 1 & 0 \\ 0 & \mathrm{e}^{i\pi/4} \end{bmatrix}. \tag{II.8}$$

`CNOT` gate has two inputs: control and target qubits. If the control qubit is in the $|1\rangle$ state, the target qubit is flipped, whereas it is left unchanged when the control qubit is in $|0\rangle$ state, that is

$$|A, B\rangle \rightarrow |A, A \oplus B\rangle, \tag{II.9}$$

where $\oplus$ is addition modulo two, which is exactly how `XOR` gate operates. Similar to single qubit gates, `CNOT` gate is also a unitary gate to conserve probability.

II.B Quantum Circuits

Quantum circuits are useful as models of quantum processes such as computation, communication, and even quantum noise. A simple quantum circuit which swaps the states of qubits can be constructed by integrating three `CNOT`

gates properly. In this quantum circuit the following actions take place sequentially:

$$|a,b\rangle \rightarrow |a,a\oplus b\rangle \rightarrow |a\oplus(a\oplus b),a\oplus b\rangle = |b,a\oplus b\rangle \rightarrow |b,(a\oplus b)\oplus b\rangle = |b,a\rangle. \quad \text{(II.10)}$$

Measurement is an important part of quantum circuits. It converts the input qubit $|\Psi\rangle = \alpha|0\rangle + \beta|1\rangle$ into one of the classical bits M probabilistically. M can be 0 with probability $|\alpha|^2$ and 1 with probability $|\beta|^2$. Measurement is represented by a "meter" symbol in quantum circuits.

Classically we can copy a bit using a classical `CNOT` gate such that

$$|x,0\rangle \mapsto |x,x\oplus 0\rangle = |x,x\rangle. \quad \text{(II.11)}$$

Suppose we try to copy an unknown qubit $|\Psi\rangle = a|0\rangle + b|1\rangle$ in the same manner using quantum `CNOT` gate, that is

$$(a|0\rangle + b|1\rangle)|0\rangle = a|00\rangle + b|10\rangle \rightarrow a|00\rangle + b|11\rangle. \quad \text{(II.12)}$$

A successful quantum copying circuit should, however, generate

$$|\Psi\rangle|\Psi\rangle = a^2|00\rangle + ab|01\rangle + ab|10\rangle + b^2|11\rangle. \quad \text{(II.13)}$$

Therefore, quantum `CNOT` gate cannot produce the copy of an unknown quantum state unless $ab = 0$. This is known as the "no-cloning theorem".

II.C Quantum Entanglement

Quantum entanglement is a new type of resource for information theory that differs vastly from the traditional resources in classical information theory. A general theory of quantum entanglement has still not been completed, despite some encouraging progress in the field. Understanding the difference between quantum mechanics and the classical world is crucial for quantum information processing to

harvest its potential power in computing and communications. Quantum entanglement is one compelling example of this difference.

In our classical world when we speak of an object we assume that its physical properties exist independently of observation. Quantum mechanically, however, an unobserved particle does not possess physical properties that exist independently of observation.

Consider, for example, the spin singlet, a two qubit entangled state,

$$|\Psi\rangle = \frac{|01\rangle - |10\rangle}{\sqrt{2}}. \tag{II.14}$$

Suppose we measure the spin along the $\vec{v}$ axis on both qubits. When the measurement yields $+1$ on the first qubit, then the measurement on the second qubit will give -1, and vice versa, regardless of the $\vec{v}$ axis we chose. It is simple to show why this anti-correlation is independent of the measurement axis. Suppose that $|a\rangle$ and $|b\rangle$ are the eigenstates of the spin. Then we can express $|0\rangle$ and $|1\rangle$ states in Eqn. (II.13) as

$$|0\rangle = \alpha|a\rangle + \beta|b\rangle \tag{II.15}$$

$$|1\rangle = \gamma|a\rangle + \delta|b\rangle, \tag{II.16}$$

where α, β, γ, and δ are complex numbers. Substituting Eqns. (II.15) and (II.16) into Eqn. (II.14) gives

$$\frac{|01\rangle - |10\rangle}{\sqrt{2}} = (\alpha\delta - \beta\gamma)\frac{|ab\rangle - |ba\rangle}{\sqrt{2}}. \tag{II.17}$$

Note that $\alpha\delta - \beta\gamma$ is nothing more than a global factor which cannot be observed. So it is clear that the anti-correlation above is independent of measurement axis.

Now by using the singlet state in Eqn. (II.14), we will show below that quantum mechanical analysis is not consistent with the common sense analysis.

Imagine that Charlie sends a particle to Alice and another to Bob. Alice can measure the physical properties P_Q and P_R of her particle, while Bob is allowed to measure P_S and P_T for his own particle. Q and R are the objective values of the physical properties P_Q and P_R, respectively, that Alice can obtain. Similarly, S and T correspond to Bob's measurement. Suppose that Alice and Bob randomly but simultaneously perform series of available measurements in their toolbox. For simplicity, we assume that all of these measurements reveal either $+1$ or -1.

Now consider the quantity

$$QS + RS + RT - QT = (Q + R)S + (R - Q)T. \tag{II.18}$$

Because $R, Q = \pm 1$, either $(Q+R)S = 0$ or $(R-Q)T = 0$. In both cases $QS + RS + RT - QT = \pm 2$. Assume that initially (i.e., before the measurement) the system is in a state where $Q = q$, $R = r$, $S = s$, and $T = t$. Then, the expectation value

$$\mathrm{E}(QS + RS + RT + QT) = \sum_{qrst} p(q, r, s, t)(qs + rs + rt - qt) \leq \sum_{qrst} 2p(q, r, s, t) = 2. \tag{II.19}$$

We can also express this as

$$\begin{aligned} \mathrm{E}(QS + RS + RT - QT) &= \sum_{qrst} p(q, r, s, t)qs + \sum_{qrst} p(q, r, s, t)rs \\ &\quad + \sum_{qrst} p(q, r, s, t)rt - \sum_{qrst} p(q, r, s, t)qt \\ &= \mathrm{E}(QS) + \mathrm{E}(RS) + \mathrm{E}(RT) - \mathrm{E}(QT). \end{aligned} \tag{II.20}$$

Comparing Eqns. (II.19) and (II.20) gives the Bell inequality

$$\mathrm{E}(QS) + \mathrm{E}(RS) + \mathrm{E}(RT) - \mathrm{E}(QT) \leq 2. \tag{II.21}$$

To find the expectation value, say QS, Alice measures P_Q and Bob measures P_S. Then they multiply their results. Alice and Bob perform this experiment a number

of times and average over their sample.

How about quantum systems? Consider, for example, the singlet state in Eqn. (II.14). Charlie prepares this entangled state and passes each of Alice and Bob one of the two qubits. Having received their qubit, Alice and Bob measure the following observables

$$Q = Z;\ R = X;\ S = \frac{-Z - X}{\sqrt{2}};\ T = \frac{Z - X}{\sqrt{2}}. \tag{II.22}$$

The quantum expectation values for these obsevables can be found as

$$\langle QS \rangle = \langle RS \rangle = \langle RT \rangle = \frac{1}{\sqrt{2}};\ \langle QT \rangle = -\frac{1}{\sqrt{2}}, \tag{II.23}$$

hence

$$\langle QS \rangle + \langle RS \rangle + \langle RT \rangle - \langle QT \rangle = 2\sqrt{2}. \tag{II.24}$$

Note that Eqn. (II.24) does not satisfy the Bell inequality in Eqn. (II.21). It seems that at least one of the two assumptions we made does not hold in quantum mechanics:

1. Physical properties P_Q, P_R, P_S, and P_T have definite values Q, R, S, and T which exist independent of observation.

2. Alice performing her measurement does not affect the result of Bob's measurement.

The first assumption is sometimes known as realism, while the second is known as locality. Bell's inequality tells us that entanglement is a fundamentally new resource which may open up a new world of possibilities unimaginable with classical information. Teleportation, superdense coding, quantum communications may be only the tip of an iceberg.

II.D Quantum Teleportation

Suppose that Alice and Bob share an Einstein-Podolsky-Rosen (EPR) pair (i.e., an entangled two-qubit Bell state) at two distant locations. Alice would like to send Bob a qubit $|\Psi\rangle$. Neither Alice nor Bob knows the state of the qubit and Alice can only send a classical message. How can she achieve this task?

Alice interacts the qubit $|\Psi\rangle$ with her half of the EPR pair and then measures the resultant qubits in her possession. She obtains one of four possible classical results: 00, 01, 10, and 11. Once she sends the outcome to Bob, he recovers the qubit $|\Psi\rangle$ by doing one of the four operations on the qubit in his possession.

We can express the whole state as a tensor product of the unknown state $|\Psi\rangle = \alpha|0\rangle + \beta|1\rangle$ and the EPR pair $|\beta_{00}\rangle = (|00\rangle + |11\rangle)/\sqrt{2}$ that Alice and Bob use

$$|\Psi_0\rangle = \frac{1}{\sqrt{2}}[\alpha|0\rangle(|00\rangle + |11\rangle) + \beta|1\rangle(|00\rangle + |11\rangle)]. \tag{II.25}$$

Assume that the first two qubits belong to Alice and the last qubit belongs to Bob. Alice first acts on her qubits by `CNOT` gate, obtaining

$$|\Psi_1\rangle = \frac{1}{\sqrt{2}}[\alpha|0\rangle(|00\rangle + |11\rangle) + \beta|1\rangle(|10\rangle + |01\rangle)]. \tag{II.26}$$

Then she performs Hadamard operation on her first qubit, obtaining

$$|\Psi_2\rangle = \frac{1}{2}[\alpha(|0\rangle + |1\rangle)(|00\rangle + |11\rangle) + \beta(|0\rangle - |1\rangle)(|10\rangle + |01\rangle)]. \tag{II.27}$$

We can reexpress Eqn. (II.27) as

$$|\Psi_3\rangle = \frac{1}{2}[|00\rangle(\alpha|0\rangle+\beta|1\rangle)+|01\rangle(\alpha|1\rangle+\beta|0\rangle)+|10\rangle(\alpha|0\rangle-\beta|1\rangle)+|11\rangle(\alpha|1\rangle-\beta|0\rangle)]. \tag{II.28}$$

Remember that the first two qubits are Alice's and the third is Bob's. Therefore, given the result of Alice's measurements, Bob's qubit collapses into one of the following states:

$$00 \mapsto |\Psi_3(00)\rangle \equiv \alpha|0\rangle + \beta|1\rangle \tag{II.29}$$

$$01 \mapsto |\Psi_3(01)\rangle \equiv \alpha|1\rangle + \beta|0\rangle \tag{II.30}$$

$$10 \mapsto |\Psi_3(10)\rangle \equiv \alpha|0\rangle - \beta|1\rangle \tag{II.31}$$

$$11 \mapsto |\Psi_3(11)\rangle \equiv \alpha|1\rangle - \beta|0\rangle. \tag{II.32}$$

Then, in order for Bob to recover the state $|\Psi\rangle$ he performs the operation $Z^{M_1}X^{M_2}$ on his half of the EPR pair, where M_1 and M_2 are the classical bits that Alice obtains from her measurements and sends to Bob. For example, if Alice measures $M_1 = 1$ and $M_2 = 0$, then Bob has to apply Z gate to the qubit in his possession to recover the original unknown state $|\Psi\rangle = \alpha|0\rangle + \beta|1\rangle$.

Quantum teleportation can be used to build noise-resistant quantum logic gates and is intimately connected with quantum error-correcting codes.

II.E Quantum Simulations

A dynamical system can be simulated efficiently, if it can be described efficiently by some differential equations such as the electromagnetic vector wave equation,

$$\vec{\nabla} \cdot \vec{\nabla}\vec{E} = \epsilon_0\mu_0 \frac{\partial^2 \vec{E}}{\partial t^2}, \tag{II.33}$$

or the diffusion equation,

$$\vec{\nabla}^2\psi = \frac{1}{a^2}\frac{\partial\psi}{\partial t}, \tag{II.34}$$

to name a very few. The dynamical behaviour of many simple quantum systems, however, is described by Schrödinger's equation ($\hbar$ is absorbed into H),

$$i\frac{d}{dt}|\psi\rangle = H|\psi\rangle, \tag{II.35}$$

which in the position representation can be given as

$$i\frac{\partial}{\partial t}\psi(x) = \left[-\frac{1}{2m}\frac{\partial^2}{\partial x^2} + V(x)\right]\psi(x). \tag{II.36}$$

Eqn. (II.36) is similar to the diffusion Eqn. (II.34). The difficulty is not in simulating Schrödinger's equation. The key challenge in simulating quantum systems is the exponential number of differential equations, which must be solved, as the number of qubits increase. The simulation of n qubits involves 2^n equations. Therefore, classical simulation of quantum systems is not feasible for many physically interesting quantum systems, such as the Hubbard and Ising models, and many others.

In most physical systems we can write the Hamiltonian for a system of n particles as a summation over many local Hamiltonians which usually involve only nearest neighbor interactions:

$$H = \sum_{k=1}^{L} H_k. \tag{II.37}$$

Most interactions decay rapidly with increasing distance or energy difference. Therefore, H_k acts on at most a constant c number of particles and $L = \text{poly}(n)$. It is in general difficult to compute the evolution operator e^{-iHt}, but we can approximate e^{-iH_kt} using efficient quantum circuits, since it only acts on a small subsystem. The problem, however, is that $[H_j, H_k] \neq 0$ for most interactions, and therefore $\mathrm{e}^{-iHt} \neq \prod_k \mathrm{e}^{-iH_kt}$.

Then, how can we simulate those quantum systems? We can approximate e^{-iHt} by using one of the following methods with Δt such that the error is acceptable:

$$e^{i(A+B)\Delta t} = e^{iA\Delta t}e^{iB\Delta t} + O(\Delta t^2), \tag{II.38}$$

$$e^{i(A+B)\Delta t} = e^{iA\Delta t/2}e^{iB\Delta t}e^{iA\Delta t/2} + O(\Delta t^3), \tag{II.39}$$

or the Baker-Campbell-Hausdorff formula,

$$e^{(A+B)\Delta t} = e^{A\Delta t}e^{B\Delta t}e^{-\frac{1}{2}[A,B]\Delta t^2} + O(\Delta t^3). \tag{II.40}$$

Suppose that we have a Hamiltonian of the form in Eqn. (II.37) acting on an N-dimensional system and our initial state at time $t = 0$ is $|\psi_0\rangle$. We would like to simulate the system to find the state $|\psi_{t_f}\rangle$ at time t_f with a positive accuracy δ, such that

$$|\langle\tilde{\psi}(t_f)|e^{-iHt_f}|\psi_0\rangle|^2 \geq 1 - \delta. \tag{II.41}$$

A simple algorithm that is given below for this simulation requires $O[\text{poly}(1/\delta)]$ steps:

1. $|\tilde{\psi}_0\rangle$; $j = 0$. (initialization)
2. $\rightarrow |\tilde{\psi}_{j+1}\rangle = U_{\Delta t}|\tilde{\psi}_j\rangle$ (iterative update)
3. $\rightarrow j = j + 1$; goto 2 until $j\Delta t \geq t_f$ (loop)
4. $\rightarrow |\tilde{\psi}(t_f)\rangle = |\tilde{\psi}_j\rangle$. (final result)

$U_{\Delta t}$ in the above algorithm is the quantum circuit for each iterative step that can be approximated as one of those given in Eqns. (II.38)-(II.40).

Although we described above the quantum simulation procedure for Hamiltonians that are sums of local interactions, efficient quantum simulations are possible even for Hamiltonians that act on all or nearly all parts of the total system. One such form of a Hamiltonian is

$$H = \bigotimes_{k=1}^{n} \sigma_{c(k)}^{k}, \tag{II.42}$$

where $\sigma_{c(k)}^{k}$ is a Pauli matrix [or identity for $c(k) = 0$] acting on the kth qubit, $c(k) \in \{0, 1, 2, 3\}$ specifying one of $\{I, X, Y, Z\}$.

Chapter III

Inspiring Technologies

In this chapter we review the recent achievements and challenges in cavity QED and linear optical approaches to quantum information processing and quantum computing based on "a quantum information science and technology roadmap" developed in 2004 sponsored by ARDA and other government sponsors. Accomplishments in these areas are critical to photonic crystal based fault-tolerant and scalable architectures for quantum computers and networks. For more information about the recent reports and references please consult Refs. [6-7].

III.A Cavity Quantum Electrodynamics

Atomic, photonic, and motional qubits form the three major qubits for cavity quantum electrodynamics (QED). Photonic qubits in cavity QED manifest themselves as excitations of a cavity or flying qubits that escape from it. In the context of quantum information processing cavity QED refers to coherent interaction of light with material, such as the interaction of single photons and moving or trapped atoms and as well as semiconductor quantum dots in high finesse cavities. Cavity QED also offers nonlinear photon-photon interaction in a cavity. To achieve coherent dynamics between a single photon and an atom, the combined system should operate in the strong coupling regime; that is, the spontaneous

emission rate of the atom and the decay rate of the cavity must be smaller than the atom-photon interaction to start the Rabi oscillations. Strong coupling can be achieved in a high-Q cavity with low mode volume. Some experimental groups have accomplished this challenging task over the last two decades.

Using highly excited energy states of Rydberg atoms the strong coupling regime is achieved experimentally in microwave cavities. These experiments demonstrate some of the cleanest entanglements. The strong coupling limit is also achieved experimentally using neutral atoms in optical cavities.

Single-qubit rotations in cavity QED can be achieved with high fidelity. Several photon-photon and atom-atom gates have been proposed. Atom-atom gate experiments have been performed in microwave regime. Over 90% success rate is within reach in current experiments. In cavity QED many atom-atom and photon-photon gates can be adapted to atom-photon entanglements. Using this idea many two-qubit quantum logic operations, atom-atom, atom-photon, and photon-photon entanglements are proposed and some proof-of-principle experiments have been performed at various labs. These achievements suggest that scalable cavity QED architectures may be possible. Cavity QED systems amount to distributed computing where individual nodes are interconnected by optical fiber or waveguide based quantum communication channels.

More uniquely, cavity QED approach is also studied to build single or multiple photon sources as well as to implement simple quantum networks. Cavity QED systems are especially interesting for quantum information processing purposes to intra-convert atomic and photonic qubits. For a networkable quantum computer the ability to intraconvert stationary and flying qubits and transmission of the latter faithfully between the specified nodes through fibers or other means are needed. There has not been sufficient proof of principle for networkability of cavity QED systems either, despite the potentially viable solutions that have been proposed. Mapping atomic qubits to flying photonic qubits is one of the strongest potentials of cavity QED.

Qubit specific measurement capability of cavity QED technique has also achieved sufficient proof of principle. Individual neutral atoms have been detected in a state sensitive manner. Additionally, cavity QED provides excellent single atom detection.

Long-lived hyperfine states of neutral atoms are available for storing quantum information. Cavity QED quantum computing has good ability to initialize the hyperfine state of qubits by optical pumping techniques in atomic physics. Despite promising achivements in state initialization and measurement, however, there has not been sufficient proof of principle in scalability of the system with well-characterized qubits, decoherence times, and universal set of quantum gates.

Creation of an arbitrary qubit, two-qubit operations, and generation and characterization of Bell and three-qubit GHZ states require further experimental work. There have been some preliminary experimental demonstrations for preparation and readout of qubits, implementation of coherent two-qubit quantum logic operations, much longer qubit decoherence time than two-qubit gate operation times, production of GHZ entangled states in microwave cavity QED systems, quantum process and state tomography for two qubits, two-qubit decoherence free subspace, and two-qubit quantum algorithms.

Major types of cavity QED systems include Rydberg atoms in microwave cavities, neutral atoms in optical cavities, trapped ion cavity QED, semiconductor quantum dot systems, solid state ion vacancy systems, superconducting junctions and cavity systems, and neutral atom ensemble based cavity QED systems.

In cavity QED decoherence time is, in general, much longer than the gate operation time. In contrast to trapped ions, atomic coherence for neutral atoms is somewhat less due to the Stark shifts induced by trapping potentials. Qubit coherence during quantum operations, on the other hand, depends on the strong coupling regime, that is, the geometry of the cavity and internal states of the atoms. There have been significant experimental demonstrations of single-qubit rotations especially Rabi flop and high-Q transition of a qubit. Qubit coherence on the

order of seconds to minutes has been realized. Single-qubit gates are not limited by qubit decoherence. They are degraded by external noise in the environment or driving field and differential Stark shift due to trapping potentials.

The major obstacle for the Rydberg atoms in microwave cavities is that these systems are not scalable, because stochastic atomic beams are used and they have to intersect with the cavities. Moreover, microwave photons leaking from the cavity cannot be coupled to fiber and detected efficiently, although this can be succesfully achieved in the optical regime.

In contrast to Rydberg atoms in microwave cavities, the main obstacle for neutral atoms in optical cavities is to incorporate scalable trapping geometries with magnetic and optical potentials, which are incompatible with low mode volume of the cavities, while preserving the strong coupling regime and compact size. Trapping and delivering single atoms in one-dimensional arrays has been established using atom conveyors. There is, however, trade-off between small mode volume for strong coupling and incorporating an array of atoms inside the cavity. Furthermore, long-range dipole-dipole interactions cannot be implemented in a controlled manner.

There have been no experimental demonstrations on three and more qubit operations (other than GHZ states) such as repetitive error correction and fault-tolerant quantum control of a single logical qubit.

To sum up, special strengths of cavity QED are its well-known theory and abilities for interconversion between stationary and flying qubits, deterministic single and entangled photon sources, and distributed quantum computing. There are also some unknowns and weaknesses. The role of atomic motion degrees of freedom during gate operations is not well understood. New techniques to localize and control Rydberg atoms under strong coupling need to be developed. Other emerging cavity technologies such as photonic crystal and whispering gallery mode may lead to stronger coupling regime and hence better performance.

The next important steps in the field may be demonstrations of determin-

istic high quality single photon and entangled photon pair sources, deterministic entanglement between atoms and photons in optical cavity, distributed entanglement over different cavity QED systems, and system scalability.

III.B Linear Optics

Optical manipulations of qubits led to many successful experimental realizations in quantum information technology which include quantum cryptography, first realization of multiparticle entanglement, quantum state and process tomography, teleportation, decoherence free subspaces, and some simple quantum algorithms.

Photon-photon coupling in existing materials is extremely small. However, recent advances in slow light and stopped light may overcome this difficulty. It has also been shown in the Knill, Laflamme, Milburn (KLM) scheme that deterministic single photon sources, and highly efficient single photon detectors are sufficient to realize quantum computing using only linear optical components. Some authors suggested simplifications and modifications to the original scheme. The main challenge is the requirement to produce entangled ancilla states, because more than 99% detector efficiency is needed. Therefore, generation of entangled states can play a key role in optical quantum computing. In addition to KLM scheme, other schemes without single photon sources are also proposed.

There has been a sufficient proof of principle in optical quantum computing for decoherence times much longer than gate operation times. Single qubit operations typically take less than a picosecond. Two-qubit gate times depend on the teleportation protocol. Gates on demand have not yet been demonstrated. Typically these gates would operate three order of magnitude slower (i.e., nanoseconds) than single qubit ones. Although the coupling of optical qubits to the thermal environment is low, photons are lost in the system. The main sources of decoherence or error are interferometric stability, both spatial and temporal mode matching,

photon loss, and detector efficiency. If gates are realized in the form of optical couplers or planar integrated circuits, mode matching and interferometric stability would be less problematic, but then the coupling of qubits to these devices must be optimized.

In optical quantum computing systems, potentially viable approaches have been proposed for scalability with well-characterized qubits, initialization of the qubits, universal set of quantum gates, and qubit-specific measurements.

Qubits in the KLM scheme are represented by the occupation of one of the modes of a pair of optical modes (such as polarization modes), which is called dual-rail representation. Some other schemes use a single mode where qubits are encoded by coherent amplitudes of the same optical mode.

Initialization of qubits in optical quantum computing requires fast, reliable, and on-demand (periodic) single photon sources. They must generate one and only one photon and demonstrate interference between two single photon pulses using Hong, Ou, Mandel (HOM) interferometer.

Single qubit operations are achieved by linear optical elements such as beam splitters, phase shifters, and polarization rotators. Teleportation gates, however, require very fast electro-optic control or photon storage. This is also relevant to conventional electro-optical switching technologies. Although no prior entanglement on demand has been yet demonstrated, it is useful for error-correction codes and to reduce the gate complexity substantialy. In the long term, integrated optical devices and elementary interferometer modules need to be developed to replace current bulky devices. For example, planar optical waveguides and photonic bandgap based devices integrated with single photon sources can be used to build more compact and robust quantum circuits.

Regarding the networkability of linear optical quantum computing and communications systems, the ability to transmit flying qubits between specified locations has achieved sufficient proof of principle. Good mode-matching is required to couple free-space or optical fiber photons to quantum circuits. Photonic

crystals can also be used as quantum interconnects to faithfully transmit photonic qubits inside the chip. However, interconverting stationary and flying qubits have not been sufficiently demonstrated.

There have been sufficient experimental demonstrations in single-qubit operations, quantum state tomography for one and two qubits and process tomography for single qubit, two-qubit decoherence free subspace, and two-qubit quantum algorithms such as Deutsch-Josza, Grover, and quantum Baker's map algorithms. Although they are not scalable, these systems allow to incorporate and test various error avoidance and correction techniques. Further improvement requires good single photon detectors and sources.

Regarding single-qubit operations, Rabi flops of a qubit and decoherence times much longer than Rabi oscillation have been realized experimentally. Single photon gates require only a beam splitter with variable amplitude reflectivity. Huge numbers of logic operations can be performed before dephasing or photon loss becomes a problem. In dual rail polarization encoding, single qubit rotation can be easily implemented. Similarly, polarization qubits can be transformed with essentially no decoherence. Basic photon storage has also been demonstrated in linear optical approaches to quantum computing.

Creation of a qubit, implementation of coherent two-qubit logic operations, production and characterization of Bell states, decoherence times much longer than two-qubit gate times, production of three-qubit GHZ state, and transfer of quantum information (such as teleportation, entanglement swapping, multiple swap operations) do not have sufficient experimental demonstrations.

Preparation and readout of single photon states using spontaneous parametric down conversion and post-selection have been demonstrated. Precision state tomography has been realized. The first electrically driven single photon sources based on Coulomb blockade in a p-n junction have been demonstrated. Promising results using quantum dots have been reported. Independently generated single photons from a quantum dot were demonstrated to have HOM interference. How-

ever, the probability of obtaining more than a single photon in quantum dots is still high. Single nitrogen vacancies in diamond manifest photon antibunching, but collection efficiency and bandwidth make it not appealing for linear optical quantum computing. Some cavity QED techniques have also been reported using single atoms in a high-finesse cavity, but the outcoupling efficiency in these systems is very low. Single photon detectors with efficiencies of 88% have been demonstrated. They are capable of distinguishing incident photon number. Superconducting detectors are excellent to resolve photon number, but the detection efficiency is very low. Suggestions for single photon detectors with 99% detection efficiency and photon number resolving capability have been reported based on coupling to atomic systems. Similar schemes for photonic quantum memories have been proposed.

A nonuniversal two-qubit gate based on spontaneous parametric down conversion and post-selection has been partially achieved. Independently produced downconverted photons were demonstrated to violate Bell inequality. Production and generation of Bell states and GHZ states using spontaneous parametric down-conversion and post-selection have been demonstrated, but the major challenge is to make these process on demand without post-selection. This requires single-photon sources or entanglement-on-demand sources.

No experimental demonstrations of maximally entangled states, quantum state and process tomography, decoherence free subspaces, quantum error-correcting codes, and quantum logic operations with fault-tolerant precision with three or more qubits have been performed.

It is difficult to mode-match and stabilize many multiply-nested interferometers. Linear optical quantum computing is directly compatible with quantum communications and a large scale integration may be available using planar integrated circuits or photonic bandgap technology, if it is shown to be more robust and stable. This will require a considerable amount of classical electromagnetic modeling. Because the information is encoded in optical modes, there may be no

need to convert the qubits to connect the all-optical quantum circuits to communication systems. If the quantum communication will rely on telecommunications wavelength 1.55μm, then photonic qubits will either need to be at the same wavelength or will need to be converted to 1.55μm to avoid propagation loss. Whether or not the quantum processor is realized optically, optical qubits seem to be the most attractive qubits for interconnecting different parts of the quantum processor as well as for distributed quantum computing to connect distant nodes. High efficiency wavelength converters are needed to match the optimal processing wavelength with the optimal transmission wavelength. We need to develop the design rules for scaling-up integrated devices.

Chapter IV

Gate-Level Design: Quantum Entanglement and Logic Operations

The superiority of quantum computing over classical computation for problems with solutions based on the quantum Fourier transform, as well as search and (quantum) simulation problems has attracted increasing attention over the last decade. Despite promising developments in theory, however, progress in physical realization of quantum circuits, algorithms, and communication systems to date has been extremely challenging. Major model physical systems include photons and nonlinear optical media, cavity QED devices, ion traps, and nuclear magnetic resonance (NMR) with molecules, quantum dots, superconducting gates, and spins in semiconductors [2].

Quantum logic gates and quantum entanglement constitute two building blocks, among others, of more sophisticated quantum circuits and communication protocols. The latter also allows us to test basic postulates of quantum mechanics.

In this chapter we propose an alternative method for creating entanglement and implementing certain quantum logic gates based on single mode PC microcavities. Our scheme requires high-Q PC microcavities with Q-factor of around

10^8, and where atoms can freely propagate through the connected void regions. We consider 3D PCs for our purposes, since they are more attractive, compared to 2D PC slabs, for the realization of such high-Q microcavities. Although the fabrication of these high-Q 3D PC microcavities is currently challenging, especially in the optical frequencies, mainly due to the reduced size of the crystals at those wavelengths; in the microwave or millimeter-wave regime, where our proposed PC cavity operates ($\sim$ 50GHz), the fabrication process is relatively easier thanks to the rather macroscopic nature of the crystals at that scale. Thus, simple machining or rapid prototyping methods can be exploited to build them [8]. It is for this reason that the initial experiments on PCs were performed in the microwave region. Subsequently, much of the research concentrated on the infrared or the optical regime of the spectrum because of numerous applications which demand telecommunications wavelengths and/or miniaturization. In the less studied but also less technically challenging microwave region the Q-factor is limited by the intrinsic loss of the material [9, 10]. Using an appropriate low-loss dielectric such as sapphire, for example, it has been predicted by Yablonovitch [9] that a Q-factor of more than 10^9 should indeed experimentally be achievable. M. Qi, *et al.* [11] have furthermore predicted that using interference, imprint or X-ray lithography combined with scanning-electron-beam-lithography, their layer-by-layer approach could allow the manufacturing of large area (several square centimeters) PCs which are low-cost, optical or even visible spectrum versions of 3D PC cavities similar to ours.

IV.A Theory of Photonic Crystal Gate Interactions

We first explore the possibility of mutually entangling two Rb atoms by exploiting their interaction, mediated by a single defect mode confined to a three-dimensional PC cavity. We then describe various logic gates that can be

implemented using the same interaction. We achieve this in three steps: analysis of a single mode cavity (i) in a generic 3D PC, (ii) in a specific 2D PC and (iii) ultimately in a 3D version of the 2D PC of (ii). We assume that the defect frequency is resonant with the Rb atoms. Because the atoms are moving, the time-dependent Hamiltonian (Jaynes-Cummings Model) for this interaction in the dipole and rotating wave approximations is

$$H(t) = \frac{\hbar\varpi}{2}\sum_j \sigma_z^j + \hbar\varpi\alpha^\dagger\alpha + \hbar\sum_j [G_j(t)\sigma_+^j\alpha + h.c.] \tag{IV.1}$$

where the summation is over two atoms, A and B, ω is the resonant frequency, σ_z is the z-component of the Pauli spin operator and $\sigma_\pm$ are atomic raising and lowering operators. α and $\alpha^\dagger$ are photon destruction and construction operators, respectively. The time-dependent coupling parameters can be expressed as [12]

$$G_j(t) = \Omega_0 f_j(t)\cos(\zeta_j) \tag{IV.2}$$

where Ω_0 is the peak atomic Rabi frequency over the defect mode and $f_j(t)$ is the spatial profile of the defect state observed by the atom j at time t. ζ_j is the angle between the atomic dipole moment vector, $\mu_{\mathbf{eg}}^j$, for atom j and the mode polarization at the atom location. For the rest of the paper $\cos\zeta_A = 1$, and $p = \cos\zeta_B$ will be a parameter that we adjust to effect desired interactions between atoms A and B.

We ignore the resonant dipole-dipole interaction (RDDI), because the atoms have their transition frequencies close to the center of a wide photonic band gap (PBG) and the distance between them is always sufficiently large that RDDI effect is not significant [13, 14].

Initially we prepare one of the atoms, A, in the excited state and the cavity is left in its vacuum state, so

$$|\Psi(0)\rangle = |100\rangle, \tag{IV.3}$$

where the tensor factors describe the states of atom A, atom B, and the cavity, successively.

The PC should be designed to allow the atoms to go through the defect. This can be achieved by injecting atoms through the void regions of a PC with a defect state of acceptor type. Since the spontaneous emission of a photon from the atoms is suppressed in the periodic region of the crystal, no significant interaction occurs outside the cavity. When the atoms enter the cavity, the interaction between the atoms is enhanced by the single mode cavity. This atom-photon-atom interaction allows us to design an entanglement process between atoms.

Given the initial state, Eq. (IV.3), the state of the system at time t should be in the form

$$|\Psi(t)\rangle = a(t)|100\rangle + b(t)|010\rangle + \gamma(t)|001\rangle \tag{IV.4}$$

to satisfy the probability and energy conservation. We will show analytically that the amplitudes at time t can be expressed in terms of the coupling parameters and the velocities of the atoms.

We can write the Schrödinger equation for the time-evolution operator in the form [1]

$$i\hbar\frac{\partial}{\partial t}U(t,t_0) = H(t)U(t,t_0). \tag{IV.5}$$

In the basis $\{|100\rangle, |010\rangle, |001\rangle\}$, the matrix elements of the Hamiltonian, Eq. (IV.1), in the rotating wave approximation, are

$$H_{11} = H_{12} = H_{21} = H_{22} = H_{33} = 0 \tag{IV.6}$$

$$H_{13} = H_{31} = \hbar G_A(t) \tag{IV.7}$$

$$H_{23} = H_{32} = \hbar G_B(t). \tag{IV.8}$$

The Hamiltonian operators $H(t)$ and $H(t')$ commute for $t' \neq t$, if $G_B(t)$ is a constant multiple p of $G_A(t)$. This condition can be satisfied easily by the appropriate orientation of atomic dielectric moment of the incoming atoms with respect to the electric field in Eq. (IV.2). Then the formal solution to Eq. (IV.5) becomes

$$U(t,t_0) = \exp[-\frac{i}{\hbar}\int_{t_0}^{t} \mathrm{d}\tau H(\tau)] = \exp(-\frac{i}{\hbar}I), \tag{IV.9}$$

where I is defined as the integral of the Hamiltonian operator. By expanding the exponential, Eq. (IV.9), we obtain

$$U(t,t_0) = 1 + (\frac{-i}{\hbar})I + \frac{1}{2!}(\frac{-i}{\hbar})^2 I^2 + \cdots + (\frac{1}{n!})(\frac{-i}{\hbar})^n I^n + \cdots \tag{IV.10}$$

Multiplying Eq. (IV.10) by the initial state $|100\rangle$ from the right and comparing with Eq. (IV.4) gives

$$a(t) = 1 + G_A^2 \sum_{n=1} (-1)^n \frac{1}{2n!} (G_A^2 + G_B^2)^{n-1} \tag{IV.11}$$

$$b(t) = G_A G_B \sum_{n=1} (-1)^n \frac{1}{2n!} (G_A^2 + G_B^2)^{n-1} \tag{IV.12}$$

$$\gamma(t) = iG_A \sum_{n=1} (-1)^n \frac{1}{(2n-1)!} (G_A^2 + G_B^2)^{n-1}, \tag{IV.13}$$

where we have defined

$$G_j = \int_{t_0}^{t} G_j(\tau) d\tau. \tag{IV.14}$$

Recognizing the Taylor series for sine and cosine allows us to rewrite equations (IV.11)–(IV.13) as

$$a(t) = 1 + \frac{G_A^2}{G_A^2 + G_B^2} [\cos(G_A^2 + G_B^2)^{1/2} - 1] \tag{IV.15}$$

$$b(t) = \frac{G_A G_B}{G_A^2 + G_B^2} [\cos(G_A^2 + G_B^2)^{1/2} - 1] \tag{IV.16}$$

$$\gamma(t) = -i \frac{G_A}{(G_A^2 + G_B^2)^{1/2}} \sin(G_A^2 + G_B^2)^{1/2}. \tag{IV.17}$$

For a single initially excited atom, A, passing across the cavity we can set $G_B = 0$ in equations (IV.15)–(IV.17), which gives the same result as Eq. (IV.15) of Ref. [13]. The exact solution for the time-independent problem of N identical two level atoms with a resonant single mode quantized field given in Ref. [16] could be helpful to generalize our results to the N-atom case, see for example Ref. [13].

Absent a rigorous calculation of the defect mode in the three-dimensional PC, which we postpone until §IV.C, let us first assume a generic spatial profile for

the mode, which oscillates and decays exponentially. Thus, $f_j(t)$ in Eq. (IV.2) can be expressed as [12]

$$f_j(t) = \exp(-|V_j t - L|/R_{\rm def}) \cos[\frac{\pi}{l}(V_j t - L)], \qquad \text{(IV.18)}$$

where V_j, L, $R_{\rm def}$, and l are the velocity of atom j, the total path length of the atoms, the defect radius, and the lattice constant of the PC, respectively.

We choose the velocities of the atoms to be the same, $V_j = V$, with 150m/s $< V <$ 650m/s, a typical velocity range appropriate for both experiments and our calculations. Setting the atoms to have the same velocity has two immediate advantages: First, it makes the Hamiltonians at different times commute, since the coupling parameters of the atoms differ by only a constant factor [see Eq. (IV.2)], and thus greatly simplifies the analysis. Second, it synchronizes the atoms, providing cyclical readout that could also be synchronized with the cycle time of a quantum computer [17]. These features are not present in previous studies [12, 13, 18].

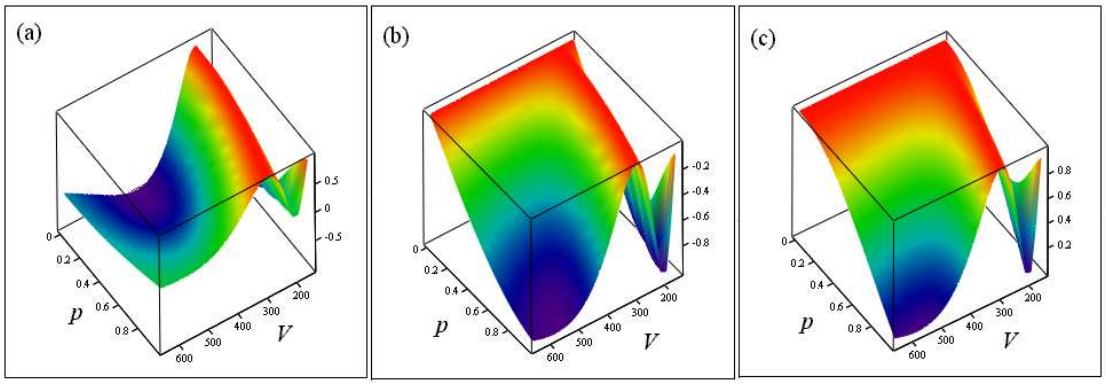

Figure IV.1: Probability amplitudes as a function of the velocity and p. Surfaces (a) $a(V,p)$ and (b) $b(V,p)$ (or $a(V,p)$) if the initial state is $|100\rangle$ (or $|010\rangle$). (c) Surface $b(V,p)$, if the system is initially prepared in the $|010\rangle$ state.

It was shown by E. Hagley, *et al.* [19] in 1997 that atomic velocity resolution could be as small as 0.4m/s in experiments, which means that our proposed entangler and logic gates are rather robust and insensitive to experimental velocity

fluctuations. In fact, with our design the velocity resolution of the atomic pairs can be further relaxed up to slightly more than $\pm$1m/s, increasing the efficiency of the system at the expense of less than 1% deviation in the output probability amplitudes.

Using equations (IV.15)–(IV.18) we can express the asymptotic probability amplitudes, $a(t)$ and $b(t)$, as functions of V and p. Fig. IV.1a illustrates $a(V,p)$, when the initial state is $|100\rangle$. The result for $b(V,p)$ (or $a(V,p)$), if the initial state is $|100\rangle$ (or $|010\rangle$), is displayed in Fig. IV.1b. Note that Fig. IV.1b illustrates two probability amplitudes simultaneously. This is a consequence of the symmetry in Eq. (IV.16). To compute these surfaces we used the asymptotic (constant) values of the G_j, which describe the accumulated atom-cavity coupling during the interaction time [(see Eq. (IV.14)]. Once this interaction ceases to occur as the atoms leave the cavity, those asymptotic values of the G_j are reached, and thus must be used in equations (IV.15)-(IV.17).

Fig. IV.2a illustrates a slice from the surface in Fig. IV.1a where the velocity of the atoms is $V = 433$m/s. Note that we obtain the maximally entangled state,

$$|\Psi_{10}\rangle \cong \frac{|10\rangle + |01\rangle}{\sqrt{2}}, \tag{IV.19}$$

up to an overall phase, -1, when the velocity of the atoms, $V = 433$m/s, and the initial state is $|100\rangle$. Similarly if we keep the velocities of the atoms the same but set the atom B to be excited initially (i.e., the initial state is $|010\rangle$), we obtain the slice in Fig. IV.2b and thus the maximally entangled state,

$$|\Psi_{01}\rangle \cong \frac{|10\rangle - |01\rangle}{\sqrt{2}}, \tag{IV.20}$$

up to the same overall phase factor as in Eq. (IV.19). [In equations (IV.19) and (IV.20), and in the following, we omit the cavity state in the kets, since it factors out and does not contribute to the logic operations with which we are concerned.]

Fig. IV.3 shows the coupling parameters calculated in the reference frame of the atoms as a function of time, $G_j(t)$, with the chosen values of Ω_0, L, $R_{\rm def}$,

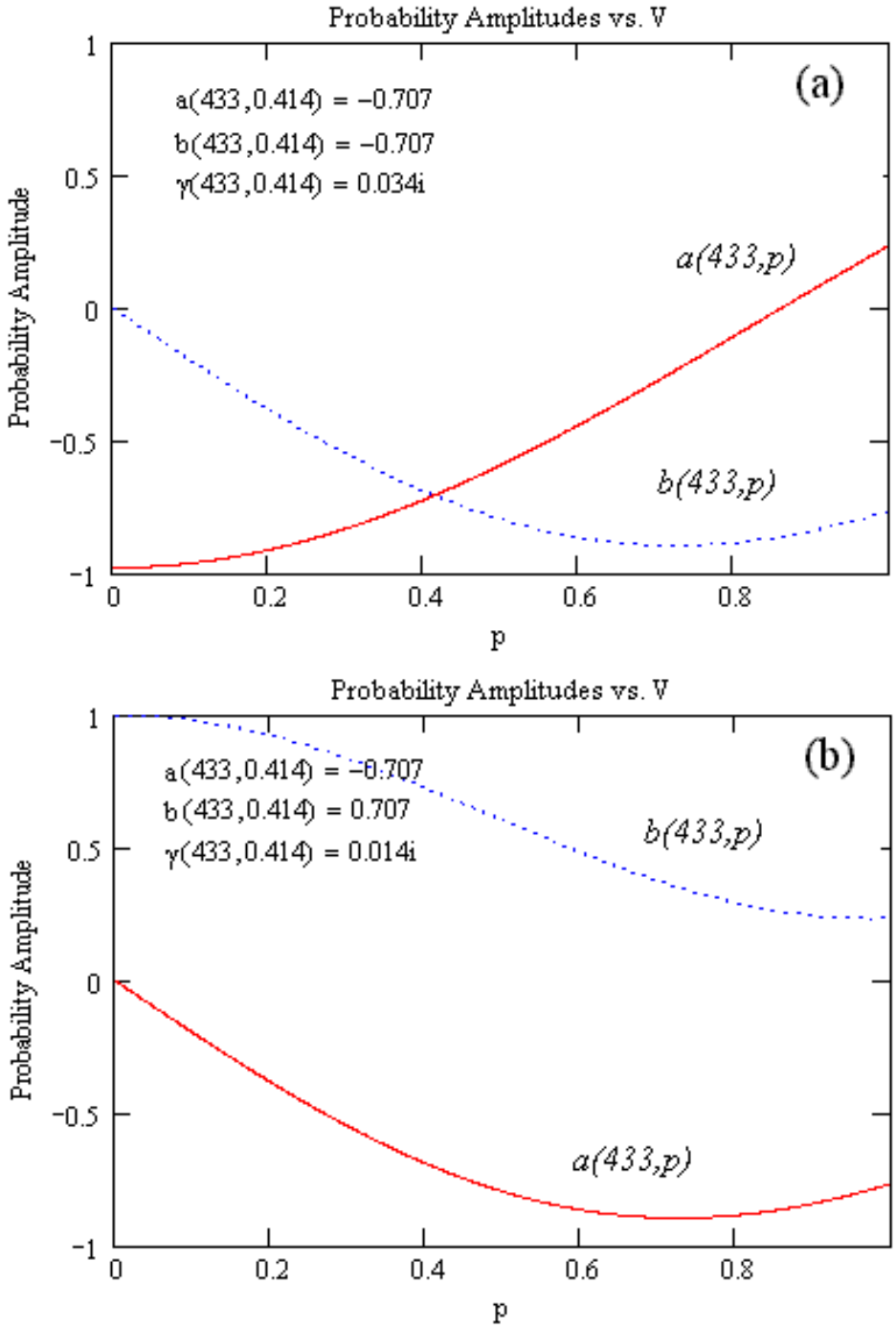

Figure IV.2: Slices from each surface in Fig. IV.1. (a) Probability amplitudes $a(V,p)$—red—and $b(V,p)$—dashed blue—with $V = 433$m/s. The entangled state, Eq. (IV.19), is obtained at $p = 0.414$. (b) Probability amplitudes $a(V,p)$—dashed blue—and $b(V,p)$—red—with the same velocity, $V = 433$m/s. The entangled state, Eq. (IV.20), is observed at the same value, $p = 0.414$.

and l. The solid red curve and blue dashed curve correspond to atoms A and B, respectively. The total interaction time is less than 20ns.

The probabilities $|a(t)|^2$, $|b(t)|^2$ and $|\gamma(t)|^2$ from equations (IV.15)–(IV.17) are graphed in Fig. IV.4. Fig. IV.4a shows the evolution of the probabilities when the initial state is $|100\rangle$. Note that the cavity is disentangled from the atoms and we end up with the final state, Eq. (IV.19). On the other hand, if the initial state is $|010\rangle$, the time evolution of the probabilities is illustrated in Fig. IV.4b. Note that the final state in this setting becomes Eq. (IV.20), since the cavity is again disentangled. From equations (IV.19) and (IV.20) it is clear that the quantum system we have described not only entangles the atoms but *also operates as a dual-rail Hadamard gate [2], up to an overall phase.*

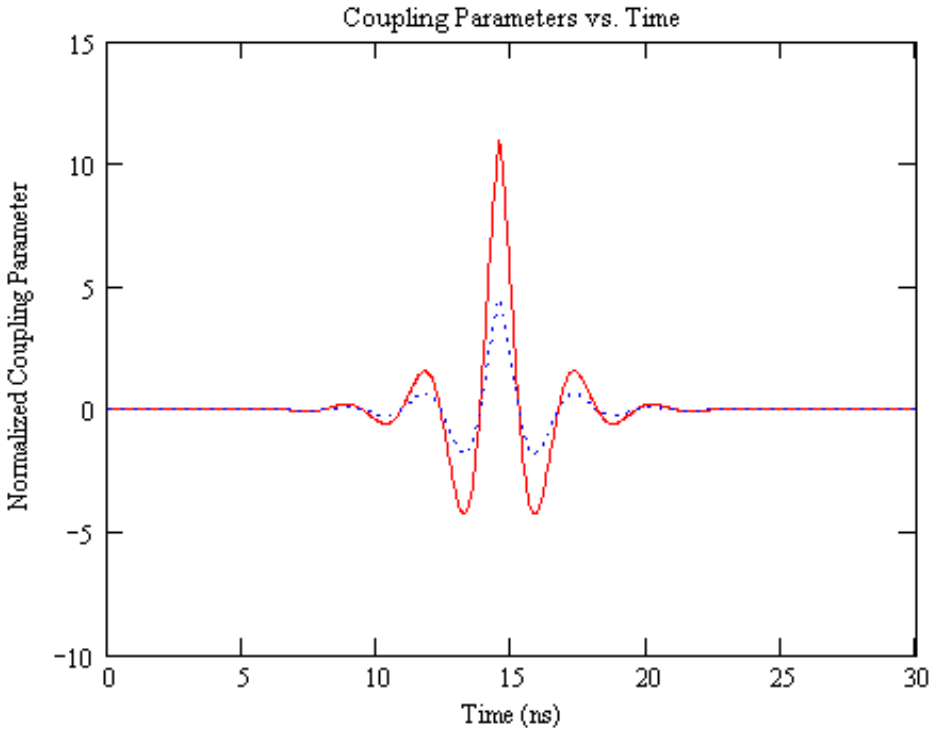

Figure IV.3: Coupling parameters in the reference frame of moving atoms with velocities $V = 433\text{m/s}$ at $p = 0.414$. $\Omega_0 = 11 \times 10^9\text{Hz}$, $\omega = 2.4 \times 10^{15}\text{Hz}$, $l = 1.6\frac{\pi c}{\omega}$, $L = 10l$, $R_{\text{def}} = l$ [12]. Atom A experiences the coupling parameter shown with the red solid curve and atom B the one shown with dashed blue.

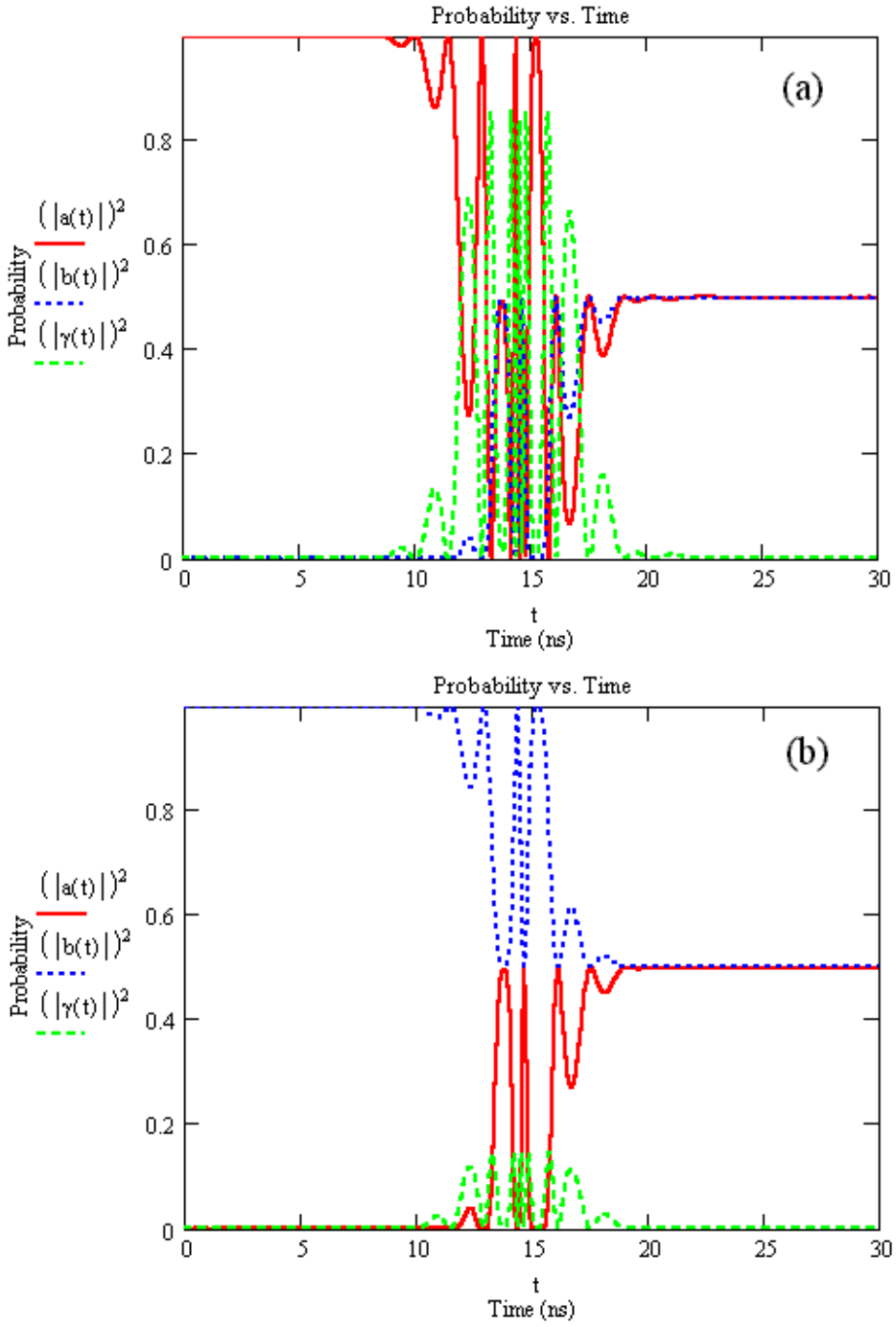

Figure IV.4: Time evolution of the probabilities showing the final entanglement when the initial state is (a) $|100\rangle$ and (b) $|010\rangle$.

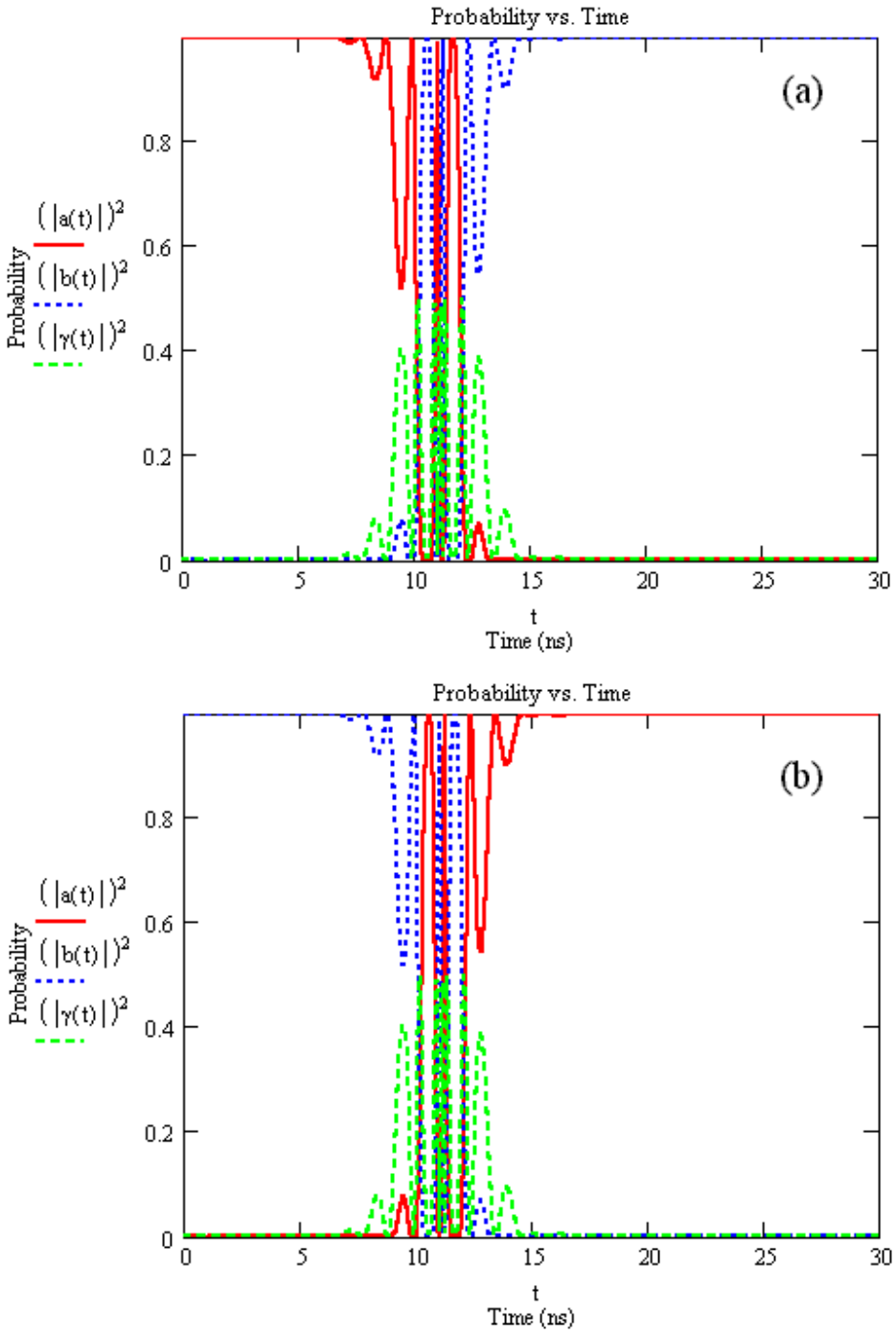

Figure IV.5: Time evolution of the probabilities that leads to a dual-rail NOT (Pauli σ_x) logic operation when the initial state is (a) $|100\rangle$ and (b) $|010\rangle$.

Using the same quantum system one can also design a dual-rail NOT gate under certain conditions. If we set $V_A = V_B = 565\text{m/s}$, for example, we obtain the following logical transformations, up to an unimportant global phase factor, which define a dual-rail NOT gate (see Fig. IV.5):

$$|10\rangle \mapsto |01\rangle \tag{IV.21}$$

$$|01\rangle \mapsto |10\rangle. \tag{IV.22}$$

Furthermore, using the Hamiltonian, Eq. (IV.1), it can be shown that a $|00\rangle$ initial state only gains a deterministic phase factor of -1 in the interaction picture. Once the conditions, equations (IV.21) and (IV.22), are satisfied, a $|11\rangle$ initial state is transformed into itself up to the same global phase as the states in equations (IV.21) and (IV.22). Thus, including these as possible initial states, our dual-rail NOT gate also operates as a SWAP gate up to the relative phase of the $|00\rangle$ state. Similar analysis shows that a dual-rail Z gate is also possible for certain parameter choices.

IV.B Two-dimensional Emulating Design

In the preceding analysis we have assumed the generic form, Eq. (IV.18), for the spatial profile of the defect mode in order to demonstrate that, in principle, PC microcavities can be used as entanglers, and more specifically, as certain logic gates. In the following we apply these ideas to two- and finally real three-dimensional photonic crystal microcavity designs, to show that implementations of these quantum devices are indeed possible in these photonic systems. As the authors of Ref. [13] observe, however, "a rigorous calculation of the electromagnetic field in the presence of a defect in a 3D photonic crystal can be a difficult task". In the following we address this task systematically.

First we consider a 2D photonic crystal design with a triangular lattice of dielectric rods with dielectric constant of 12 (i.e., silicon) in Fig. IV.6. The radius

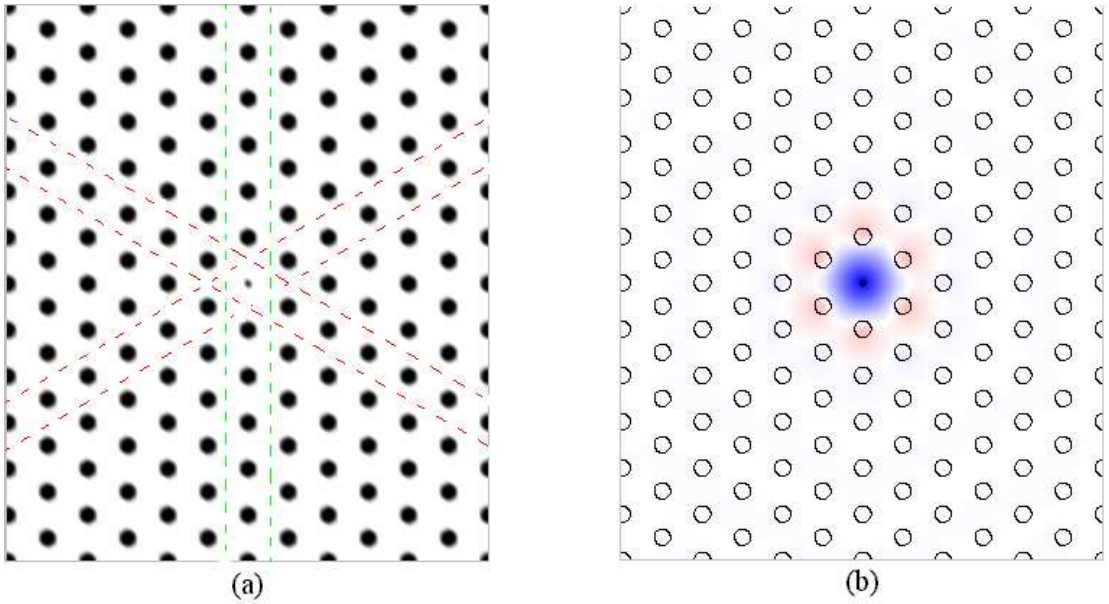

Figure IV.6: (a) A single-mode microcavity in a 2D photonic crystal with a triangular lattice (see the text for details). (b) The corresponding electric field spatial profile for the transverse-magnetic (TM) mode allowed in the cavity.

of the rods is $0.175l$, where l is the lattice constant. The symmetry is broken in the center by introducing a defect with reduced rod-radius of $0.071l$ to form the microcavity of our quantum system. We assume that the atoms A and B travel along the dashed green lines shown in Fig. IV.6a, although any two of the obvious paths shown by dashed lines (or any void regions with line of sight to the cavity) work as well.

We should note that the 2D cavity is only designed for preliminary purposes. Since it assumes infinite height, it cannot be intended for actual implementation of our entangler or logic operations. However, the real 3D PC, described in §IV.C, is sufficiently closely related to the 2D cavity designed in this section that the mode profiles along the 1D atomic trajectories in the 2D cavity overlap to a great extent with those of the 3D cavity. Regardless of the lack of vertical confinement in this preliminary 2D design, designing it first reduces the extensive computational resources needed in more sophisticated 3D logic designs.

In order to find the probability amplitudes for the atoms as a function of time while travelling through the crystal, we need to calculate the coupling parameters in Eq. (IV.14) and substitute them in equations (IV.15)–(IV.17). Once we obtain the probability amplitudes, we can demonstrate entanglement creation and design logic gates as before. We also note that the quality factor of the cavity should be high enough that the interaction time (i.e., the logic operation time) is much less than the photon lifetime in the cavity. Below we show that typical logic operations take 50μs for the Hadamard gate and 30μs for the NOT or the SWAP gate. Thus a quality factor of 10^8 should be sufficient for reliable gate operations in real 3D PC microcavities. Since our preliminary 2D PC cavity is not realistic, however, only an in-plane Q-factor of the same value is taken into consideration to match the mode profiles along the atomic trajectories in both 2D and 3D. To achieve this matching the Q-factor of the cavity could be increased exponentially with additional periods of rods [20] in Fig. IV.6a. We observe, however, that the spatial profile of the mode in Fig. IV.6b does not change significantly (and hence degrade the gate) after a certain number of periods. Thus, the exact number of periods required for a quality factor of 10^8 is not essential to demonstrate our main goal in this paper, namely that such logic operations and entanglement creation are indeed possible in these photonic crystal structures.

In our generic profile, Eq. (IV.18), the coupling parameter is assumed to be real. For generality, however, we must allow it to be a complex parameter. Thus, the interaction part of the Hamiltonian, Eq. (IV.1), for a single-atom cavity interaction can be written as [21-24]

$$H_I = \hbar|g(\mathbf{r})|(\alpha^\dagger\sigma_- + \alpha\sigma_+), \tag{IV.23}$$

by incorporating a complex coupling parameter $g(\mathbf{r})$ into Eq. (IV.1).

In a photonic crystal we can express the atom-field coupling parameter [21, 25] at the position of atom j, as

$$g(\mathbf{r}_j) = g_0\Psi(\mathbf{r}_j)\cos(\zeta_j) \tag{IV.24}$$

where g_0 and $\Psi(\mathbf{r}_j)$ are defined as:

$$g_0 \equiv \frac{\mu_{eg}}{\hbar}\left(\frac{\hbar\omega}{2\varepsilon_0\varepsilon_m V_{\text{mode}}}\right)^{1/2} \tag{IV.25}$$

$$\Psi(\mathbf{r}_j) \equiv E(\mathbf{r}_j)/|E(\mathbf{r}_m)|. \tag{IV.26}$$

$\mathbf{r}_m$ denotes the position in the dielectric where $\varepsilon(\mathbf{r})|E(\mathbf{r})|^2$ is maximum and ε_m is defined as the dielectric constant at that point. The cavity mode volume, V_{mode}, is given by

$$V_{\text{mode}} = \frac{\int\int\int \varepsilon(\mathbf{r})|E(\mathbf{r})|^2 \mathrm{d}\mathbf{r}}{\varepsilon_m |E(\mathbf{r}_m)|^2}. \tag{IV.27}$$

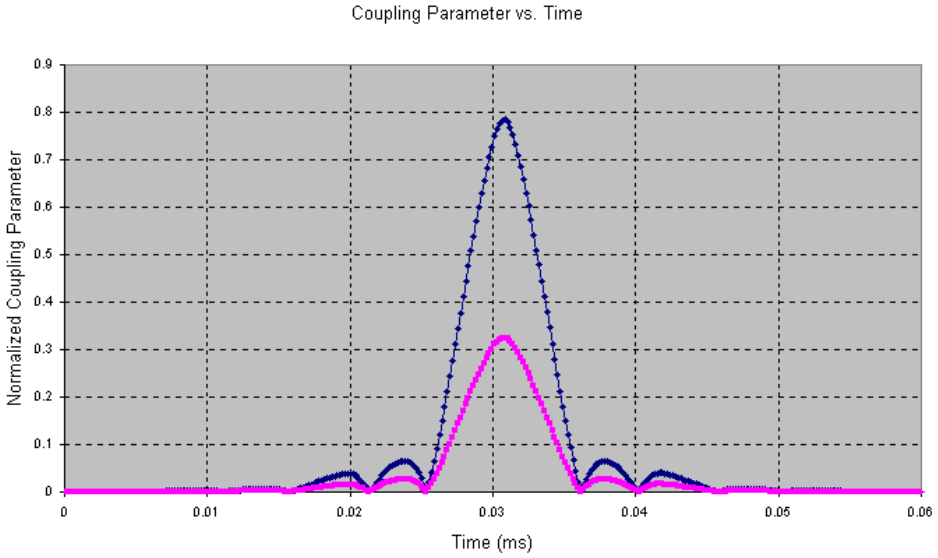

Figure IV.7: Normalized coupling parameters (i.e., divided by g_0) in the reference frame of moving atoms with velocities $V = 374$m/s at $p = 0.414$, where g_0 is found to be 2.765MHz. Blue and red curves correspond to normalized coupling strengths for atoms A and B, respectively.

Using the block iterative plane-wave expansion method [26] we found the normalized frequency of the cavity mode shown in Fig. IV.6b to be $0.3733c/l$. By setting $l = 2.202$mm, we tune the resonant wavelength to 5.9mm. At this wavelength, μ_{eg} for the Rb atom is 2×10^{-26}Cm [12]. Since we observe that the energy density is concentrated in the center of the cavity, ε_m in equations (IV.25)

and (IV.27) becomes 12. On the other hand, $\cos(\zeta_j)$ in Eq. (IV.24) can be safely assumed constant for each atom, because our cavity mode is a transverse-magnetic (TM) mode and its electric field polarization direction can always be assumed to have a constant angle with the atomic dipole moment vector, $\mu_{\mathbf{eg}}{}^j$. We can compute the coupling parameters as functions of time in the reference frame of the moving atoms, as shown in Fig. IV.7. The tails of the coupling parameter functions do not contribute significantly to the results due to exponential decay away from the cavity.

With these settings Fig. IV.8 demonstrates an entangler which operates as a dual-rail Hadamard gate. If the initial state is $|10\rangle$ (i.e., atom A is excited), we end up with state $|\Psi_{10}\rangle$ [see Eq. (IV.19) above and Fig. IV.8a]. If atom B is initially excited (i.e., the initial state is $|01\rangle$), however, we obtain the state $|\Psi_{01}\rangle$, up to an unimportant global phase factor of -1 [see Eq. (IV.20) above and Fig. IV.8b] as the output of the logic gate.

In order to get the system to act as a dual-rail NOT gate, we simply set the velocities of the atoms to be $V_A = V_B = 490\text{m/s}$. The evolution of the probability amplitudes for the atoms is shown in Fig. IV.9. When the excitation is initially at atom A (or at atom B), it is transferred to atom B (or atom A). Note that we also get an unimportant phase factor of -1 in the output. Furthermore, as explained above, the input states $|00\rangle$ (or $|11\rangle$) are not transformed into different states, and only $|00\rangle$ gains a different phase factor of $+1$. If this phase problem with the $|00\rangle$ state were solved, the system could also be exploited as a SWAP gate.

IV.C Three-dimensional Design

Although the implementation of logic gates in 2D photonic crystals looks promising, in reality we need 3D devices. The 2D analysis is useful, however, for reducing the substantial computation required for analyzing more realistic 3D

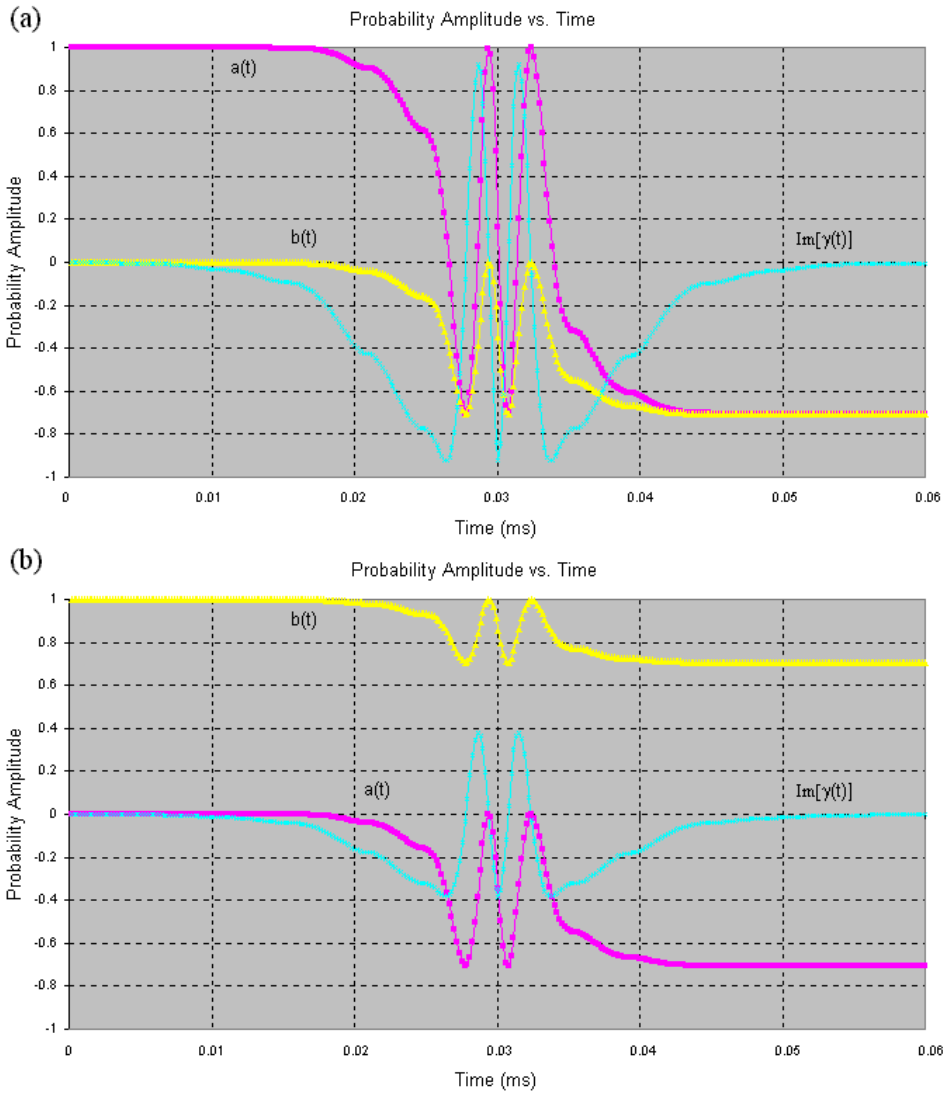

Figure IV.8: Probability amplitudes for entangled atoms created by a dual-rail Hadamard operation in the 2D photonic crystal (see Fig. IV.6) (a) when atom A is initially in the excited state and (b) when atom B is initially in the excited state. $a(t)$, $b(t)$ and $\gamma(t)$ are probability amplitudes for the states $|100\rangle$, $|010\rangle$ and $|001\rangle$, respectively.

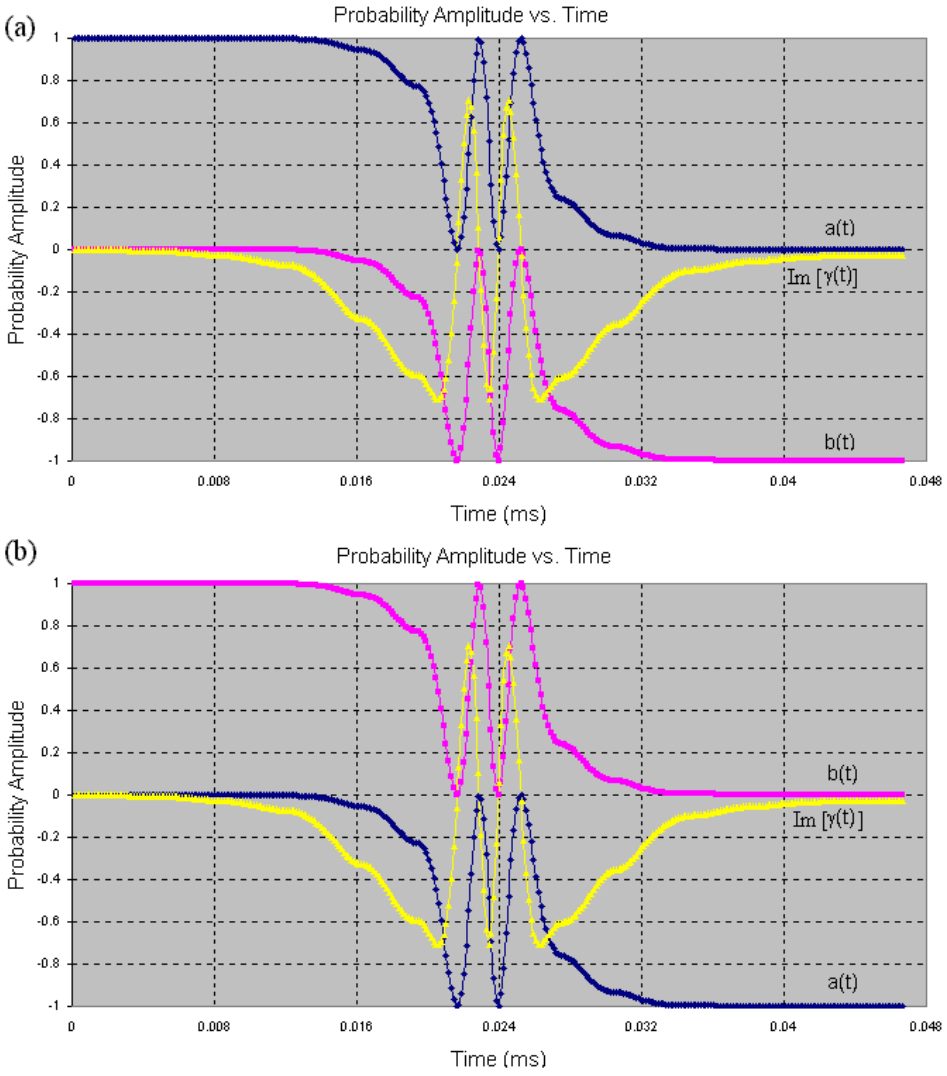

Figure IV.9: Probability amplitudes for atom A and B under the dual-rail NOT operation in the 2D photonic crystal when initially (a) atom A is excited only and (b) atom B is excited only.

structures, because there is great similarity between the modes allowed in these 2D crystals and in their carefully chosen 3D counterparts (see Fig. IV.10), which we describe next.

To engineer logic operations in 3D photonic crystals, we employ the structure [11, 27, 28] shown in Fig. IV.10a. The 3D photonic crystal we have chosen has various advantages over others [29-31]: emulation of 2D properties in 3D [11, 28], polarization of the modes, and simplified design and simulation. It consists of alternating layers of a triangular lattice of air holes and a triangular lattice of dielectric rods, where the centers of the holes are stacked along the [111] direction of the face-centered cubic (fcc) lattice. The parameters for the crystal are given in the caption of Fig. IV.10a. Using the block iterative plane-wave expansion method [26], we calculate that the structure exhibits a 3D band gap of over 20%, across the frequency range of $0.507c/l$–$0.623c/l$.

As in the 2D geometry, we introduce a defect by reducing the radius of a rod inside the crystal as shown in Fig. IV.10b. Using the supercell method we can compute that this cavity supports only a single mode with a frequency of $0.539c/l$. Setting $l = 3.18$mm tunes the cavity mode to the atomic transition wavelength of 5.9mm. Thus we can design a 3D single-mode cavity for our system to operate as the desired quantum logic gates.

The spatial profile for the electric field of the mode is shown in Figs. IV.10c and IV.10d. Note that it has a similar profile to its 2D counterpart in Fig. IV.6b, where the energy density is also maximized in the center of the cavity. It is this similarity which simplifies our design and analysis for the 3D case.

In our designs, although the maximum field intensity is concentrated in high-dielectric regions, the resultant atom-cavity interaction is sufficient to achieve our goals. Cavities maximizing the field intensity in low-index regions, where atoms can strongly interact with the mode, could lead to higher performance. However, from the design and implementation perspective we find the former more appropriate. Some of the drawbacks of the latter can be stated as follows: If we

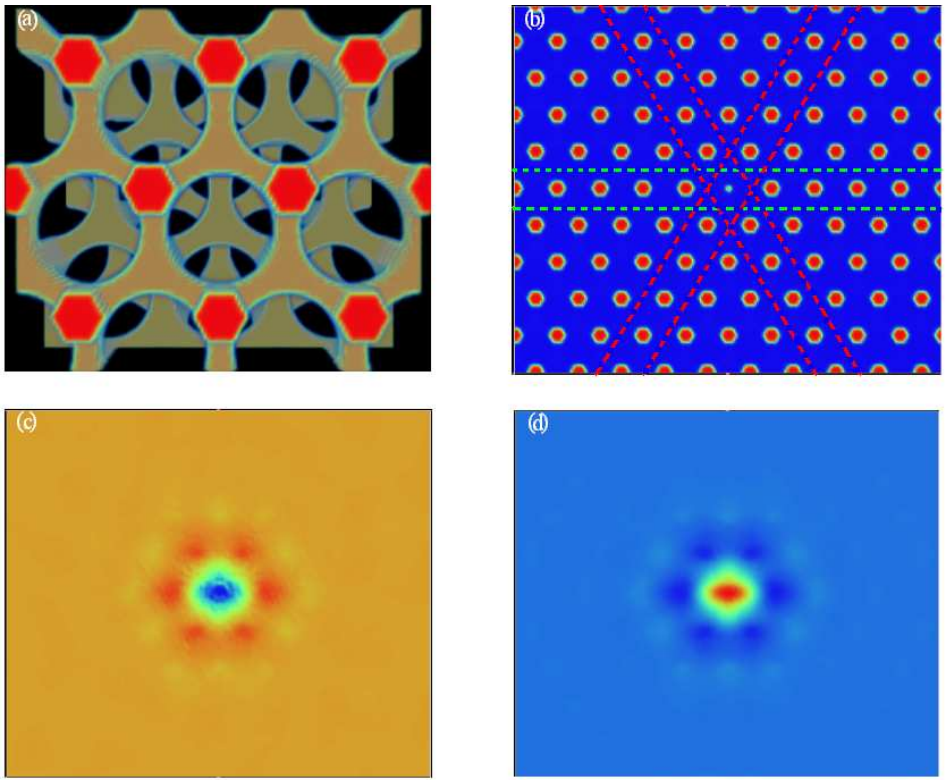

Figure IV.10: (a) Top view of the 3D photonic crystal with fcc lattice. It consists of alternating layers of a triangular lattice of air holes and a triangular lattice of dielectric rods (for details of the structure, see Refs. [11, 27, 28]). The nearest-neighbor spacing within either a hole or rod layer is $\frac{1}{\sqrt{2}}l$, where l is the fcc lattice constant. The hole and rod radii are $0.293l$ and $0.124l$, respectively. The thicknesses of a hole layer and a rod layer are taken to be $0.225l$ and $0.354l$, respectively. Silicon is assumed as the high-index material of dielectric constant 12. (b) Horizontal cross-section of the crystal. Dashed lines show the obvious paths atoms can travel. In our simulations we assumed the path shown by the dashed yellow line. A defect is introduced by reducing the radius of the middle rod down to $0.050l$ to hold a single mode in the cavity. The (c) real part and (d) imaginary part of the electric-field of the TM mode allowed in the cavity at a particular instant in time with the frequency of $0.539c/l$. The imaginary part is half a period later.

remove the dielectric completely in the center of the defect to maximize the field intensity in air, then the defect frequency would be close to the band edge, which would thus strengthen the otherwise negligible RDDI mechanism [13]. If we use a holey lattice, on the other hand, emulating the 2D PBG inside a 3D crystal and simultaneously allowing the free passage of atoms, without interfering with the dielectric backbone of the 3D crystal, would complicate the design considerably. Nevertheless, further optimization of the proposed structure could be possible.

We can quantify [28] the TM-polarization of the mode in a plane as:

$$P \equiv \frac{\int \mathrm{d}^2\mathbf{r}|E_z(\omega;\mathbf{r})|^2}{\int \mathrm{d}^2\mathbf{r}|\mathbf{E}(\omega;\mathbf{r})|^2}. \tag{IV.28}$$

We compute that P is almost 0.99 in the defect plane shown in Fig. IV.10b for the spatial profile exhibited in Figs. IV.10c and IV.10d. Thus it is safe to assume a TM polarized mode in the system Hamiltonian, because this doesn't affect the probability amplitudes significantly in the microwave regime, for the parameters we have chosen.

The coupling parameters as function of time in the reference frame of the atoms are shown in Fig. IV.11, where the velocities of the atoms are both set to $V = 353\mathrm{m/s}$, with $p = 0.414$.

In Fig. IV.12 we demonstrate the 3D version of our 2D dual-rail Hadamard gate, which also acts as an atomic entangler. Just as in the 2D case, if the initial excitation is on atom A, the resulting state is $|\Psi_{10}\rangle$ [see Eq. (IV.19) above] as shown in Fig. IV.12a, while if it is on atom B the output state is $|\Psi_{01}\rangle$ [see Eq. (IV.20) above] as displayed in Fig. IV.12b, up to an unimportant global phase of -1. The interaction between atom A and B is mediated by the photonic qubit when the parameters are set correctly.

We set the velocity of both atoms to $V_A = V_B = 459\mathrm{m/s}$ to obtain a dual-rail NOT gate in the 3D photonic crystal, up to an unimportant global phase factor, -1. The probability amplitude evolution of the atoms is displayed in Fig. IV.13.

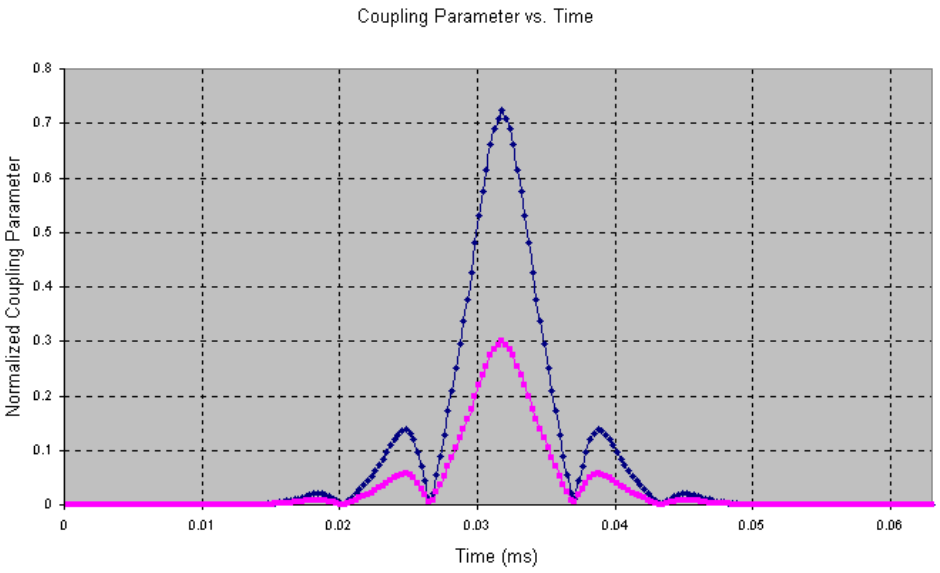

Figure IV.11: Coupling parameters in the reference frame of the moving atoms with both velocities $V = 353\text{m/s}$, and $p = 0.414$, where g_0 is found to be 2.899MHz. Blue and red curves correspond to normalized coupling strengths for atoms A and B, respectively.

The excitation of the excited atom is transferred to the ground state atom with the help of the photonic qubit allowed in the designed cavity. Note that because of the symmetry of the problem, the $b(t)$s in Figs. IV.5a, IV.9a and IV.13a are indeed approximately the same as the $a(t)$s of Figs. IV.5b, IV.9b and IV.13b, respectively. Furthermore, for the same reason as in the 2D case, analyzed in the previous section, our 3D dual-rail NOT gate also operates as a SWAP gate up to some deterministic phase. That is,

$$|00\rangle \mapsto -|00\rangle \tag{IV.29}$$

$$|01\rangle \mapsto |10\rangle \tag{IV.30}$$

$$|10\rangle \mapsto |01\rangle \tag{IV.31}$$

$$|11\rangle \mapsto |11\rangle. \tag{IV.32}$$

Note also that the values of the velocities of the atoms, and g_0, for the

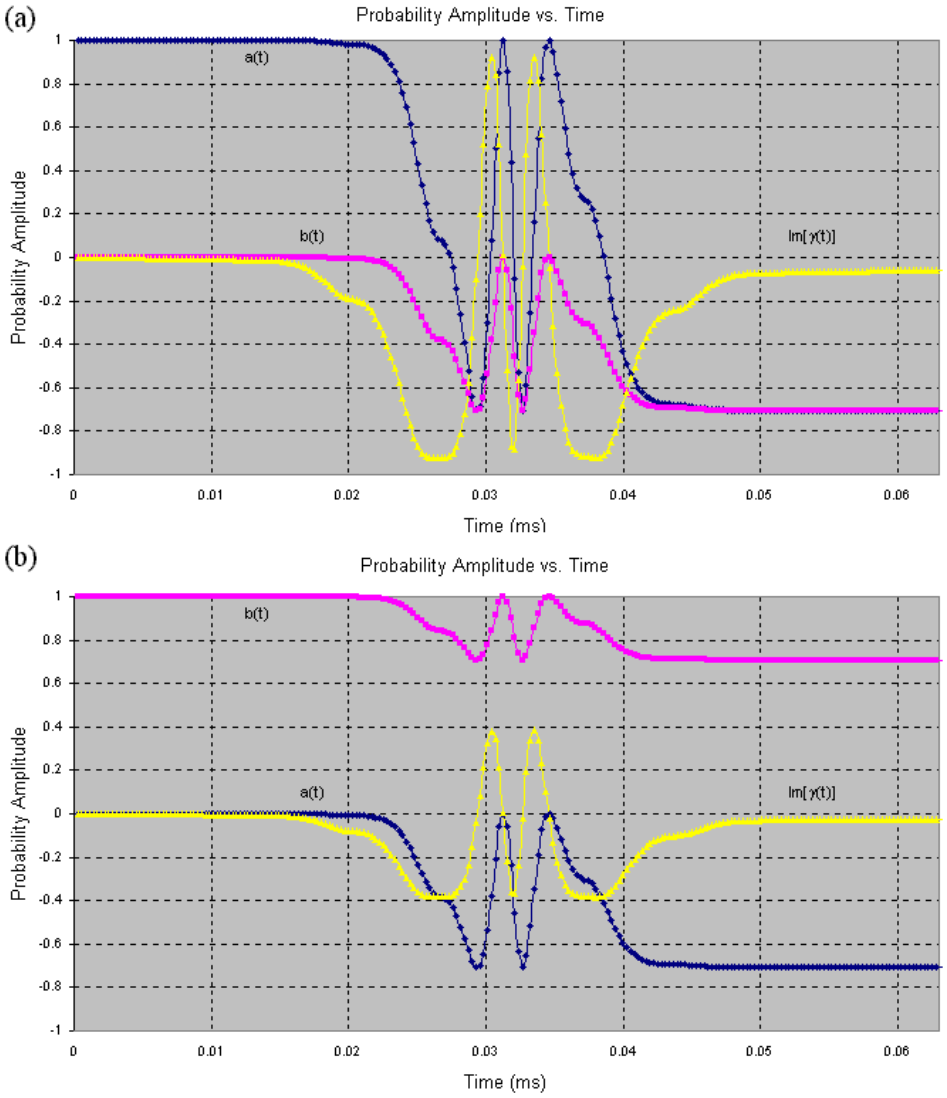

Figure IV.12: Probability amplitudes for the entangled atoms under dual-rail Hadamard operation in the 3D photonic crystal (see Fig. IV.10) when (a) atom A is initially in the excited state and (b) atom B is initially in the excited state. $a(t)$, $b(t)$ and $\gamma(t)$ are probability amplitudes for the states $|100\rangle$, $|010\rangle$ and $|001\rangle$, respectively.

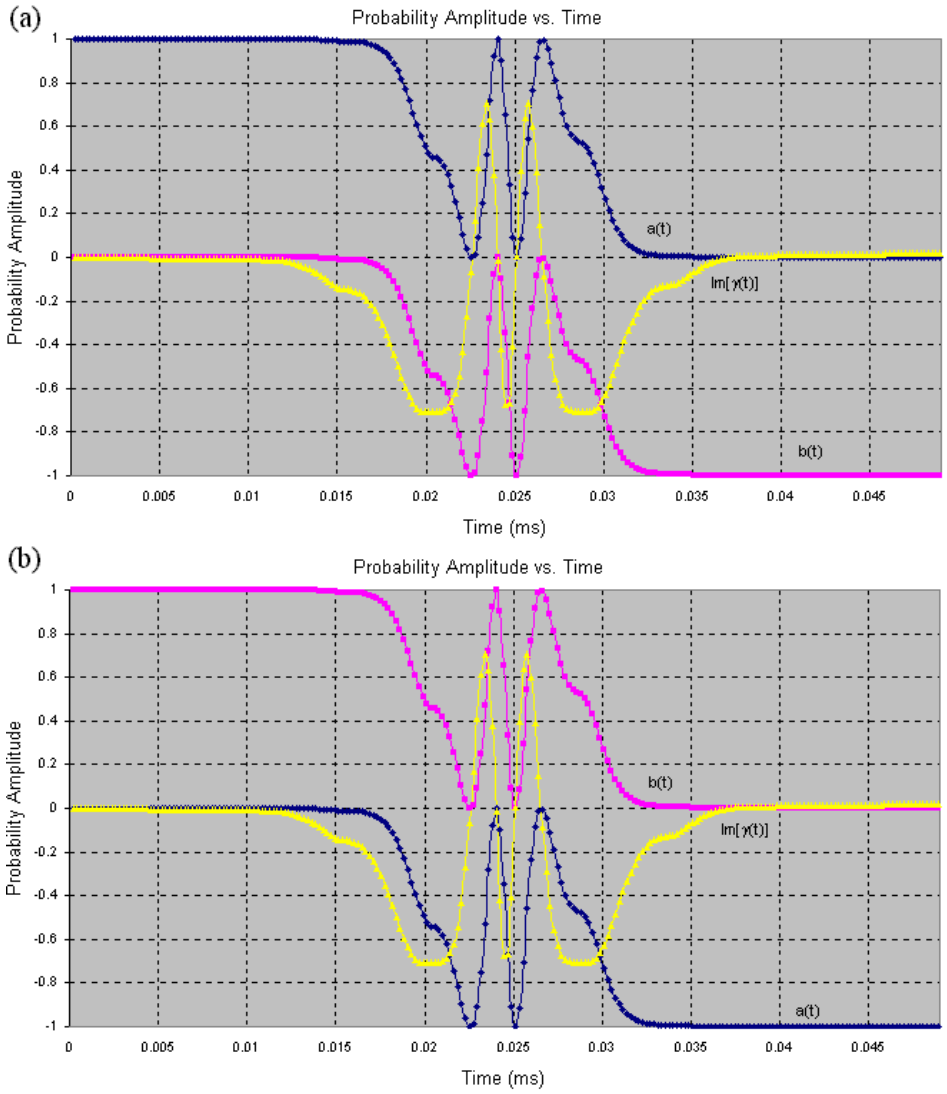

Figure IV.13: Probability amplitudes for atoms A and B under the dual-rail NOT operation in the 3D photonic crystal when initially (a) only atom A is excited and (b) only atom B is excited.

2D logic gates are within 10% of those in the 3D gates. This is a consequence of the fact that the localized modes allowed in 2D and 3D cavities have more than 90% overlap in their spatial profiles [28]. Thus our results are also consistent with Ref. [28] and justify first investigating the 2D case.

Portions of this chapter were presented in the paper: D. Ö. Güney and D. A. Meyer, "*Creation of entanglement and implementation of quantum logic gate operations using a three-dimensional photonic crystal single-mode cavity*", J. Opt. Soc. Am. B **24**, 283 (2007).

Chapter V

Circuit-Level Design: Teleportation and Readout

It has been shown theoretically by Bennett [32], et al. that quantum teleportation of an unknown state can be achieved using Bell states. Since then several theoretical and experimental schemes have been proposed, which include implementation in optical, NMR, and cavity QED systems [2, 33-35]. Inspired by the recent paper of S.-B. Zheng [33], in this letter we propose a photonic crystal (PC) based cavity QED implementation of the scheme described therein, as well as the integration of the device with an atomic readout circuit to detect the teleported state.

Underlying our interest in Zheng's proposal is the vision of more sophisticated large-scale photonic crystal integration for compact, robust, and scalable quantum computation technology. Zheng's teleportation protocol is only conditional (i.e., the success of the protocol is conditioned on a specific measurement result contrary to unconditional teleportation), but the relative simplicity of the proposed scheme from the perspective of design and implementation is attractive for an initial step toward that vision. Compared to other cavity QED based teleportation schemes, it does not require a two-qubit Bell-state measurement and thus can be implemented, in principle, using only two atoms interacting with a

single mode cavity. Briefly, atom B, initially prepared in the excited state, is first entangled with an initially empty cavity. Then atom A, whose state is to be teleported, interacts with the cavity. Subsequent detection of atom A in the excited state collapses atom B to the initial state of atom A.

V.A Design Specifications

An illustration of the photonic crystal chip that we propose is shown in Fig. V.1, where a single mode cavity is integrated with two parallel waveguides. The distances between various components of the circuit and the sizes are chosen in such a way that the possible sources of error due to the design of the PC are minimized. To achieve sufficiently strong and coherent atom-cavity interaction, negligibly small couplings between the cavity and the waveguide, and separated oscillatory waveguide modes we set the following size and distance parameters in our design: The actual size of the chip, which is designed in this chapter, is larger than that of the illustration. The actual height (i.e., vertical) is $\frac{17\sqrt{3}a}{2}$ and the width (i.e., horizontal) is $79a$, where a is the lattice constant. x_1, x_2, x_3, x_4 and y are $9a$, $43a$, $18a$, $9a$, and $4\sqrt{3}a$, respectively. Because of its large size, we design the chip in a 2D lattice to reduce the high computational cost of 3D crystal analysis. This is, however, a good approximation due to the ability of 2D photonic crystal defect modes to emulate those of 3D photonic crystals. This emulation issue is considered in detail in Ref. [28] and its advantages for photonic crystal based quantum logic gate design are discussed in Chapter IV (also in Ref. [36]), where we have used exactly the same lattice parameters. Thus, our 2D PC structure is chosen to emulate its 3D counterpart and is based on a triangular lattice of silicon rods with dielectric constant of 12 and lattice constant of 2.202mm for the resonant atom-cavity interaction at 51GHz. The radii of the rods and the defects are $0.175a$ and $0.071a$, respectively. The trajectories of the atoms through the PC are depicted by the differently dashed lines in Fig. V.1.

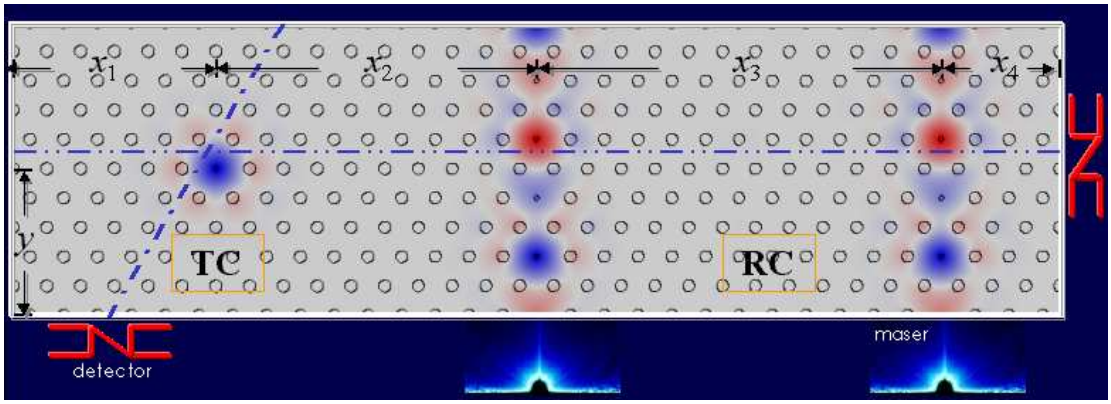

Figure V.1: Illustration of the proposed photonic crystal quantum circuit. This illustration is not to scale.

Incorporated with detectors, the cavity part of the chip operates as a teleportation circuit and the parallel waveguides act as a readout circuit to detect the teleported atomic state (see Fig. V.1). Below we use the terms teleportation circuit (TC) and readout circuit (RC), respectively, to refer those two integrated photonic crystal circuits. We choose the width of the former to be $43a$ and the latter to be $36a$ in order to avoid unwanted coupling between the two circuits. In the first part of this chapter we describe the teleportation mechanism and in the second part we explain how to detect the atomic state [37-40] within our designed PC quantum circuit (PCQC).

V.B Teleportation Circuit

The TC involves the interaction of two Rb atoms with a resonant high-Q (assumed to be larger than 10^8 to prevent cavity decoherence) single mode cavity and the detection of one of the atoms using a detector. The total Hamiltonian (Jaynes-Cummings Model) for the TC under the dipole and rotating wave approximations is given by Chapter IV:

$$H_{atom-cavity} = \frac{\hbar\omega}{2}\sum_j \sigma_z^j + \hbar\omega\alpha^\dagger\alpha + \hbar\sum_j |g(\mathbf{r}_j)|(\alpha^\dagger\sigma_-^j + \alpha\sigma_+^j) \qquad \text{(V.1)}$$

where the summation is carried over two atoms, A and B, ω is the resonant frequency, σ_z is the z-component of the Pauli spin operator and $\sigma_\pm$ are the atomic raising and lowering operators. α and $\alpha^\dagger$ are the annihilation and creation operators, respectively. $g(\mathbf{r}_j)$ is the atom-cavity coupling parameter at the position of atom j and can be written as

$$g(\mathbf{r}_j) = g_0 E(\mathbf{r}_j)/|\mathbf{E}(\mathbf{r}_m)|. \tag{V.2}$$

g_0 denotes the vacuum Rabi frequency and $\mathbf{r}_m$ is the position in the dielectric where the electric field energy density is maximum. Note that we implicitly assume in Eq. (V.2) that the atomic dipole moments, μ_{10}^j, of the atoms are aligned with the photon polarization.

In the first stage of the conditional teleportation protocol, atom B (whose trajectory is horizontal in Fig. V.1), initially in the excited state $|1\rangle_B$, traverses the cavity, which is initially in the vacuum state $|0\rangle$, with velocity V_B. Since at this stage atom A, whose state is to be teleported, is not in play, index j only takes value B in Eq. (V.1). The composite state for atom B and the cavity at time t then can be written as

$$|\Psi(t)\rangle = \cos G_B(t)|1\rangle_B|0\rangle - i\sin G_B(t)|0\rangle_B|1\rangle, \tag{V.3}$$

where

$$G_j(t) \equiv \int_{t_0}^{t} |g(\mathbf{r}_j)| d\tau. \tag{V.4}$$

The cavity we have designed in this chapter supports a transverse magnetic (TM) polarized monopole mode as illustrated in Fig. V.1. Based on the block-iterative plane wave expansion method [26], with 32 grid points per a, we find the normalized frequency of the cavity mode to be $0.3733c/a$. By setting $a = 2.202$mm, we tune the resonant wavelength to 5.9mm. At this wavelength, the atomic dipole moment for the Rb atom is taken to be 2×10^{-26}Cm. [36]

Using these parameters, we obtain $G_B(t) \cong 9\pi/4$ at time $t_1 = 51.6\mu$s at $18a$ from the left edge of the TC, if V_B is set to 767.7m/s, and hence atom-cavity

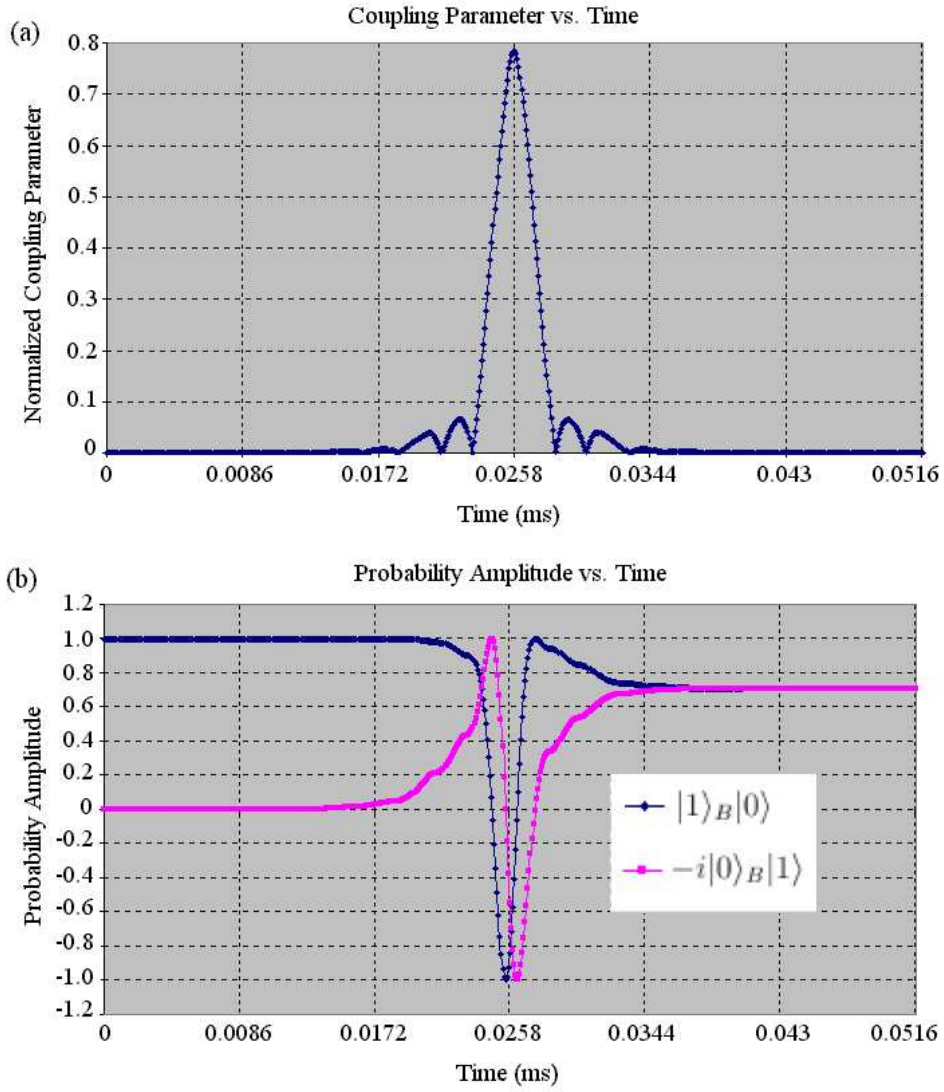

Figure V.2: (a) The time-dependent atom-cavity coupling parameter and (b) the evolution of the probability amplitudes of states $|1\rangle_B|0\rangle$ (initially at 1; shown in blue online) and $-i|0\rangle_B|1\rangle$ (initially at 0; shown in pink online) in Eq. (V.3), as atom B travels across the cavity.

entanglement in Eq. (V.3). In other words, this asymptotic (constant) value of $G_B(t)$ is the necessary condition for the completion of the entanglement process [see Eq. (V.3)] and can be satisfied only under certain circumstances at the end of the atom-cavity interaction. As atom B travels across the cavity, the time-dependent atom-cavity coupling parameter and the evolution of the probability amplitudes of states $|1\rangle_B|0\rangle$ (initially at 1; shown in blue online) and $-i|0\rangle_B|1\rangle$ (initially at 0; shown in pink online) in Eq. (V.3) are displayed in Fig. V.2. In our calculations we neglect the insignificant effect of the mode tail on the probability amplitudes of the entangled state—less than 1% beyond $18a$. Another even less significant source of error in our design is the coupling of the waveguides in the RC to the cavity [41, 42], which is simply circumvented by keeping x_2 in Fig. V.1 sufficiently large (i.e., $43a$).

Having entangled atom B and the cavity, the second stage of the conditional teleportation protocol is to inject atom A (whose trajectory is diagonal in Fig. V.1), which is initially (i.e., at time t_1) in an arbitrary (or an unknown) quantum state,

$$|\phi\rangle_A = c_0|0\rangle_A + c_1|1\rangle_A. \tag{V.5}$$

Thus at time t_1, the state of the whole system is written as

$$|\varphi(t_1)\rangle \cong \frac{1}{\sqrt{2}}(c_0|0\rangle_A + c_1|1\rangle_A)(|1\rangle_B|0\rangle - i|0\rangle_B|1\rangle). \tag{V.6}$$

Once atom A arrives at the detector, right before the detection, say at time $t_1 + t_2$, the state of the whole has evolved into

$$\begin{aligned} |\varphi(t_1+t_2)\rangle \;\cong\; & \frac{1}{\sqrt{2}}\{c_0|0\rangle_A|1\rangle_B|0\rangle - ic_0|0\rangle_B[\cos G_A(t_2)|0\rangle_A|1\rangle - i\sin G_A(t_2)|1\rangle_A|0\rangle] \\ & + c_1|1\rangle_B[\cos G_A(t_2)|1\rangle_A|0\rangle - i\sin G_A(t_2)|0\rangle_A|1\rangle] \\ & - ic_1|0\rangle_B[\cos\sqrt{2}G_A(t_2)|1\rangle_A|1\rangle - i\sin\sqrt{2}G_A(t_2)|0\rangle_A|2\rangle]\}, \end{aligned} \tag{V.7}$$

which would reduce to Eq. (V.6) of Ref. [33], if $|g(\mathbf{r}_j)|$ were spatially uniform in Eq. (V.1).

In the derivation of Eq. (V.7), the contribution of $|g(\mathbf{r}_B)|$ in Eq. (V.1) is neglected, since atom B is sufficiently far from the cavity when atom A is injected. At times close to t_1, although $|g(\mathbf{r}_B)| \approx |g(\mathbf{r}_A)|$, neither atom alone nor combined can start the Rabi oscillation (see Chapter IV). On the other hand, as atom A proceeds its coupling to the cavity mode increases, while the coupling of atom B decreases. This means that the effect of $|g(\mathbf{r}_B)|$ becomes even less significant for times greater than t_1.

The third stage of the conditional teleportation protocol is the measurement of the state of atom A. If the result is $|1\rangle_A$, the combined state of atom B and the cavity becomes

$$\Psi(t_1+t_2) \cong \frac{-c_0 \mathrm{sin} G_A(t_2)|0\rangle_B|0\rangle + c_1 \mathrm{cos} G_A(t_2)|1\rangle_B|0\rangle - ic_1 \mathrm{cos}\sqrt{2} G_A(t_2)|0\rangle_B|1\rangle}{[|c_0|^2 \mathrm{sin}^2 G_A(t_2) + |c_1|^2 \mathrm{cos}^2 G_A(t_2) + |c_1|^2 \mathrm{cos}^2 \sqrt{2} G_A(t_2)]^{1/2}}. \tag{V.8}$$

The denominator in Eq. (V.8) is simply the norm of the unnormalized state in the numerator. We obtain $G_A(t_2) \cong 7\pi/4$ [i.e., the necessary condition to be satisfied for the completion of the teleportation process, see Eq. (V.8)] in Eq. (V.8) if we set $V_A = 987\mathrm{m/s}$, and thus

$$|\phi\rangle_B \cong c_0|0\rangle_B + c_1|1\rangle_B. \tag{V.9}$$

That is, the initial arbitrary (or unknown) state of atom A has been teleported to atom B, conditional on detecting atom A in state $|1\rangle_A$, which occurs with probability 1/4. The time-dependent coupling parameter for atom A and the evolution of the probability amplitudes of states $-c_0|0\rangle_B|0\rangle$ (initially at 0; shown in pink online), $c_1|1\rangle_B|0\rangle$ (dark curve initially at 1; shown in blue online), and $-ic_1|0\rangle_B|1\rangle$ (light curve initially at 1; shown in yellow online) for the unnormalized state (i.e., the numerator) in Eq. (V.8) are shown in Fig. V.3. Note that as time elapses Eq. (V.8) transforms into Eq. (V.9). Note also that atom B arrives at $31a$ at time t_1+t_2 (i.e., 88.9μs). After an additional distance of $12a$, the fourth stage of our conditional teleportation and detection protocol begins as atom B enters the RC at time $t_1+t_2+t_3$ (i.e., 123.3μs). Next we study how to detect its state.

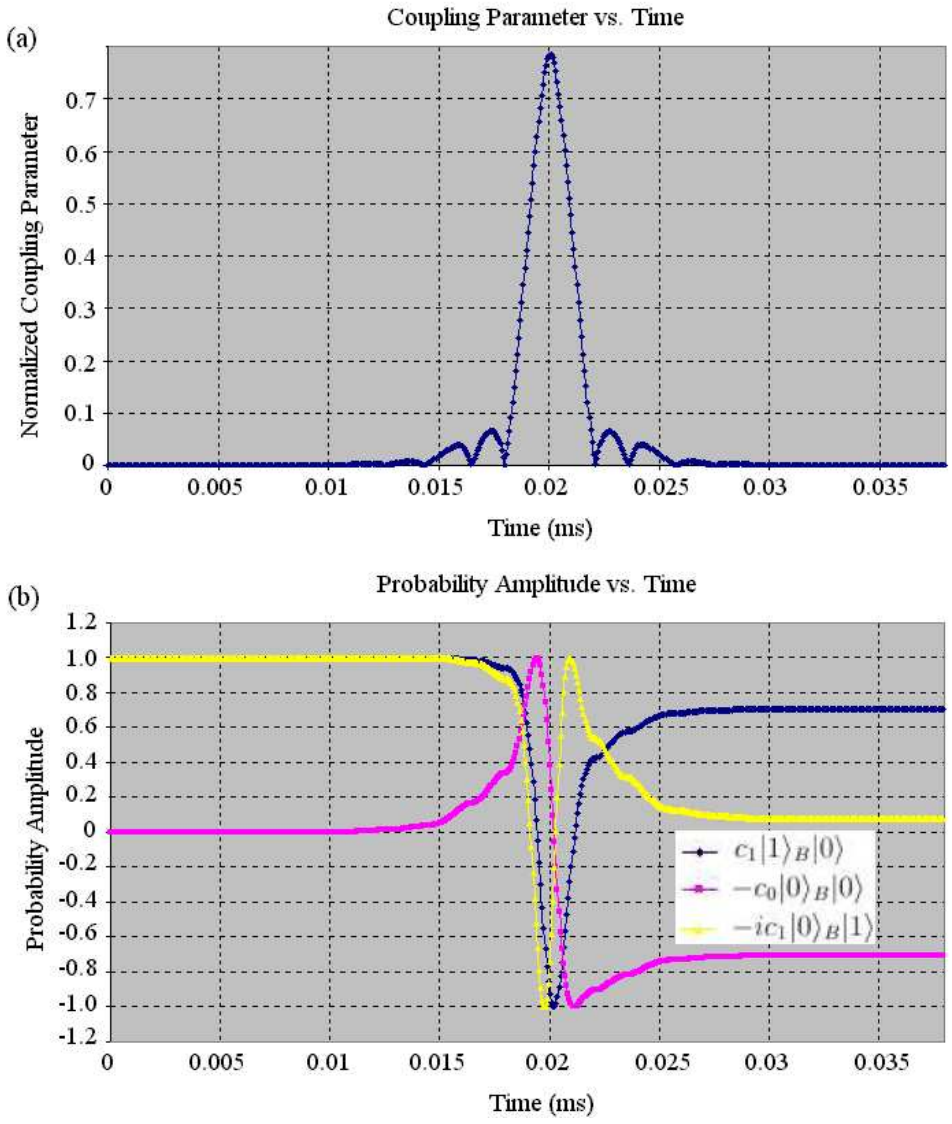

Figure V.3: (a) Time-dependent coupling parameter for atom A and (b) the evolution of the probability amplitudes of states $-c_0|0\rangle_B|0\rangle$ (initially at 0; shown in pink online), $c_1|1\rangle_B|0\rangle$ (dark curve initially at 1; shown in blue online), and $-ic_1|0\rangle_B|1\rangle$ (light curve initially at 1; shown in yellow online) for the unnormalized state (i.e., numerator) in Eq. (V.8).

V.C Readout Circuit

We can write the atom-maser Hamiltonian, under the dipole and rotating wave approximations, as [43]

$$H_{atom-maser} = \frac{\hbar\omega}{2}\sigma_z + \hbar\frac{\Omega(\mathbf{r})}{2}(e^{i\omega_m t}\sigma_- + e^{-i\omega_m t}\sigma_+) \tag{V.10}$$

where

$$\Omega(\mathbf{r}) = \frac{2\mu_{10}|\mathbf{E}(\mathbf{r})|}{\hbar} \tag{V.11}$$

is the Rabi frequency and ω_m is the frequency of the maser, whose polarization is also matched with the atomic dipole moment, μ_{10}, of the atom. In the following we will first assume a constant $\Omega(\mathbf{r}) = \Omega_0$ to simplify the explanation of the detection mechanism, and then we will modify the analysis to apply to our proposed PCQC, where $\Omega(\mathbf{r})$ is not constant.

Assume that atom B in state $|\phi\rangle_B$ [see Eq. (V.9)] enters a uniform field region at time t and interacts during a time interval t_4. Then its probability amplitudes at time $t + t_4$ can be computed to be [4]

$$c_0(t+t_4) = \{[i\cos\Theta\sin(\frac{\Lambda t_4}{2}) + \cos(\frac{\Lambda t_4}{2})]c_0 + i\sin\Theta\sin(\frac{\Lambda t_4}{2})e^{i\omega_m t}c_1\}e^{i\omega_m t_4/2}, \tag{V.12}$$

$$c_1(t+t_4) = \{i\sin\Theta\sin(\frac{\Lambda t_4}{2})e^{-i\omega_m t}c_0 + [-i\cos\Theta\sin(\frac{\Lambda t_4}{2}) + \cos(\frac{\Lambda t_4}{2})]c_1\}e^{-i\omega_m t_4/2}. \tag{V.13}$$

where cosΘ, sinΘ, and Λ are defined as follows.

$$\Lambda \equiv \sqrt{(\omega-\omega_m)^2 + \Omega_0^2}, \tag{V.14}$$

$$\cos\Theta \equiv \frac{(\omega-\omega_m)}{\Lambda}, \tag{V.15}$$

$$\sin\Theta \equiv -\frac{\Omega_0}{\Lambda}. \tag{V.16}$$

After this interaction, atom B interacts with a second uniform field region for the same time interval t_4 starting at time $t + t_4$. The probability amplitudes, $c_0(t+2t_4)$ and $c_1(t+2t_4)$, in this case can be also found from equations (V.12) and (V.13) by replacing c_0, c_1, and t with $c_0(t+t_4)$, $c_1(t+t_4)$, and $t+t_4$, respectively.

Note that one can also treat these two uniform field regions as a single uniform field region with an interaction time of $2t_4$. In this chapter, however, we also intend to show that our RC has the potential to be an atomic interferometer, like a Ramsey interferometer [4]. In order to hint how this could work, we design two separate oscillating field regions based on two parallel waveguides as discussed below. Implementation of a fully working interferometer, however, requires further consideration.

After atom B has interacted with the two uniform field regions, we can implicitly write the final state of atom B at time $t + 2t_4$, before detection as

$$|\phi(t + 2t_4)\rangle_B \cong (c_0 c_{00} + c_1 c_{10})|0\rangle_B + (c_0 c_{01} + c_1 c_{11})|1\rangle_B \tag{V.17}$$

where c_{ij} is the probability amplitude of the atom being in state $|j\rangle$ at time $t + t_4$ if it is initially prepared in state $|i\rangle$. For example if the atom is initially in state $|1\rangle$ then it evolves into $c_{10}|0\rangle + c_{11}|1\rangle$ at time $t + t_4$.

Having interacted with both waveguides, atom B is finally detected by an ionization detector, as shown in Fig. V.1. The probability of finding it in the excited state is

$$P_1 = |c_0|^2|c_{01}|^2 + |c_1|^2|c_{11}|^2 + [c_0^{(r)}c_1^{(r)} + c_0^{(i)}c_1^{(i)}]2(c_{01}c_{11}^{\star})^{(r)} + [c_0^{(r)}c_1^{(i)} + c_0^{(i)}c_1^{(r)}]2(c_{01}c_{11}^{\star})^{(i)}. \tag{V.18}$$

Superscripts (r) and (i) represent the real and imaginary part, respectively.

We can simplify Eq. (V.18) by writing Eq. (V.9) in the form

$$|\phi\rangle_B \cong \cos(\theta/2)|0\rangle_B + \sin(\theta/2)e^{i\varphi}|1\rangle_B \tag{V.19}$$

where we have implicitly set $c_0^{(r)} = \cos(\theta/2)$, $c_0^{(i)} = 0$, $c_1^{(r)} = \sin(\theta/2)\cos\varphi$, and $c_1^{(i)} = \sin(\theta/2)\sin\varphi$.

Then, at four different $\Delta \equiv \omega_m - \omega$ values we calculate $|c_{01}|^2$, $|c_{11}|^2$, $2(c_{01}c_{11}^{\star})^{(r)}$, and $2(c_{01}c_{11}^{\star})^{(i)}$ directly from the system parameters using Eqs. (V.12) and (V.13); and measure only P_1 using field ionization detector. Thus having obtained four equations, we can find $|c_0|^2$, $|c_1|^2$, $[c_0^{(r)}c_1^{(r)} + c_0^{(i)}c_1^{(i)}]$, $[c_0^{(r)}c_1^{(i)} - c_0^{(i)}c_1^{(r)}]$

and hence $|\phi\rangle_B$. Note that, although we have only two unknowns in Eq. (V.19), it is convenient to use four equations due to the form of Eq. (V.18). This demonstrates that one could detect a teleported (or an arbitrary) unknown state with our proposed device, provided that P_1 is measured by employing an atomic beam of identically prepared single atoms, since multiple observations are necessary to estimate the probability. Since the TC only has a 25 percent conditional success rate, incoming atoms to the RC will not be identical. Thus if atom A of the relevant pair is not detected in the excited state, the corresponding atom B measurement is discarded from the calculation of P_1.

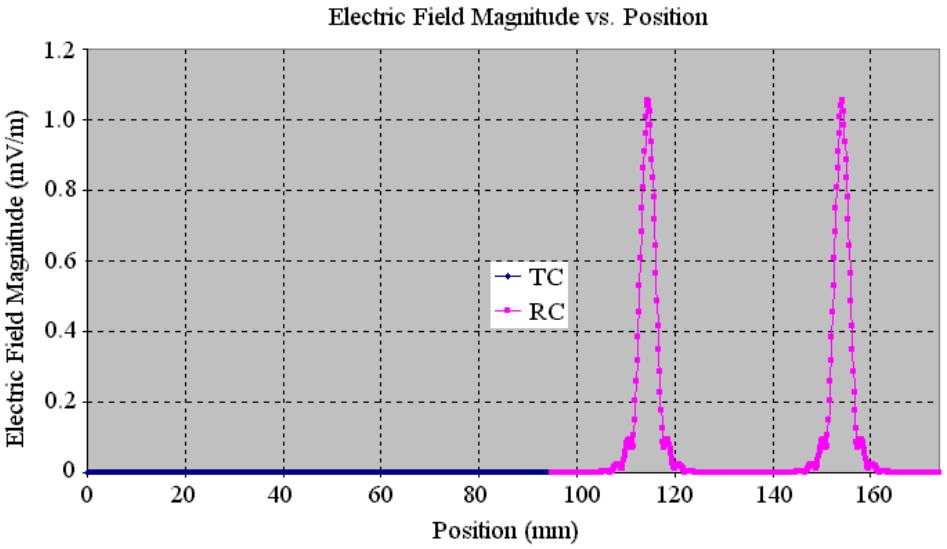

Figure V.4: The steady-state cross section of the electric field magnitude, for $\Delta = 0$, along the path of atom B (see text).

Finally, we describe how to apply these ideas to our proposed PCQC. Remember that atom B in state $|\phi\rangle_B$ enters the RC at time $t_1 + t_2 + t_3$. The steady-state mode profiles of the waveguides are calculated by the two-dimensional-finite-difference-time-domain (2D-FDTD) method with discretizations of $\frac{a}{13}$ and $\frac{a}{13}\frac{\sqrt{3}}{2}$ in the horizontal and vertical directions, respectively. We have designed the waveguides as coupled-cavity-waveguides [44, 45] to allow the atoms sufficiently large void regions through which to travel freely without a resonant-dipole-dipole-

interaction or the Casimir-Polder effect (see Fig. V.1). The steady-state cross section of the electric field magnitude, for $\Delta = 0$, along the path of atom B is shown in Fig. V.4. At the steady state the coupling between the two parallel waveguides [46-49] is not significant.

In our calculations we assume that atom B interacts with two separate nonuniform waveguide modes of total width $36a$, shown by the part of the curve in Fig. V.4 to the right of approximately 95mm (shown in pink online). In other words we truncated their tails (the part of the curve to the left of approximately 95mm in Fig. V.4; shown in blue online), which overlap with the cavity mode. The effect of this truncation in our design is observed to be negligibly small. We have observed that the coupling of waveguide modes to the cavity mode is less than the cavity coupling to waveguides, which does not affect the probability amplitudes by more than 0.6%.

Since there is no feedback mechanism, as there is in the atom-cavity interaction, the atom-waveguide interaction can be described by a Markoff approximation. In other words, when an atom emits a photon into the waveguide, the photon leaves the interaction region immediately and cannot act back on the atom. Then the waveguides must be designed in such a way that total rate of spontaneous emission into the waveguide and the free-space lossy modes is sufficiently low as atom B traverses them. In our design considering the estimated effective transverse cross section of the corresponding three-dimensional waveguide mode the maximum probability of spontaneous emission for a given atom is estimated to be on the order of 10^{-4} [50]. Thus, it is safe to assume that the Bloch vector of atom B can be manipulated without being correlated with the defect mode [51] of the waveguides.

The total interaction time with the parallel waveguides is also $2t_4$, as in the uniform case above, with t_4 (i.e., 51.6μs) for each. Note that, since the Rabi frequency, $\Omega(\mathbf{r})$, is proportional to $|\mathbf{E}(\mathbf{r})|$, the part of the curve in Fig. V.4 to the right of approximately 95mm (shown in pink online) also describes the position

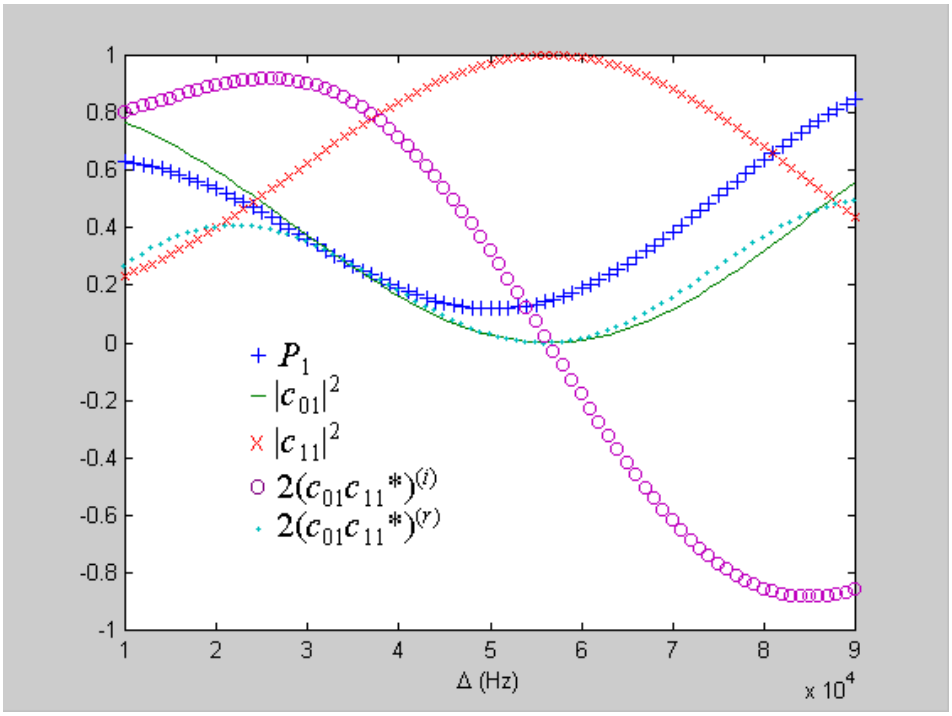

Figure V.5: Calculated values of $|c_{01}|^2$ (solid line; shown in green online), $|c_{11}|^2$ ('$\times$'; shown in red online), $2(c_{01}c_{11}^{\star})^{(r)}$ (dotted line; shown in light blue online), $2(c_{01}c_{11}^{\star})^{(i)}$ ('o'; shown in purple online), and to be measured value of P_1 ('+'; shown in dark blue online) (see text).

dependence of the Rabi frequency if multiplied by $2\mu_{10}/\hbar$. Thus the evolution of the teleported state, as it interacts with the parallel waveguides, can be determined numerically by exploiting equations (V.12) and (V.13) successively, with t_4 replaced with the maximum tolerated time-step, which is 44ns in our case (the time for atom B to travel $a/65$).

Thus, right before the detection, the final state is $|\phi(t_1+t_2+t_3+2t_4)\rangle_B$, which can be written in the form of Eq. (V.17). The probability of detecting atom B in the excited state is then given by Eq. (V.18), and following the same method as in the uniform case above, we can easily detect $|\phi\rangle_B$, the state output by TC.

As an example, assume that the final state of the TC [see Eq. (V.19)] is

$$|\phi\rangle_B = \cos(\pi/8)|0\rangle_B + \sin(\pi/8)e^{-i\pi/6}|1\rangle_B \qquad \text{(V.20)}$$

The corresponding calculated values of $|c_{01}|^2$ (solid line; shown in green online), $|c_{11}|^2$ ('$\times$'; shown in red online), $2(c_{01}c_{11}^{\star})^{(r)}$ (dotted line; shown in light blue online), $2(c_{01}c_{11}^{\star})^{(i)}$ ('o'; shown in purple online), and the value of P_1 ('+'; shown in dark blue online), which will be measured, are shown in Fig. V.5. Picking four different values of Δ, we can easily determine that $\theta = \pi/4$ and $\varphi = -\pi/6$.

V.D Discussion

Our readout scheme does not require 100% detection efficiency. Finite detection efficiency with a relatively larger atomic ensemble can lead to an arbitrarily accurate result. For example, with a detection efficiency of 40% (as in Ref. [38]), our detection scheme gives about $\pm 4\%$ error using the Poisson distribution (confidence level 99%) in P_1 out of 10^4 events. Increasing the number of events to 10^5 reduces the error to about $\pm 1\%$ with the same confidence level. Using the latter number, we have estimated that the maximum error in the probability amplitudes (i.e., $c_0^{(r)}$, $c_1^{(r)}$, and $c_1^{(i)}$) is about 0.1; for most states the error is at least an order of magnitude smaller.

The total operation time in our circuit is 226.5μs compared to the 30ms lifetime of the Rb atoms, which are prepared one at a time in a circular Rydberg state with principal quantum number 50 (ground) or 51 (excited) [52].

Note that we need a maser (as assumed in §V.C) or a coherent microwave source operating around the atomic transition frequency (i.e., 51GHz), which allows measurements at four different detunings of 10s of kHz as shown in Fig. V.5. We can achieve this task using, for example, continuously tunable backward wave oscillators (BWO) which can generate coherent, highly monochromatic and linearly polarized radiation [53]. Minimum frequency steps of 100Hz and frequency stability of up to 10^{-11} can be obtained for BWOs, [54] using an external 5MHz signal from a rubidium standard. This would be more than sufficient for our purpose.

Due to the electromagnetic scalability of photonic crystals one could also

implement this device in more compact form in the optical regime. In this case, however, the electric field gradient and the momentum recoil of the atom would also have to be analyzed. In the microwave regime studied in this chapter, the small momentum recoil due to a microwave photon does not cause external degrees of freedom (i.e., the position or momentum) of the atom to couple with its internal degrees of freedom (i.e., the ground or excited state).

To implement our PCQC, one should also engineer the surface states, which reside at the air-photonic crystal interfaces. These surface modes may also become correlated with the atoms exiting the crystal. These modes can be handled, however, by appropriate termination of the crystal [55-58].

Portions of this chapter were presented in the paper: D. Ö. Güney and D. A. Meyer, "*Integrated conditional teleportation and readout circuit based on a photonic crystal single chip*", J. Opt. Soc. Am. B **24**, 391 (2007).

Chapter VI

Analog Design: Optoelectronic Quantum Simulation of Klein Paradox

In 1968, Veselago [64] demonstrated that the refractive index (n) of a material should be negative when permittivity ϵ and permeability μ are simultaneously negative. In his paper, Veselago called such materials left-handed materials (LHMs) and treated them purely formally, since existed no such material at that time. Nonetheless, he gave a number of arguments as to how one should look for such materials. He pointed out how the Doppler effect, the Cerenkov radiation, and even Snell's law are inverted. He also considered some questions related with the physical realization of materials with $\epsilon < 0$ and $\mu < 0$.

It has been recently demonstrated that an effective LHM, which consists of periodic array of split ring resonators (SRRs) and continuous wires manifests $n < 0$ for a certain frequency region in the microwave regime, which then leads to anomalous electromagnetic wave propagation [65-66]. An experimental verification of a negative index has been established by R. A. Shelby et al [67].

A treatment of the refraction of physical electromagnetic waves in newly developed LHMs has been recently put forward by Valanju, et al. while raising

objections about the previous interpretations of the wave refraction phenomena in these peculiar materials [68]. However, it has been shown later that in an isotropic negative index medium (NIM), a modulated beam with finite width exhibits negative refraction, while the modulation interference fronts do not propagate not normal to the group velocity [69]. Refraction of the electromagnetic waves in media with negative index has also been verified very recently by S. Foteinopoulou, et al. They exploited a photonic crystal structure, which almost isotropically exhibits negative effective refractive index for certain modes. They also explained using the finite-difference time-domain (FDTD) method, why causality and speed of light are not violated [70].

In this chapter, we show how the wave propagation and refraction in an isotropic NIM displays exactly the similar phenomena with that of a well known quantum relativistic problem, which is known as the Klein paradox. To accomplish this, we will first underline some significant results for the refraction at the interface between a positive refractive index material and effectively LHM. We will defer the Klein paradox till §VI.B.

Although one-dimensional (1D) scattering from a Klein step has been considered in various publications [71–73], to best of our knowledge such a two-dimensional (2D) scattering from a semi-infinite Klein step potential is treated first here inspired by the works about its optical counterpart, LHM [64, 68-70]. It is amazing that extra one-dimension not only verifies the Klein paradox existing in one dimension but also shows the negative refraction of matter waves which never has been recorded before. It is not the first time, however, the Klein paradox is shown to exist in Maxwell's equations for the problem of optical scattering from excited targets [74].

In §VI.C, we will note how the LHMs could be used to simulate the problems where the Klein paradox exists and vice versa. Our work highlights richer possibilities of novel optical devices by calling attention to works, which have already been established in the field of relativistic quantum mechanics as well as

calling attention for the search of many other useful quantum mechanical potential barrier problems for various applications in optics. The converse is also true. Implemented or demonstrated optical devices and phenomena could be analog processors and motivating guides for the more abstract quantum world, since the optical experiments are in general easier and cheaper to realize physically than high energy physics experiments. LHMs and photonic band gap (PBG) materials, which are sometimes called artificial semiconductors for light, are only two kinds of fruits among others harvested from this fertile optics-quantum field.

VI.A Left Handed Materials

Following the suggestions given in Refs. [64, 68-70] about wave propagation in the LHM, we assume the geometry shown in Fig. VI.1, to study wave refraction at the interface between two semi-infinite layers of optical media.

Wave vector, $\mathbf{K}_L$ (L denotes LHM), of the electric field incident on the frequency dependent NIM from vacuum makes an angle, Θ_i, with the normal to the boundary located at $z = 0$. We assume the incident electric field to be a plane wave and linearly polarized along the y-axis. Thus its wave vector lies in the xz-plane. That is

$$E(\mathbf{r}, t) = \mathrm{e}^{i(\mathbf{K}_L \cdot \mathbf{r} - \omega t)}, \tag{VI.1}$$

with unit amplitude. It can be shown by the phase matching condition and causality for the refracted wave that the transmitted wave vector $\mathbf{Q}_L$ is

$$\mathbf{Q}_L = |\mathbf{K}_L|_x \hat{\mathbf{x}} + \sigma \sqrt{n^2 |\mathbf{K}_L|^2 - |\mathbf{K}_L|_x^2} \hat{\mathbf{z}}. \tag{VI.2}$$

$\sigma = +1$ for the positive index medium and -1 for the NIM (or LHM) [68]. From the definition of group velocity for isotropic, low loss materials, the refracted beam has the group velocity

$$\mathbf{V}_g = \frac{\mathbf{Q}_L}{|\mathbf{Q}_L|}\frac{\sigma nc}{n_g}, \tag{VI.3}$$

where c is the light speed and n_g is the group index, which is by causality always greater than unity [69]. Thus the group velocity is always antiparallel to the phase velocity of the refracted wave for $\sigma = -1$. Since the time-averaged energy flux $\langle \mathbf{S} \rangle = \langle u \rangle \mathbf{V}_g$ [70], where $\langle u \rangle$ is the time-averaged energy density, it is clear from Eqns. (VI.2) and (VI.3) and by causality that the incident wave should undergo negative refraction.

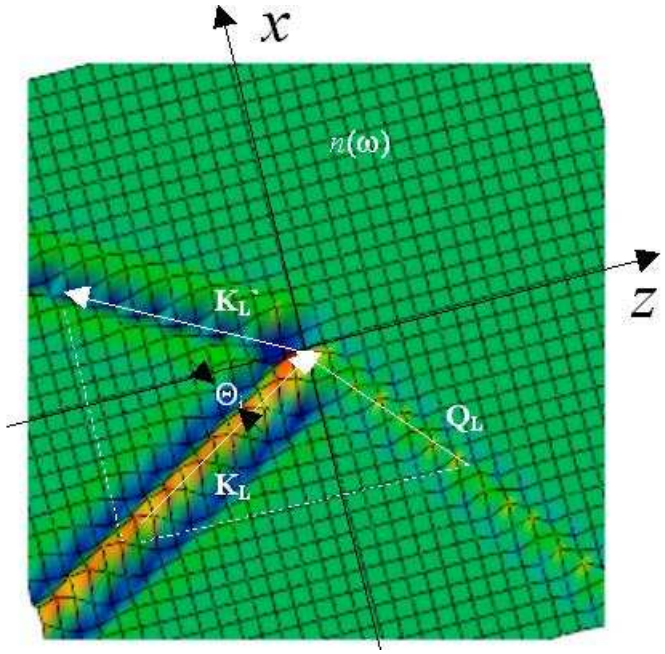

Figure VI.1: Negative refraction of a beam of photons at the interface between a PIM ($z < 0$) and a NIM ($z > 0$). The white arrows indicate the wavevector for an arbitrary wave ($\mathbf{K}_L$) in the incident flux and its corresponding transmitted ($\mathbf{Q}_L$) and reflected ($\mathbf{K'}_L$) wavevector. The angle between the boundary normal and $\mathbf{K}_L$ is Θ_i.

Field transmission (τ_L) and reflection (ρ_L) coefficients for NIM can be determined by matching the electric and magnetic fields at the interface between positive and NIM. That gives,

$$\tau_L = \frac{2\mu|\mathbf{K}_L|_z}{\mu|\mathbf{K}_L|_z + |\mathbf{Q}_L|_z} \tag{VI.4}$$

$$\rho_L = \frac{\mu|\mathbf{K}_L|_z - |\mathbf{Q}_L|_z}{\mu|\mathbf{K}_L|_z + |\mathbf{Q}_L|_z}. \tag{VI.5}$$

where μ is the permeability of the NIM assuming that the electromagnetic wave is incident from a non-magnetic material. Power transmission and reflection coefficients can be obtained from the average energy flux $\langle \mathbf{S} \rangle = (c/8\pi)\Re[\mathbf{E}\times\mathbf{H}^*]$. Thus we have, respectively,

$$T_L = \frac{|\tau_L|^2|\mathbf{Q}_L|_z}{\mu|\mathbf{K}_L|_z}, \tag{VI.6}$$

$$R_L = |\rho_L|^2. \tag{VI.7}$$

It can be shown from Eq. (VI.2) that if the incident beam is a superposition of two component waves with the same direction of propagation but different frequencies, they are refracted at different angles. This results in interference fronts, which are not normal to the group velocity. For example, following the suggestions of D. R. Smith et al [69], if we have two finite width component waves, the resultant interference front exhibits sideways motion relative to the beam. Further from the interface, in the NIM, these two component waves are sufficiently separated that no interference pattern is observed.

VI.B Klein Paradox

Now, we turn our attention to the Klein paradox. Although the nonrelativistic quantum mechanics of the scattering of a quantum particle is straightforward, the quantum relativistic case displays quite peculiar situation called the Klein Paradox [72]. In the following we discuss 2D scattering of a particle from a

Klein step potential and consider some of these peculiarities, which include transmission through strong potential barrier, pair production, negative transmission and negative refraction.

We consider a spin-0 particle, which is governed by the KG equation,

$$[\mathbf{E} - V(\mathbf{r})]^2|\Psi\rangle = (-c^2\mathbf{P}^2 + m^2c^4)|\Psi\rangle, \tag{VI.8}$$

where m is the mass of the particle. The problem is described in Fig. VI.2. A particle confined to the xz-plane with energy $E = (P^2c^2 + m^2c^4)^{1/2}$ is incident on a potential barrier, at angle θ_i with the normal to the interface. The potential, $V(\mathbf{r})$, is assumed to be 0 on the incident side and it is described by a 2D Klein step potential, $V(\mathbf{r}) = V$ for $z > 0$.

In the position representation, Eqn. (VI.8) becomes

$$\{[i\hbar\partial_t - V(\mathbf{r})]^2 + c^2\hbar^2\nabla^2 - m^2c^4\}\Psi(\mathbf{r}, t) = 0. \tag{VI.9}$$

For $z < 0$, we consider a positive energy incoming wave of the form

$$\Phi(\mathbf{r}, t) = \mathrm{e}^{i(\mathbf{K}_K\cdot\mathbf{r} - Et/\hbar)}. \tag{VI.10}$$

Note that Eqn. (VI.10) is similar to Eqn. (VI.1) given for the y-polarized electric field.

We look for the solution of the form

$$\Psi(\mathbf{r}) = \phi(-z)[\mathrm{e}^{-iEt/\hbar}(\mathrm{e}^{i\mathbf{K}_K\cdot\mathbf{r}} + \rho_K\mathrm{e}^{i\mathbf{K}_K^{'}\cdot\mathbf{r}})] + \phi(z)\tau_K\mathrm{e}^{-iEt/\hbar}\mathrm{e}^{i\mathbf{Q}_K\cdot\mathbf{r}}. \tag{VI.11}$$

Substitution of Eqn. (VI.11) into Eqn. (VI.9) and satisfying the phase matching condition yields

$$E^2 = c^2\hbar^2|\mathbf{K}_K|^2 + m^2c^4, \quad z < 0 \tag{VI.12}$$

$$c^2\hbar^2|\mathbf{Q}_K|^2 = (E - V)^2 - m^2c^4, \quad z > 0. \tag{VI.13}$$

We can analyse Eqn. (VI.13) by considering three cases. If the potential V is weak, such that it is less than $E - mc^2$, then $|\mathbf{Q}_K|$ has to be real. For the intermediate case, where $E - mc^2 < V < E + mc^2$, $|\mathbf{Q}_K|$ is purely imaginary, so the trasmitted field is damped.

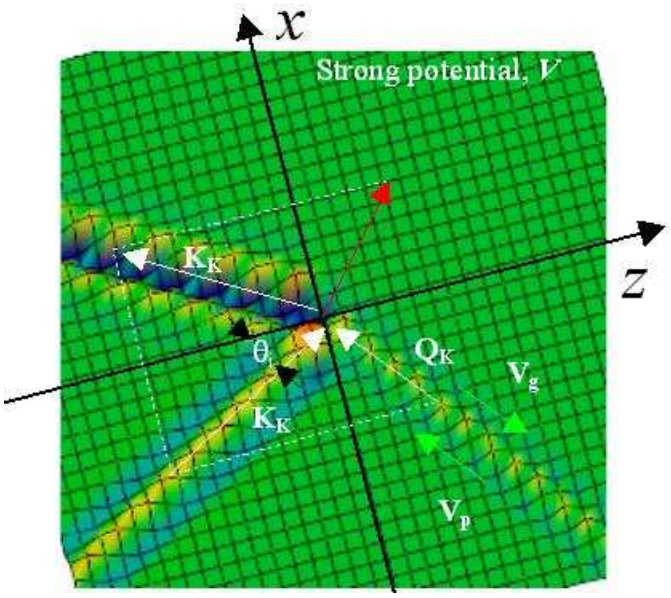

Figure VI.2: Negative refraction of a beam of spin-zero particles at the boundary of a strong potential, V, for $z > 0$. White arrows indicate wave vectors for an arbitrary wave ($\mathbf{K}_K$) component in the incident flux and its corresponding transmitted ($\mathbf{Q}_K$) and reflected ($\mathbf{K'}_K$) counterparts. The wave vector shown with red is not allowed due to the causality and phase matching conditions at the interface. The green arrows show the directions of group ($\mathbf{V}_g$) and phase ($\mathbf{V}_p$) velocities, which are antiparallel. The angle between $\mathbf{K}_K$ and the normal to the interface is Θ_i.

We concentrate on the strong potential case, that is $V > E + mc^2$. Note that we again have real $|\mathbf{Q}_K|$. Even when the energy of the incident particle is less than the height of the potential, the transmitted particle doesn't necessarily undergo any attenuation. This is a classically (also in nonrelativistic quantum mechanics) forbidden situation.

The question thus naturally arises: What is the direction of the momen-

tum of the transmitted wave, $\mathbf{Q_K}$, for the strong potential case? Since $E(\mathbf{Q}_K) = E(|\mathbf{Q}_K|)$ in Eqn. (VI.13), for the group velocity of the transmitted wave we have

$$\mathbf{V}_g = \frac{\mathrm{d}E(|\mathbf{Q}_K|)}{\mathrm{d}|\mathbf{Q}_K|} = \frac{\hbar c \mathbf{Q}_K}{E - V}. \tag{VI.14}$$

Regardless of Eqn. (VI.14), to satisfy the phase matching condition at the interface, incoming wave in Eqn. (VI.10) should either follow white-path or red-path. Since the group velocity is the velocity of the moving wave packet, if we allow white path it looks as if the transmitted wave packet came in from positive-z side. This contradicts the causality which only allows an incoming wave packet from negative-z side. Thus, it is clear that $\mathbf{Q}_K$ in Eqn. (VI.14) should be directed toward the boundary as shown in Fig. VI.2.

Since the momentum, $\mathbf{Q}_K$, of the transmitted wave is a function of the energy of the incident particle E, we can write Eqn. (VI.13) in terms of its components as

$$c^2\hbar^2|\mathbf{Q}_K|_z^2 = c^2\hbar^2|\mathbf{K}_K|_z^2 - 2EV + V^2. \tag{VI.15}$$

Remember that we found $|\mathbf{Q}_K|$ to be real in the strong potential case, where $E < V$ and we know that $|\mathbf{Q}_K|_x^2 = |\mathbf{K}_K|_x^2$ is real. So we immediately conclude from Eqn. (VI.15) that $|\mathbf{Q}_K|_z^2$ can be real as well as purely imaginary, even though $|\mathbf{Q}_K|$ is real. Now we closely examine the condition which makes $|\mathbf{Q}_K|_z$ either real or purely imaginary. To achieve that we define the excess potential as

$$\Delta\epsilon \equiv V - E - mc^2. \tag{VI.16}$$

If we substitute V in Eqn. (VI.16), into Eqn. (VI.15) we obtain

$$c^2\hbar^2|\mathbf{Q}_K|_z^2 = 2mc^2(\Delta\epsilon) + (\Delta\epsilon)^2 - c^2\hbar^2|\mathbf{K}_K|_x^2. \tag{VI.17}$$

Since $\Delta\epsilon$ is arbitrarily chosen, for a given incident particle with mass m, it is interesting that the stronger the potential the more momentum transfer

to the z-component of the transmitted wave occurs without any damping. As we increase the height of the potential step, keeping m and $|\mathbf{K}_K|_x$ the same, the angle of refraction approaches zero. However, for the relatively weaker potential such that $0 < \Delta\epsilon < -mc^2 + (c^2\hbar^2|\mathbf{K}_K|_x^2 + m^2c^4)^{1/2}$, the transmitted wave is attenuated as it propagates through the Klein step. This is contrary to classical physics. More interestingly it does not occur in the 1D scattering from a strong potential of the same kind, either. First, this could be easily understood from Eqn. (VI.17) by setting $|\mathbf{K}_K|_x = 0$, so that $|\mathbf{Q}_K|_z$ never becomes purely imaginary. Second, Eqn. (VI.17) also states that pair production in 2D scattering requires an additional potential of $\Delta\epsilon = -mc^2 + (c^2\hbar^2|\mathbf{K}_K|_x^2 + m^2c^4)^{1/2}$ for given m and $|\mathbf{K}_K|_x$, compared to 1D scattering. Besides, in the resonant state of the Klein step, $\Delta\epsilon = -mc^2 + (c^2\hbar^2|\mathbf{K}_K|_x^2 + m^2c^4)^{1/2}$, the incident wave is totally reflected without any damping inside the potential barrier.

The expressions for ρ_K and τ_K in Eqn. (VI.11) are determined by imposing the boundary conditions on $\Psi(\mathbf{r})$ and $\partial_z\Psi(\mathbf{r})$ at the interface, $z = 0$. Thus we obtain

$$\tau_K = \frac{2|\mathbf{K}_K|_z}{|\mathbf{Q}_K|_z + |\mathbf{K}_K|_z} \tag{VI.18}$$

$$\rho_K = \frac{|\mathbf{Q}_K|_z - |\mathbf{K}_K|_z}{|\mathbf{Q}_K|_z + |\mathbf{K}_K|_z}. \tag{VI.19}$$

We find the transmission T_K and reflection R_K coefficients from the probability current, which is given by

$$\mathbf{J} = \frac{1}{2im}(\Psi^\star\nabla\Psi - \Psi\nabla\Psi^\star). \tag{VI.20}$$

If $|\mathbf{Q}_K|_z$ is purely imaginary (i.e. *relatively weaker* strong potential), we get

$$R_K = |\rho_K|^2 = 1, \;\; T_K = 0. \tag{VI.21}$$

This is the same result with the intermediate Klein step in 1D. If $|\mathbf{Q}_K|_z$ is real, however, the coefficients are

$$T_K = \frac{|\mathbf{Q}_K|_z |\tau_K|^2}{|\mathbf{K}_K|_z} \tag{VI.22}$$

$$R_K = |\rho_K|^2. \tag{VI.23}$$

Note that the probability is conserved at the expense of a negative transmission coefficient and a reflection coefficient exceeding unity. This paradox can be resolved by employing the notion of particle-antiparticle pair production due to the strong potential. The antiparticles create a negative charged current moving right inside the potential barrier, while the particles are reflected and combined with the incident beam leading to a positively charged current moving to the left. This is the essence of the peculiarities in Eqn. (VI.22) and Eqn. (VI.23).

VI.C Analog Quantum Simulation

Having presented the two problems, we realize that wave propagation and refraction in the LHM is exactly the same with that of the matter wave interacting with the Klein step potential considered here. They both have reversed group and phase velocity and manifest negative refraction. Moreover, we have mathematical expressions above, which connect these two problems to each other, to help us simulate one with the other. The question we would like to address now is how to simulate the Klein paradox using LHMs? Although this is possible under many different transformations, here, we only consider the following transformation to simulate the Klein paradox. To be more precise in some results or to solve other specific problems, similar but different transformations based on the same argument could also be applied.

We match the input and output (I/O) in the LHM case to the I/O of the Klein case, respectively, which basically include matching the incident and

transmitted wavevectors in one case with the other, as well as the phase velocity in both problems. Thus, Eqn. (VI.2) through Eqn. (VI.3) and Eqn. (VI.12) through Eqn. (VI.15) lead to the transformation given by

$$E \to \hbar\omega \tag{VI.24}$$

$$V \to (|n| + 1)\hbar\omega \tag{VI.25}$$

where n is the effective refractive index of LHM. Arrows should be understood in this way: Left-hand side gives us the physical properties in the Klein problem, in terms of the physical properties of the LHM problem on the right. However, this transformation is only valid for $V - E \gg mc^2$ and $|\mathbf{V}_g| \to c$, independent of any group index, which is defined as

$$n_g \equiv \frac{\mathrm{d}(n\omega)}{\mathrm{d}\omega}. \tag{VI.26}$$

On the other hand, since $|\mathbf{Q}_L|_z$ is assumed to be real negative, $\Delta\epsilon > -mc^2 + (c^2\hbar^2|\mathbf{K}_K|_x^2 + m^2c^4)^{1/2}$ and lossless LHM are considered.

Clearly, given a wave with angular frequency ω incident on an LHM results in exactly the same kind of wave propagation and refraction with that of its equivalent Klein counterpart, which is characterised by the transformations (VI.24) and (VI.25). Since the corresponding parameters (E, V, etc.) are on the order of the energy of a typical photon, they have to be scaled up to describe the Klein system with higher energies. Thus, having obtained the power transmission and reflection coefficients for the LHM, it is simple matter to find the equivalent pair production probabilities regardless of any scaling factor, since these coefficients are invariant under such scaling. Comparing Eqn. (VI.6) to Eqn. (VI.22) and Eqn. (VI.7) to Eqn. (VI.23), we observe that the $\mu \to 1$ applied to Eqns. (VI.6) and (VI.7) leads to Eqns. (VI.22) and (VI.23), respectively. Notice that this transformation negates the power transmission coefficient of the LHM thus simulating the particle-antiparticle pair production.

From the experimental point of view, once we obtained the power coefficients for LHM, their Klein counterparts can be found from

$$\frac{|T_K|}{T_L} \equiv T(\omega, \theta_i) = \frac{1}{|\mu|} \frac{(\mu s - a)^2}{(s - a)^2}, \tag{VI.27}$$

$$\frac{R_K}{R_L} \equiv R(\omega, \theta_i) = \frac{[(s + a)(\mu s - a)]^2}{[(s - a)(\mu s + a)]^2}. \tag{VI.28}$$

s and a are defined as

$$s \equiv \cos\theta_i \tag{VI.29}$$

$$a \equiv \sqrt{|n|^2 - \sin^2\theta_i}, \tag{VI.30}$$

where $s \neq a$ or $s \neq -a/m$. Note that these ratios are only functions of applied frequency and incidence angle. This is remarkable for the physical realization of such a simulator.

For example, let the incoming pulse be polarized but not monochromatic, such that it is represented by individual delta functions in frequency domain separated by $\Delta\omega_0 \gg \Delta\omega_i$ (i.e., $\Delta\omega_i$ is the bandwidth of individual pulses). Then each frequency component (ω_i) simulates a single Klein particle with different E_i, V_i, and m_i as well as $\Delta\epsilon_i$ corresponding to those delta functions. In other words, it is possible to simulate all single Klein particles simultaneously in the spectral bandwidth of the incoming pulse. The picture beyond the interface can be described as the superposition of all these solutions. However, since the transmitted waves interfere in LHM, to get output for these individual Klein particles, we need a spectral filter at the output.

The physical realization of such a processor performing this simulation is possible with current integrated optoelectronics and microelectronics machining technology. It mainly consists of an integration of an analog LHM component with

a digital readout circuit as well as some other optoelectronic components, which are controlled digitally.

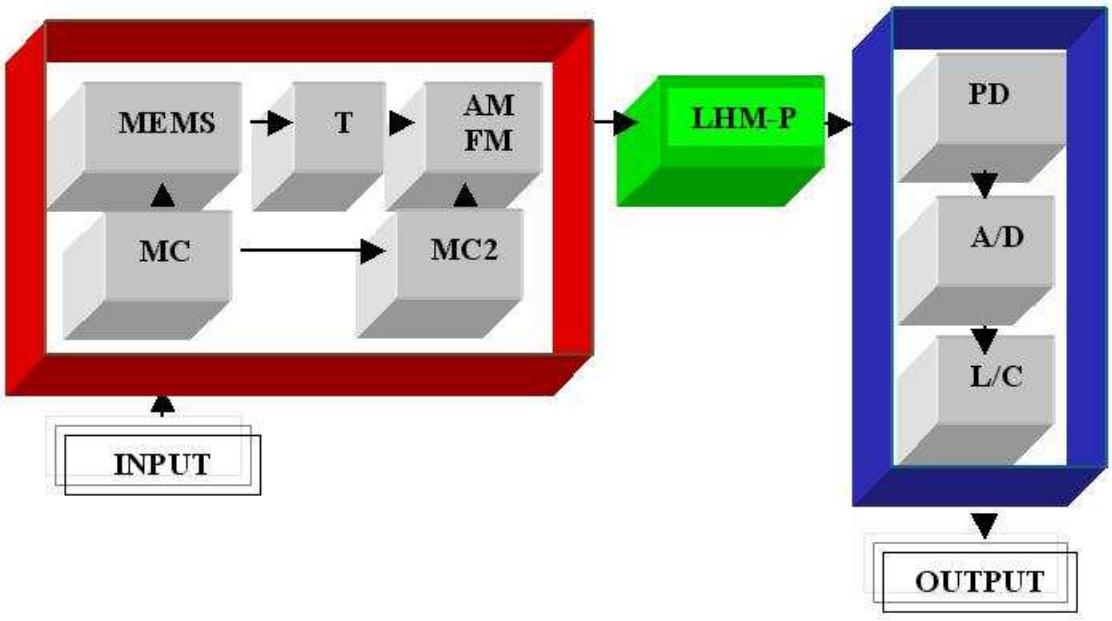

Figure VI.3: Block diagram for the simulator which roughly illustrates the components of the simulator. The quantum problem is defined and pre-processed in the red block and then sent to green block. Having been solved there, it is post-processed in the blue block, before obtaining output in Fig. VI.6. The simulator mainly consists of microcontrollers (MC), microelectromechanical systems (MEMS) actuator, transmitters (T), amplitude (AM) and frequency modulators (FM), LHM, photodetectors, analog to digital converters (A/D) and logic circuits (L/C).

Hardware implementation of this simulator is roughly illustrated in Fig. VI.3. The more detailed architecture design issues are out of the scope of this chapter and we will not consider here. The device mainly consists of three blocks. The problem we would like to solve is first defined and pre-processed in the red block, then it is solved in the green block and post-processed in the blue block. A microelectromechanical systems (MEMS) actuator, which is controlled by a microcontroller, changes the direction of the laser beam, while the amplitude and

frequency of the signal are tuned by using modulators in accordance with $R(\omega, \theta_i)$ and $T(\omega, \theta_i)$, before it is sent to LHM.

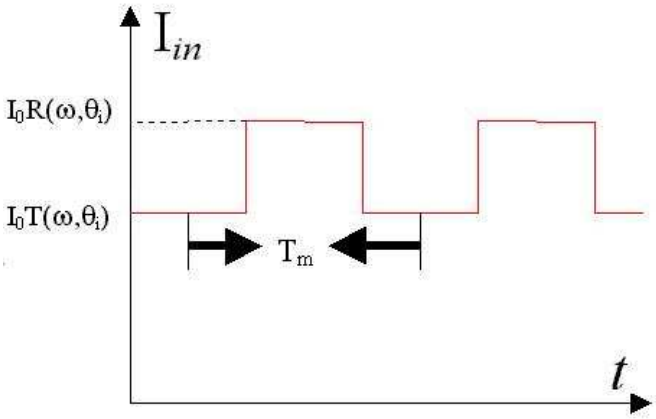

Figure VI.4: To get the same spatial pattern in the LHM with that of the Klein problem, the intensity of the input signal is modulated in a square wave manner. In this figure $R(\omega, \theta_i)$ is assumed to be larger than $T(\omega, \theta_i)$ for given ω and θ_i. Half the period T_m input intensity is set to $I_0 R(\omega, \theta_i)$ and in the remaining half it is set to $I_0 T(\omega, \theta_i)$.

Since the reflection coefficient for the Klein problem is bigger than one, normally it is not possible to obtain such a reflection coefficient using LHM. However, this problem can be overcome by using an amplitude modulator (AM) in the red block. AM, which is also driven by a MEMS actuator modulates the input signal between a peak and minimum value in the form of a square wave as shown in Fig. VI.4. Thus the intensity of the input signal is modulated between $I_0 R(\omega, \theta_i)$ and $I_0 T(\omega, \theta_i)$ in a square wave manner where I_0 is a constant. If the modulation period is T_m, half of the period the transmitter sends signal with intensity $I_0 T(\omega, \theta_i)$ which results in exactly the same spatial pattern in the LHM with that of antiparticles under Klein potential, and half of the period it sends signal which results in reflection to be bigger than one and exactly same spatial pattern with

that of the reflected particles due to the Klein step. Since we have divided T_m into two time slots, the sampling time and response speed for the detectors are important.

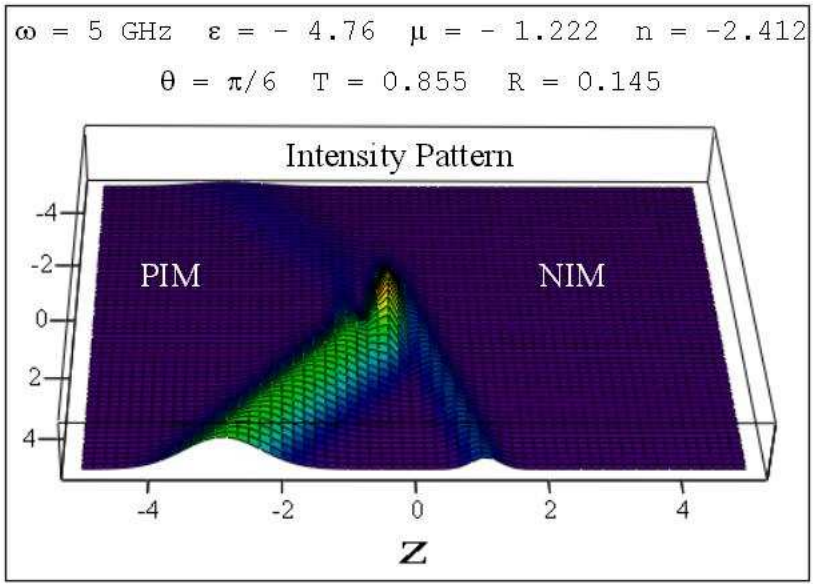

Figure VI.5: Negative refraction of a gaussian wavepacket with center frequency of 5GHz, which is incident on a NIM of refractive index -2.412. For an incidence angle of $\pi/6$, the corresponding transmittance T_L and reflectance R_L are 0.855 and 0.145, respectively. The colors show the relative intensity pattern at a random time. An interference fringes occur due to the incident (bottom left) and reflected (top left) wavepackets near the interface.

The calculated net effect of the LHM (i.e. no modulation) in Fig. VI.3 is shown in Fig. VI.5. In this calculation we assumed the form for the refractive index given by Ref. [66]

$$n(\omega) = \frac{\sigma'}{\omega}\left[\frac{(\omega^2-\omega_b^2)(\omega^2-\omega_p^2)}{\omega^2-\omega_0^2}\right]^{1/2}, \qquad \text{(VI.31)}$$

where σ' is -1 for simultaneously negative permittivity and permeability. The angle of incidence is taken as $\pi/6$ and the center frequency for the incident wavepacket is assumed to be 5GHz to have a negative refractive index in Eqn. (VI.31). The

gaussian wavepacket is designed by exploiting the method explained by Kong, et al [75]. The other parameters are the same as in Ref. [66], which are $\omega_p = 12.0$GHz, $\omega_b = 6.0$GHz, and $\omega_0 = 4.0$GHz.

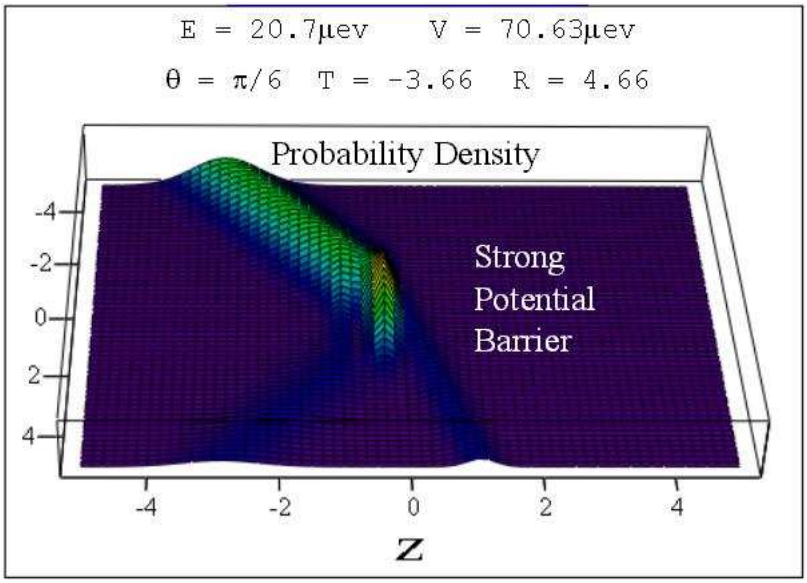

Figure VI.6: Solution to the Klein problem corresponding to the LHM problem in Fig. VI.5., which is obtained simply by setting $\mu = 1$. In this equivalent problem, the center energy of the wavepacket is 20.7μeV and the height of the potential barrier is 70.63μeV. For the same incidence angle of $\pi/6$, the corresponding transmittance T_K and reflectance R_K are -3.66 and 4.66, respectively. Colors show the probability density at the same random time with Fig. VI.5. Here also interference fringes occur near the interface between the incident (bottom left) and reflected (top left) wavepackets.

After the modulation the problem is ready to be simulated by the LHM, then its output is detected by the pixel arrays in the blue block and post-processed by means of analog to digital converters (A/D) and logic circuit to get the output shown in Fig. VI.6. Although mathematically it is easy to transform Fig. VI.5 to VI.6, $\mu \to 1$ transformation, modulation and some additional processing is required in its physical implementation.

The essential point to note in this operation is that although some digital operations take place, the problem is indeed solved by the LHM.

If the incident field contains infinitely many modes with the same frequency but propagating along different directions in the xz-plane, this corresponds to the simulation of the scattering of infinitely many non-interacting identical Klein particles with the same energy (or average energy per particle) due to a constant Klein step.

More complicated scenarios under these (or other) transformations with (or without) some approximations could also be possible.

Above simulations could indeed also be performed by PIMs. However, this would require additional circuitry and logic operations. One drawback of the NIM, on the other hand, is dynamic range problem. For more powerful and complex problems alternative types of NIMs with higher dynamic range are desired.

Here, we do not consider how to simulate a specific problem existing in the quantum relativistic field but we present a basic approach for how to handle some general and complicated problems, which might have/had been risen in this field, related with the Klein paradox using LHMs. Such a device performing certain operations based on mathematical connection could also be helpful in controlling some related quantum processes in real time, such as controlling pair production rate, distribution, and etc.

After we showed that the wave propagation in negative index materials is analogous to that of the Klein paradox, it came to our attention that the Klein paradox also exists in graphene, which was reported after our work. This made us to think that given our work and Ref. [76], there may be a link between negative index materials and graphene too, because of the Klein paradox. Shortly after that another paper was published in Science connecting the negative index materials and graphene [77].

Observation of the Klein tunnelling in negative index materials and the graphene are only two examples, which may open a way to the exploration of this

counterintuitive behavior in a relatively simple benchtop experiment. Otherwise it would appear such as at collisions of ultra-heavy nuclei or black hole evaporations [77].

A portion of this chapter was presented in a conference paper: D. Ö. Güney and D. A. Meyer, "*Optoelectronic simulation of the Klein paradox using left-handed materials*", 2004 MRS Spring Meeting, 12-16 Apr. 2004, San Fransisco, CA, USA.

Chapter VII

Conclusions and Future Work

Control over electrical properties of materials led to transistor revolution in electronics. PCs may have similar impact by controlling the flow of light. Given the immense literature produced only in about two decades, capabilities seem to be only lacked by the human imagination. Compatibility with other technologies such as microelectromechanical systems (MEMS), quantum dots, and fibers may further enhance their capabilities.

All of the approaches for quantum information processing have their own advantages, but unfortunately also their own drawbacks. Ideally, one would merge the most attractive features of those different approaches in a single technology. We envision that large-scale photonic crystal (PC) integrated circuits and fibers could be the basis for robust and compact quantum circuits and processors of the next generation quantum computers and networking devices. Cavity QED, solid-state, and (non)linear optical models for computing, and optical fiber approach for communications are the most promising candidates to be improved through this novel technology. In our work, we consider both digital and analog quantum computing.

The high quality factor and extremely low mode volume achieved successfully in microcavities have already made photonic crystals an especially attractive paradigm for quantum information processing experiments in cavity QED [12,

13, 59]. In our work we have extended this paradigm by solving analytically the Jaynes-Cummings Hamiltonian under the dipole and rotating wave approximations for two synchronized two-level atoms moving in a photonic crystal and by applying the solution to produce the two maximally entangled states in equations (IV.19) and (IV.20). We have also demonstrated the design of quantum logic gates, including dual-rail Hadamard and NOT gates, and SWAP gate operations. Our proposed system is quite tolerant to calculation and/or fabrication errors, in the sense that most errors remaining after the design can be corrected by simply experimentally adjusting the velocity or the angle between the atomic moment vector of the atom and the mode polarization. Our technique could not only be generalized to N-atom entanglement [13] but also has potential for universal quantum logic gates, atom-photon entanglement processes, as well as the implementation of various, useful cavity QED based quantum information processing tasks. We should also mention the methodological result that due to the emulation of 2D photonic crystal cavity modes in 3D photonic crystals [11, 29], one can design the more sophisticated circuit first in 2D to reduce the difficulty of the 3D computations, where typically much more computational power is needed.

In the circuit-level, we have designed an integrated conditional teleportation circuit with readout in a single PC chip. Our proposed PCQC can be implemented by current or near future semiconductor processing technologies and experimental techniques. Even the detectors and sources illustrated in Fig. V.1 could also be integrated—the feasibility of single atom detection on a PC chip has already been demonstrated [60], as have PC based lasers [61, 62]. In Ref. [60], for example, the detection of single atoms by exploiting a highly efficient integrated optical fiber-PC waveguide coupling is proposed. It could be envisioned that a compatible integrated atomic detection device based on such an experimental system might lead to more compact and robust PCQCs in general. The RC part of our device can not only be used with the TC but also can be used independently, or integrated with other compatible optical circuits to read out atomic states. It

also hints at the potential for implementation of atomic interferometers, such as the Ramsey interferometer, in photonic crystals.

The teleportation scheme we have designed can also be used for (i) quantum switching/routing, (ii) changing the velocity and direction of atoms on demand in a large scale PC quantum circuits and networks, among other applications.

To the best of our knowledge our work presents the first explicit designs of quantum circuits in the literature using PCs .

Achieving good mode-matching stability becomes quite cumbersome for many multiply nested interferometers in optical quantum computing. Photonic crystals, however, may be an especially promising paradigm as robust quantum circuit boards for delicate, next generation, scalable optical quantum computing and networking technologies, as well as scalable quantum dynamic random access memory [63], where qubits are refreshed using PC based cyclical quantum circuits. Integrated PC devices, such as planar waveguides and elementary interferometer modules, could replace the current bulky elements in linear optical quantum circuits. Furthermore, such devices could be made quite compact using PC integrated with single photon sources [7].

In the analog domain, we have shown that the Klein paradox for the KG equation of spin-zero particle exhibits exactly the same kind of wave propagation and refraction with those of the TM-polarized electromagnetic wave incident on LHM. Based on this amazing nature of LHMs, we have examined how to simulate the Klein paradox related problems and pointed out the possible applications of this optoelectronic simulator. Our work also highlights an optical approach to the analog quantum simulations based on the wave-particle duality in nature.

After we showed that the wave propagation in negative index materials is analogous to that of the Klein paradox, it came to our attention that the Klein paradox also exists in graphene, which was reported after our work. This made us to think that given our work in Chapter VI and Ref. [76], there may be a link between negative index materials and graphene too, because of the Klein paradox.

Shortly after that another paper was published in Science connecting the negative index materials and graphene [77].

Observation of the Klein tunnelling in negative index materials and the graphene are only two examples, which may open a way to the exploration of this counterintuitive behavior in a relatively simple benchtop experiment. Otherwise it would appear such as at collisions of ultra-heavy nuclei or black hole evaporations [77]. Our simulation of the Klein paradox using NIMs also opens a way to analog quantum simulation contrary to conventional digital quantum simulations, where the unitary transformations are approximated by sequence of logic gates [2].

Photonic crystal fibers (PCFs), on the other hand, may transform not only conventional optical communications but also may open a way to ultra high distance and data rate, secure quantum communications.

Fiber attenuation is critical for long distance and high data rate secure transmission. Attenuation of conventional telecom fiber (CTF) is about 0.2dB/km and to the best of our knowledge the minimum attenuation obtained experimentally is about 0.15dB/km [82]. Regarding PCF, on the other hand, holey fibers appear more promissing. Because the mode is confined inside the air core, which prevents absorption that exists in solid core optical fibers. However, the current attenuation obtained in these PCFs is still higher than that of CTFs. The record breaking number is currently 0.28dB/km . This is mainly because of the fabrication imperfections and surface modes residing between air-cladding interface. Minimum PCF attenuation predicted by P. Roberts, et al. is 0.1dB/km [83]. Under this value in our preliminary work (to be publishe elsewhere) we have shown that the transmission distance can be extended to about 100km from its original value of about 50km [84]. This is especially important for quantum communication, because data-rate exponentially decreases [85] with the number of delicate quantum repeaters.

Exploration of photonic crystals in the way of the realization of quantum computers may also lead to interesting avenues of fundamental physics beyond

negative index [67], electromagnetic cloak [78], and quantum Hall effect [79-81].

Future challenge is the development of fault-tolerant scalable quantum computer and network architectures based on photonic bandgap technology. Given current fabrication technoloy, optical properties of the designed structures agree well with the experiments. Although we consider a Q-factor of 10^8 in our work, incorporation of spontaneous emission rate and cavity decay into equations will decrease the required Q-factor substantially.

Bibliography

[1] J. J. Sakurai, *Modern Quantum Mechanics* (Addison-Wesley, 1994).

[2] M. A. Nielsen and I. L. Chuang, *Quantum Information and Quantum Computing* (Cambridge University, 2000).

[3] S. Chu, *Atom Interferometry, Course 4* (Physics Department, Stanford University).

[4] N. Ramsey, *Molecular Beams* (Clarendon, Oxford, 1956).

[5] W. H. Zurek, "Decoherence and the transition from quantum to classical," Phys. Today **44,** 36–44 (1991).

[6] M. Chapman, "Cavity QED approaches to quantum information processing and quantum computing," in *A Quantum Information Science and Technology Roadmap,* 2004, http://qist.lanl.gov.

[7] P. Kwiat and G. Milburn, "Optical approaches to quantum information processing and quantum computing," in *A Quantum Information Science and Technology Roadmap,* 2004, http://qist.lanl.gov.

[8] C. M. Soukoulis, "The history and a review of the modelling and fabrication of photonic crystals," Nanotechnology **13,** 420–423 (2002).

[9] E. Yablonovitch, "Photonic crystals," J. Mod. Opt. **41,** 173-194 (1994).

[10] Ekmel Özbay, Nanotechnology Research Center, Bilkent University, Ankara, Turkey, 06800 (personal communication, 2006).

[11] M. Qi, E. Lidorikis, P. T. Rakich, S. G. Johnson, J. D. Joannopoulos, E. P. Ippen, and H. I. Smith, "A three-dimensional optical photonic crystal with designed point defects," Nature (London) **429,** 538–542 (2004).

[12] N. Vats and T. Rudolph, "Quantum information processing in localized modes of light within a photonic band-gap material," J. Mod. Opt. **48,** 1495–1502 (2001).

[13] M. Konopka and V. Buzek, "Entangling atoms in photonic crystals," Eur. Phys. J. D **10,** 285–293 (2000).

[14] S. John and J. Wang, "Quantum optics of localized light in a photonic band gap," Phys. Rev. B **43,** 12772–12789 (1991).

[15] J. D. Joannopoulos, R. D. Meade, and J. N. Winn, *Photonic Crystals: Molding the Flow of Light* (Princeton University, 1995).

[16] M. Tavis and F. W. Cummings, "Exact solution for N-molecule-radiation field Hamiltonian," Phys. Rev. **170,** 379–384 (1968).

[17] T. B. Pittman and J. D. Franson, "Cyclical quantum memory for photonic qubits," Phys. Rev. A **66,** 062302–062305 (2002).

[18] D. G. Angelakis and P. L. Knight, "Testing Bell inequalities in photonic crystals," Eur. Phys. J. D **18,** 247–250 (2002).

[19] E. Hagley, X. Maitre, G. Nogues, C. Wunderlich, M. Brune, J. M. Raimond, and S. Haroche, "Generation of Einstein-Podolsky-Rosen pairs of atoms," Phys. Rev. Lett. **79,** 1-5 (1997).

[20] P. R. Villeneuve, S. Fan, and J. D. Joannopoulos, "Microcavities in photonic crystals: mode symmetry, tunability, and coupling efficiency," Phys. Rev. B **54,** 7837–7842 (1996).

[21] Jelena Vuckovic, Ginzton Laboratory, Stanford University, Stanford, CA, 94305 (personal communication, 2004).

[22] H. J. Kimble, "Strong interactions of single atoms and photons in cavity QED," Physica Scripta **T76,** 127–137 (1998).

[23] S. Haroche and J. M. Raimond, "Manipulation of nonclassical field states," in *Cavity Electrodynamics,* P. Berman, eds. (Academic, San Diego, Calif., 1994), pp. 126–127.

[24] Y. Yamamoto and A. Imamoglu, *Mesoscopic Quantum Optics* (Wiley-Interscience, 1999).

[25] R. J. Glauber and M. Lewenstein, "Quantum optics of dielectric media," Phys. Rev. A **43,** 467–491 (1991).

[26] S. G. Johnson and J. D. Joannopoulos, "Block-iterative frequency-domain methods for Maxwell's equations in a planewave basis," Opt. Express **8,** 173–190 (2001).

[27] S. G. Johnson and J. D. Joannopoulos, "Three-dimensionally periodic dielectric layered structure with omnidirectional photonic band gap," Appl. Phys. Lett. **77,** 3490–3492 (2000).

[28] M. L. Povinelli, S. G. Johnson, S. Fan, and J. D. Joannopoulos, "Emulation of two-dimensional photonic crystal defect modes in a photonic crystal with a three-dimensional photonic band gap," Phys. Rev. B **64,** 075313–075320 (2001).

[29] S. Fan, P. R. Villeneuve, R. D. Meade, and J. D. Joannopoulos, "Design of three-dimensional photonic crystals at submicron lengthscales," Appl. Phys. Lett. **65,** 1466–1468 (1994).

[30] K. H. Dridi, "Intrinsic eigenstate spectrum of planar multilayer stacks of two-dimensional photonic crystals," Opt. Express **11,** 1156–1165 (2003).

[31] K. H. Dridi, "Mode dispersion and photonic storage in planar defects within Bragg stacks of photonic crystal slabs," J. Opt. Soc. Am. B **21,** 522–530 (2004).

[32] C. H. Bennett, G. Brassard, C. Crepeau, R. Jozsa, A. Peres, and W. K. Wootters, "Teleporting an unknown quantum state via dual classical and Einstein-Podolsky-Rosen channels," Phys. Rev. Lett. **70,** 1895–1899 (1993).

[33] S.-B. Zheng, "Scheme for approximate conditional teleportation of an unknown atomic state without the Bell-state measurement," Phys. Rev. A **69,** 064302–064304 (2004).

[34] E. S. Guerra, "Teleportation of atomic states via cavity quantum electrodynamics," arXiv: quant-ph/0409194.

[35] D. Bouwmeester, J.-W. Pan, K. Mattle, M. Eibl, H. Weinfurter, and A. Zeilinger, "Experimental quantum teleportation," Nature (London) **390,** 575–579 (1997).

[36] D. Ö. Güney and D. A. Meyer, "Creation of entanglement and implementation of quantum logic gate operations using a three-dimensional photonic crystal single-mode cavity," J. Opt. Soc. Am. B **24,** 283–294 (2007). arXiv: quant-ph/0603087.

[37] Shi-Biao Zheng, Department of Electronic Science and Applied Physics, Fuzhou University, Fuzhou, 350002, China (personal communication, 2005).

[38] S. Osnaghi, P. Bertet, A. Auffeves, P. Maioli, M. Brune, J. M. Raimond, and S. Haroche, "Coherent control of an atomic collision in a cavity," Phys. Rev. Lett. **87,** 037902–037905 (2001).

[39] L. Davidovich, A. Maali, M. Brune, J. M. Raimond, and S. Haroche, "Quantum switches and nonlocal microwave fields," Phys. Rev. Lett. **71,** 2360–2363 (1993).

[40] X. Maitre, E. Hagley, G. Nogues, C. Wunderlich, P. Goy, M. Brune, J. M. Raimond, and S. Haroche, "Quantum memory with a single photon in a cavity" Phys. Rev. Lett. **79,** 769–772 (1997).

[41] S. Fan, "Sharp asymmetric line shapes in side-coupled waveguide-cavity systems," Appl. Phys. Lett. **80,** 908–910 (2002).

[42] E. Waks and J. Vuckovic, "Coupled mode theory for photonic crystal cavity-waveguide interaction," arXiv: physics/0504077.

[43] M. O. Scully and M. S. Zubairy, *Quantum Optics* (Cambridge University, 1997).

[44] A. Martinez, A. Garcia, P. Sanchis, and J.Marti, "Group velocity dispersion model of coupled-cavity waveguides in photonic crystals," J. Opt. Soc. Am. A **20,** 147–150 (2003).

[45] M. Loncar, T. Doll, J. Vuckovic, and A. Scherer, "Design and fabrication of silicon photonic crystal optical waveguides," J. Lightwave Technol. **18,** 1402–1411 (2000).

[46] S. Boscolo, M. Midrio, and C. G. Someda, "Coupling and decoupling of electromagnetic waves in parallel 2-D photonic crystal waveguides," IEEE J. Quantum Electron. **38,** 47–53 (2002).

[47] S. Kuchinsky, V. Y. Golyatin, A. Y. Kutikov, T. R. Pearsall, and D. Nedelikovic, "Coupling between photonic crystal waveguides," IEEE J. Quantum Electron. **38,** 1349–1352 (2002).

[48] T. Koponen, *Tunnelling of Light in Photonic Crystal Waveguides* (Thesis, University of Jyvskyl, Finland, 2003).

[49] C. J. M. Smith, R. M. De La Rue, M. Rattier, S. Olivier, H. Benisty, C. Weisbuch, T. F. Krauss, R. Houdre, and U. Oesterle, "Coupled guide and cavity in a two-dimensional photonic crystal," Appl. Phys. Lett. **78,** 1487–1489 (2001).

[50] P. Domokos, P. Horak, and H. Ritsch, "Quantum description of light pulse scattering on a single atom in waveguides," arXiv: quant-ph/0202005.

[51] N. Vats, T. Rudolph, and S. John, "Quantum information processing in localized modes of light within a photonic band-gap material," arXiv: quant-ph/9910046.

[52] S. Zippilli, D. Vitali, P. Tombesi, J.-M. Raimond, "Scheme for decoherence control in microwave cavities," Phys. Rev. **67,** 052101-052112 (2003).

[53] J. van Slageren, S. Vongtragoola, B. Gorshunovab, A. A. Mukhinb, N. Karla, J. Krzystekc, J. Telserd, A. Mllere, C. Sangregoriof, D. Gatteschif, and M. Dressela, "Frequency-domain magnetic resonance spectroscopy of molecular magnetic materials," Phys. Chem. Chem. Phys. **5,** 3837-3843 (2003).

[54] "Frequency stabilization and control system for backward-wave oscillators of $35 - 400$GHz range," Institute of Applied Physics Russian Academy of Sciences, Microwave Spectroscopy Laboratory, Novogorod, 603950 Russia, http://www.mwl.sci-nnov.ru/35.html.

[55] R. D. Meade, K. D. Brommer, A. M. Rappe, and J. D. Joannopoulos, "Electromagnetic Bloch waves at the surface of a photonic crystal," Phys. Rev. B **44,** 10961–10964 (1991).

[56] F. Ramos-Mendieta and P. Halevi, "Surface electromagnetic waves in two-dimensional photonic crystals: effect of the position of the surface plane," Phys. Rev. B **59,** 15112–15120 (1999).

[57] Y. A. Vlasov, N. Moll, and S. J. McNab, "Observation of surface states in a truncated photonic crystal slab," Opt. Lett. **29,** 2175–2177 (2004).

[58] T. Ochiai and J. Sanchez-Dehesa, "Superprism effect in opal-based photonic crystals," Phys. Rev. B **64,** 245113–245119 (2001).

[59] J. Vuckovic, M. Loncar, H. Mabuchi, and A. Scherer, "Design of photonic crystal microcavities for cavity QED", Phys. Rev. E **65,** 016608–016618 (2001).

[60] B. Lev, K. Srinivasan, P. Barclay, O. Painter, and H. Mabuchi, "Feasibility of detecting single atoms using photonic bandgap cavities," arXiv: quant-ph/0402093.

[61] A. Sugitatsu, T. Asano, and S. Noda, "Line-defect-waveguide laser integrated with a point defect in a two-dimensional photonic crystal slab," Appl. Phys. Lett. **86,** 171106–171108 (2005).

[62] X. Checoury, P. Boucaud, J. - M. Lourtioz, O. Gauthier-Lafaye, S. Bonnefont, D. Mulin, J. Valentin, F. Lozes-Dupuy, F. Pommereau, C. Cuisin, E. Derouin, O. Drisse, L. Legouezigou, F. Lelarge, F. Poingt, and G. H. Duan, "1.5μm room-temperature emission of square-lattice photonic-crystal waveguide lasers with a single line defect," Appl. Phys. Lett. **86,** 151111–151113 (2005).

[63] S. Bandyopadhyay, "Prospects for a quantum dynamic random access memory (Q-DRAM)," arXiv: quant-ph/0101058.

[64] V. G. Veselago, "The electrodynamics of substances with simultaneously negative values of ϵ and μ," Sov. Phys. Usp. **10,** 509–514 (1968).

[65] D. R. Smith, W. J. Padilla, D. C. Vier, S. C. Nemat-Nasser, and S. Schultz, "Composite medium with simultaneously negative permeability and permittivity," Phys. Rev. Lett. **84,** 4184–4187 (2000).

[66] D. R. Smith and N. Kroll, "Negative refractive index in left-handed materials," Phys. Rev. Lett **85,** 2933–2936 (2000).

[67] R. A. Shelby, D. R. Smith, and S. Schultz, "Experimental verification of a negative index of refraction," Science **292,** 77–79 (2001).

[68] P. M. Valanju, R. M. Walser, and A. P. Valanju, "Wave refraction in negative-index media: always positive and very inhomogeneous," Phys. Rev. Lett **88,** 187401–187404 (2002).

[69] D. R. Smith, D. Schurig, and J. B. Pendry, "Negative refraction of modulated electromagnetic waves," Appl. Phys. Lett **81,** 2713–2715 (2002).

[70] S. Foteinopoulou, E. N. Economou, and C. M. Soukoulis, "Refraction in media with a negative refractive index," Phys. Rev. Lett. **90,** 107402–107405 (2003).

[71] G-J Ni, W. Zhou, and J. Yan, "Klein paradox and antiparticle," arXiv: quant-ph/9905044.

[72] H. Nitta, T. Kudo, and H. Minowa, "Motion of a wave packet in the Klein paradox," Am. J. Phys. **67,** 966–971 (1999).

[73] A. Calogeracos and N. Dombey, "Klein tunnelling and the Klein paradox," Int. J. Mod. Phys. A **14,** 631–644 (1999).

[74] O. Panella, Y. N. Srivastava, and A. Widom, "Klein paradox for optical scattering from excited targets," arXiv: quant-ph/0105010.

[75] J A Kong, B Wu, and Y Zhang, "Lateral displacement of a Gaussian beam reflected from a grounded slab with negative permittivity and permeability," Appl. Phys. Lett. **80,** 2084–2086 (2002).

[76] M. I. Katsnelson, "Graphene: Carbon in two dimensions," Materials Today **10,** 20–27 (2007).

[77] V. V. Cheianov, Vladimir Fal'ko, and B. L. Altshuler, "The focusing of electron flow and a Veselago lens in graphene p-n junctions," Science **315,** 1252–1255 (2007).

[78] F. Zolla, S. Guenneau, A. Nicolet, and J. B. Pendry, "Electromagnetic analysis of cylindrical invisibility cloaks and the mirage effect," Opt. Lett. **32,** 1069–1071 (2007).

[79] F. D. M Haldane and S. Raghu, "One-way Waveguides": Analogs of Quantum Hall Edge-States in Photonic Crystals," arXiv: cond-mat/0503588.

[80] S. Raghu and F. D. M. Haldane, "Analogs of quantum Hall effect edge states in photonic crystals," arXiv: cond-mat/0602501.

[81] M. Onoda, S. Murakami, and N.Nagaosa, "Hall effect of light," Phys. Rev. Lett. **93,** 083901–083904 (2004).

[82] K. Nagayama, M. Kakui, M. Matsui, I. Saitoh, Y. Chigusa, "Ultra-low-loss (0.1484 dB/km) pure silica core fibre and extension of transmission distance," Electronics Lett. **38,** 1168–1169 (2002).

[83] P. Roberts, F. Couny, H. Sabert, B. Mangan, D. Williams, L. Farr, M. Mason, A. Tomlinson, T. Birks, J. Knight, and P. St. J. Russell, "Ultimate low loss of hollow-core photonic crystal fibres," Opt. Express **13,** 236–244 (2005).

[84] Gobby, Z. L. Yuan, and A. J. Shields, "Unconditionally secure quantum key distribution over 50 km of standard telecom fibre," Electronics Lett. **40,** 1603–1605 (2004).

[85] E. Waks and J. Vuckovic, "Dipole Induced Transparency in Drop-Filter Cavity-Waveguide Systems," Phys. Rev. Lett. **96,** 153601–153604 (2006).